1-1-2017

Pet Imaging Of Early Therapeutic Response In Solid Tumors

Stephanie J. Blocker
Wayne State University,

PET IMAGING OF EARLY THERAPEUTIC RESPONSE IN SOLID TUMORS

by

STEPHANIE J BLOCKER

DISSERTATION

Submitted to the Graduate School

of Wayne State University,

Detroit, Michigan

in partial fulfillment of the requirements

for the degree of

DOCTOR OF PHILOSOPHY

2017

MAJOR: CANCER BIOLOGY

Approved By:

_____

Advisor Date

_____

_____

_____

_____

DEDICATION

To my father, mother, and sister.

ACKNOWLEDGEMENTS

With the completion of my dissertation work, there are a great deal of people who deserve my appreciation. The work I have accomplished, as well as all of the knowledge I have gained, would not have been possible without the support of my advisors, my colleagues, my family, and my friends.

Advisor

I would like to express my sincere gratitude to Dr. Anthony Shields, who has served as my advisor during my dissertation work. Along with providing an environment in which I could learn, design projects, and hone my skills, Dr. Shields also encouraged me to develop creative problem solving skills. His ever-inspired approach to solving scientific problems has taught me how to ask questions, to thoughtfully tackle problems, and to see the big picture that is often obscured by details. I thank Dr. Shields for his unwavering support as a mentor, and for serving as a model of scientific integrity that I will strive to match throughout my career.

Dissertation Committee

Throughout my dissertation research, I have received encouragement and mentorship from each of the members of my Dissertation Committee. Each member has provided me with valuable insight, and encouraged my ideas as they developed. Dr. Nerissa Viola has been an invaluable source of knowledge, information, and inspiration regarding all imaging aspect of my projects, and has helped me navigate the logistical hurdles that lie between concept and completion. Dr. Olivia Merkel has consistently asked thoughtful questions which allowed me to see my projects from multiple perspectives, and has proposed inventive solutions for difficult problems. Dr. David

Gorski has provided vital insight into the biology and design of multiple facets of these projects, and has encouraged me to seek and understand the clinical implications of my results. Dr. Joshua Reineke, despite being in another state, continues to provide a wealth of information and expertise on the chemistry and engineering of many of the elements of my projects. Each of my committee members has provided me with valuable mentorship and consistent encouragement, for which I am especially grateful.

Shields Lab

Each member of the Shields team has been a great source of support for me during the entire time in the lab. I would like to thank Kirk Douglas for his contributions to my projects and my education, of which there are too many to list. Kirk not only helped me navigate the difficult logistics of setting up my studies, but he also helped me to complete them—all while being a great friend, particularly during the most stressful times. I want to acknowledge Jawana Lawhorne-Crews for teaching me the basics of image analysis and imaging study design. Her advice was essential, as I had no experience in the field upon joining the lab. I would also like to sincerely thank Janice Akoury, for her unwavering dedication to helping me navigate the uncertainties of graduate school. I am unable to count the number of pitfalls and disasters I avoided thanks to her brilliant problem-solving and foresight. Also, I want to acknowledge former lab member, Dr. Omid Tahrani, whose work in the Shields Lab provided the rationale for a large part of my dissertation. Finally, I would like to thank Enxhi Lalo, an undergraduate student at Michigan State University whom I had the pleasure to mentor for three summers. Enxhi's dedication to learning and his interest in clinical science made for a great partnership, and the work he completed during his time in the lab has been an important addition to the Shields Lab.

Cancer Biology Graduate Program

Of course, I must mention the Cancer Biology Graduate Program, and the integral role its administration has played in my accomplishments thus far. I would like to thank Dr. Larry Matherly for his personal vested interest in the success of the students in the CB program. His guidance was instrumental in helping me to get the most out of my experience at Wayne State. To Dr. George Brush, I would like to offer my thanks for all of the input and advice he has provided over the years. I would like to thank Nadia Daniel, for her never-ending enthusiasm for the CB students and for ensuring that we were always connected to the resources we needed to succeed. Additionally, I would like to thank the members of the Cancer Biology Steering Committee for fostering a student research-focused environment for the program and its students to flourish.

Additional Significant Support

I would like to specifically thank Dr. Lisa Polin and her lab for all of the guidance, assistance, and expertise she offered over the years. I credit the efficiency of our animal studies to her expert input, without which we likely would have had fewer, more arduous successes. Staff members of her lab, Juiwanna Kushner and Katherine White, were persistently helpful as well during our studies, and their input was always appreciated.

I want to specifically acknowledge Karri Stark, who was my unofficial mentor in all aspects of in vitro work. Her unmatched skillset, ability to pinpoint problems, and dedication to all things science were the foundations on which I was able to learn a large portion of my bench skills. I thank Karri for serving as a role model for me as I continue to work and learn.

During my collaboration with Merrimack Pharmaceuticals, I was able to work with many great scientists out of Boston. I would like to thank Dr. Helen Lee and Dr. Bart Hendriks for their persistent support of my project, and for their continued input and advice. In particular, I would like to specifically thank Helen for always responding quickly and beyond sufficiently each time I asked a question.

During our animal imaging studies, I had the opportunity to work with Dr. Xin Lu, who often offered his support and expertise. I would like to thank him for his help with the microPET instrumentation and data configuration, as well as his insight into the data analysis.

I would also like to thank Dr. Tom Mangner, for synthesizing the ^{18}F-FMAU for all of the lung studies. Without his hard work, none of those studies would have been possible.

Family and Friends

Aside from the amazing support I have received from mentors and colleagues, none of my accomplishments to date would have been possible if not for the steadfast support of my family. I want to give my most heartfelt thanks to them for everything they have done to keep me motivated and calm throughout this process. I thank my dad, who has always been confident in my ability to do great things—even when I wasn't sure, myself. He has never let his daughters forget that he believes in us, and that has always helped me to push through the tougher times. I thank my mom, who taught me everything I know about being a strong, intelligent woman. She has always been a fierce advocate for her daughters, and is always ready to help, no matter what the issue. I thank my sister, Jillian, who has taught me the value of keeping perspective, and taking time to

laugh. Despite being my younger sister, I feel that she has taught me so much about how to identify the important things in life. My family's support has never faltered, and I hope to make them proud as I move forward.

I would also like to thank my husband, Alex Duric. Having met in the lab, Alex often understood the frustrations I would often experience with my projects, and was always able to suggest something helpful. Throughout my dissertation work, he has helped me to grow as a person, and is the single largest contributor to my confidence. I want to thank him for keeping me grounded, while encouraging my dreams to take flight. I also want to thank Alex's parents, who have very quickly become wonderful additions to my family and are always very supportive.

TABLE OF CONTENTS

LIST OF TABLES

LIST OF FIGURES

LIST OF ABBREVIATIONS

%i.d.	Percent injected dose
%i.d./cc	Percent injected dose per gram
$\%\Delta SUV_{max}$	Percent change in maximum Standardized Uptake Value
µCi	Microcurie
µm	Micrometer
µmol	Micromole
^{18}F	Fluorine-18
2q7d	Two doses per week
5FU	5-fluorouracil
^{64}Cu	Copper-64
^{99}Tc	Technetium-99
ATCC	American Type Culture Collection
ATP	Adenosine triphosphate
Bev	bevacizumab (Avastin™)
Bq	Becquerel
Cc	Cubic centimeter; gram
CD31	Cluster of differentiation 31
CD34	Cluster of differentiation 34
Ci	Curie
Cm	Centimeter
CRC	Colorectal cancer
CT	Computerized Tomography

DCE-MRI	Dynamic contrast-enhanced magnetic resonance imaging
DNA	Deoxyribonucleic acid
Dox	Doxorubicin
Dpm	Disintegrations per minute
DTPA	Diethylenetriaminepentaacetic acid or pentetic acid
Dx-NP	Diagnostic Nanoparticles
ECM	Extracellular matrix
EPR	Enhanced permeability and retention
FAU	1’-(2’-deoxy-2’-fluoro-beta-D-arabinofuranosyl)uracil
FDG	Fluorodeoxyglucose
FIAU	2’-fluoro-2’-deoxy-1-beta-D-arabinofuranosyl-5-iodo-uracil
FLT	Fluorothymidine
FMAU	1’-(2’-deoxy-2’-fluoro-beta-D-arabinofuranosyl)thymine
G	Gram
Gd	Gadolinium
HBS	HEPES-buffered saline
HEPES	2-[4-(2-hydroxyethyl)piperazin-1-yl]ethanesulfonic acid
HER2	Human epidermal growth factor receptor 2
HPLC	High-pressure liquid chromatography
HPMA	N-(2-Hydroxypropyl)methacrylamide
IACUC	Institutional Animal Care and Use Committee
IC_{50}	Half maximal inhibitory concentration
IFP	Interstitial fluid pressure

IP	Intraperitoneal
iTLC	Instant thin layer chromatography
IV	Intravenous
kBq	kiloBecquerel
kBq/cc	kiloBecquerel/gram
keV	Kiloelectronvolt
Kg	Kilogram
KOH	Potassium hydroxide
K^{ps}	Transfer coefficient
LP	Liposome(s)
LP-I	Liposomal irinotecan
M	Molar
mCRC	Metastatic colorectal cancer
Mg	Milligrams
Mg	Milligram
Ml	Milliliter
Mm	Millimeter
mM	Millimolar
Mm	Millimeter
MR	Magnetic resonance
MRI	Magnetic Resonance Imaging
MTT	3-(4,5-Dimethylthiazol-2-yl)-2,5-Diphenyltetrazolium Bromide
MVD	Microvessel density

NaOAc	Sodium acetate
NiR	Near infrared
Nm	Nanometer
NP	Nanoparticle(s)
PBS	Phosphate buffered saline
PEG	Polyethyline glycol
PET	Positron Emission Tomography
RBC	Red blood cell
RNA	Ribonucleic acid
ROI	Region of Interest
RPMI-1640	Roswell Park Memorial Institute-1640
Rx	Drug
S phase	Synthesis phase
SCID	Severe Combined Immunodeficiency
SD	Standard deviation
SPECT	Single Photon Emission Computerized Tomography
SUV	Standardized Uptake Value
SUV_{max}	Maximum Standardized Uptake Value
$t_{½}$	Half-life
TK1	Thymidine Kinase 1
TK2	Thymidine Kinase 2
Tx-NP	Therapeutic Nanoparticles
VEGF	Vascular endothelial growth factor

VEGFR	Vascular endothelial growth factor receptor
VOI	Volume of Interest
Δ	Change

CHAPTER 1. INTRODUCTION

In recent decades, cancer imaging has advanced beyond the determination of size and location of lesions to defining the biological properties of tumors. One of the most powerful tools to dynamically measure tumor activity is positron emission tomography (PET), a form of nuclear medicine imaging which utilizes small doses of radioactive tracers to produce three dimensional images. While PET can provide morphological information about solid tumors, the novelty of PET imaging over other modalities is its ability to non-invasively provide information about the metabolic behavior of tumors. This allows both physicians and researchers to gain insight into the tumors which may aid in determining the best options for treatment, as well as monitor tumor response to therapies. In this way, PET is one of the diagnostic modalities at the forefront of personalized medicine for cancer patients.

1. Basic PET Physics and Tracer Synthesis

PET is performed by injection of a radioactive tracer, and scans are acquired on by detection of emitted photons. Tracers for PET are designed to incorporate positron emitting nuclides, such as ^{18}F or ^{64}Cu. Upon decay, positrons are released from the nuclide and subsequently collide with an electron in the surrounding area. This collision, or annihilation, releases two photons with energies of 511 keV in opposite directions (1). PET utilizes rings of crystal blocks to quantitate emitted photons (2, 3).by detecting coincidence pairs of photons in all directions around the object being scanned. Subsequently, a statistical map of describing the probable 3-dimensional location of tracer is generated. After

allowing for distance traveled by the positron prior to annihilation, tissue scatter, and coincidental detection of non-paired photons (“random” events), clinical PET scanners typically have a spatial resolution of about 4-5 mm (4). Preclinical PET scanners for small animal imaging typically have better resolution, due to the smaller diameter of the crystal rings (5, 6). This leads to resolution of about 1-2 mm in PET images acquired during small animal imaging (7-9). Additionally, the detection of only 511 keV photons by the PET crystals results in excellent sensitivity, often between 10^{-11} and 10^{-12} mol/L of tracer required to obtain an image (10). Tracers synthesized for PET often exhibit high specific activity which, combined with PET detection sensitivity, allows for image acquisition with a relatively small mass of tracer required (2).

Tracers for PET are be rationally designed to image biological processes of interest to acquire valuable biochemical information (11). Depending on their atomic properties, positron emitting nuclides can be incorporated into biologically active molecules. For example, ^{18}F is can be substituted for a hydroxyl group, such as at the C-2 position of glucose to form 2-deoxy-2-^{18}F-fluorodeoxyglucose, or ^{18}F-FDG (12) . ^{18}F-FDG is thought to be retained in metabolically active tissues following uptake mediated by glucose transporter 1, or GLUT1 followed by phosphorylation by hexokinase (13). ^{18}F-FDG was one of the first FDA-approved tracers for PET for a variety of applications. It is relatively easy to synthesize, and ^{18}F is widely available. In utilizing a glucose analogue, ^{18}F-FDG images can identify tissues that are metabolically active, such as brain and heart (14).

Additionally, proliferating tumors utilize circulating glucose during cellular metabolism.

Another commonly used tracer in PET is ^{18}F-fluorothymidine, or ^{18}F-FLT. ^{18}F-FLT is a thymidine analogue that is taken up by cells through the salvage pathway of DNA synthesis (15). Mimicking endogenous thymidine, ^{18}F-FLT is trapped in rapidly dividing cells which are rapidly dividing, such as tumor. Thus, ^{18}F-FLT serves as a marker of cellular proliferation with PET (16).

1.1. Biological Implications of PET Interpretation

Although the mechanism of tracer quantitation during PET is always coincidence detection of 511 keV photons, PET tracers can be designed to image a multitude of tissue properties. As with ^{18}F-FDG and ^{18}F-FLT, positron emitting nuclides can be incorporated into a variety of small biologically active molecules to image their activity in tissues of interest. Further, nuclides can be incorporated into larger structures, such as nanoparticles, to determine their delivery to tissues such as solid tumors (17, 18). Importantly, the amount of tracer required for PET imaging is normally too small to disrupt the kinetics of endogenous molecules, ensuring that the tracer will not alter biochemical pathways and confound scans (19).

PET can measure specific processes of tumors for the purpose of classification, predicting treatment success, and monitoring tumor response to therapy over time. Tracers for PET are often able to detect or probe for subtle changes in tumor metabolism or intratumoral biochemistry. PET scans offer the opportunity to measure metabolic changes which occur in response to therapy (20-

22). For example, ^{18}F-FDG has been studied in the clinic as a prognostic marker for progression free survival and overall survival prior to treatment with antivascular agents in patients with metastatic renal cell carcinoma (23). ^{18}F-FDG was similarly able to predict overall survival and metastasis-free survival in early hepatocellular carcinoma prior to surgery (24). In studies with ^{18}F-FLT, researchers have been able to assess early responses to sunitinib treatment in patients with metastatic renal cell carcinoma (25). ^{18}F-FLT imaging has also been shown to identify progression of pancreatic cancer early into gemcitabine treatment, to potentially select patients that may benefit from alternative therapeutic options (26). Importantly, different tumors can exhibit varying levels of tracer uptake. Baseline uptake should be considered when choosing tracers to monitor therapeutic response in cancers, as one tracer is not likely to be suitable for all cases.

While identifying tumor location, size, and stage are important aspects of imaging in oncology, PET can provide specific information about the biological characteristics of an individual tumor. By designing tracers to measure biological pathways of interest, PET can be used to quantitate these tumor characteristics in ways which impact therapeutic decisions. Measuring early changes in tumor metabolism and behavior which result from treatment can provide individualized information about a patient's likelihood of response (11, 27, 28). The ability to identify responders early into treatment would allow physicians to make the best therapeutic decisions for cancer patients. Imaging with PET is an invaluable tool for the personalization of medicine for solid tumors.

2. PET for Early Detection of Therapeutic Effects on Solid Tumors

In clinical oncology, one of the most promising aspects of PET research is the potential to image early tumor response to therapy. Although new therapies for a multitude of cancers are being developed each year, measurable response to cancer treatments are extremely heterogenous in patient populations (29-31). Traditionally, patients and their physicians were forced to wait until months of treatment are completed to determine the extent, if any, of therapeutic efficacy. Thus, a means by which physicians could predict therapeutic success or failure early into cancer treatments could save patients valuable time, resources, and avoid unnecessary side effects.

The principle of measuring early metabolic consequences of successful therapy has been demonstrated using ^{18}F-FDG imaging. Multiple studies have been performed to evaluate ^{18}F-FDG PET in measuring early response to breast cancer treatment, including one of the first of such studies in patients published by Wahl *et al.* (32). Patients were scanned with ^{18}F-FDG before beginning the first cycle of chemotherapy, and at multiple time points throughout therapy. Interestingly, significant reductions in ^{18}F-FDG uptake were observed in as little as 8 days, and continued through day 60 of treatment in women who responded to therapy. Conversely, little change was observed in PET of women who were later identified as non-responders. In another example, by Buvat *et al.*, aimed to identify PET measurement thresholds of early therapeutic response in metastatic colorectal cancer patients receiving chemotherapy (33). The authors found that after 14 days of therapy, standardized uptake values (SUV) of tumors with ^{18}F-

FDG PET were able to predict response when compared to pre-treatment scans. In thymic epithelial tumors, Segreto *et al.* measured ^{18}F-FDG uptake in tumors before and after three cycles of chemotherapy (34). Similarly, the authors found that changes in ^{18}F-FDG uptake following partial therapy differed between responders and non-responders. In each of these studies, the authors noted that early changes in ^{18}F-FDG uptake preceded any measurable changes in tumor morphology. In this way, ^{18}F-FDG PET has demonstrated the utility of measuring metabolic changes to assess early therapeutic effects in cancer and results with a number of tumor types and treatments have been explored (35-37).

Although ^{18}F-FDG is among the most commonly used tracers utilized for PET, multiple forms of radiolabeled small molecules and macromolecules are currently being studied as tracers to image early response to therapy. With the increasing interest in precision personalized medicine, tracers are being developed as companions to therapy in order to offer insight into unique behavior of a patient's disease. One strategy revolves around developing tracers which mimic a targeted therapeutic agent in order to assess availability of the target or successful delivery of the treatment (38, 39). Another approach is the design of tracers to measure downstream or biologically-related processes in order to measure the effect of a treatment (40, 41). In each case, although the effects of the therapeutic strategies may face heterogeneous response in patient populations, companion imaging offers a means by which clinicians and researchers can more efficiently plan and assess successful treatments for patients on an individual basis.

3. Imaging of Nanoparticle Distribution to Assess Treatments that Alter Delivery

As interest in nanoparticles (NP) for delivery of therapeutic agents to solid tumors grows, methods to measure or predict their utility are critically needed. Imaging NP can streamline the development and implementation of NP treatments, and can serve as tools for personalized medicine. NP platforms for drug delivery are used to enhance drug deposition in tumor tissues to increase effective therapeutic doses (42). However, preclinical successes in treating tumors with NP are often met with failure in human trials due to ineffective delivery to tumors in the heterogeneous patient population (43, 44).

By providing non-invasive, quantitative measures of NP localization, imaging can provide invaluable information of NP distribution in tumors. With imaging, the delivery of NP can be assessed in a patient or lesion, predict therapeutic efficacy of NP treatments, and monitor distribution over time or as a response to treatment. While ineffectual NP delivery in human tumors has hampered the path to the clinic, researchers are now considering the use of therapies which alter the tumor and its microenvironment to improve NP delivery (45). The use of imaging to quantify NP delivery could identify and characterize novel methods for improving NP localization to solid tumors. In the clinic, these same NP-based imaging tools can be used to personalize treatments by predicting therapeutic outcomes, identifying barriers to delivery, and monitoring changes in delivery throughout the course of treatment.

“Nanotheranostics” to visualize delivery with non-invasive imaging

In addition to delivering therapeutic payloads, many NP can be designed or modified for imaging to act as a tracer or contrast agent. Imaging with NP (diagnostic NP; Dx-NP) that mimic the systemic distribution of drug-loaded NP (therapeutic NP; Tx-NP) can assess the tumor-targeting capacity of the NP platform.

Recently, coupling of targeted therapies with complimentary diagnostic imaging has been termed “theranostics” (46). From this, the emerging field of “nanotheranostics” provides tools to measure NP delivery which may predict efficacy of NP therapy on an individual basis (47, 48). Examples of a variety of NP for imaging are outlined in Table 1. While imaging with Dx-NP to predict therapeutic response has been the goal of nanotheranostics, the potential utilities of imaging in NP research are myriad. Dx-NP can measure the release of payloads, or assess drug availability (49). Non-invasive scans can be repeated over time to monitor delivery through the course of treatment. Perhaps the newest and least explored utility for nanotheranostics is in evaluating strategies to improve NP deposition in tumors with therapies that have an impact on enhanced permeability and retention (EPR). Imaging with Dx-NP can allow researchers and clinicians evaluate how therapies such as radiation, chemotherapy, and anti-vascular agents affect the delivery of NP. Utilizing imaging with NP could streamline NP development, identify the best combination therapies and treatment timelines, and narrow the gap between preclinical studies and clinical application of NP.

Table 1. Examples of nanoparticle platforms for imaging

Platform	Name	Tumor Model	Modality	Therapeutic Component	Ref.
Liposome					
	Liposomal Gd-DTPA	Colon	DCE-MRI	None	(50)
	MM-302	HER2+ breast	PET	Dox; Anti-HER2 antibody fragment	(51)
	Fluorescently-labeled liposomes	Murine colon	NiR Imaging	None	(52)
	Fluorescent PEGylated siRNA-lipoplexes	Murine colon	NiR Imaging	siBcl-2	(53)
	Liposomal iodine	Primary sarcoma	CT	None	(54)
	^{99}Tc-liposomes	Feline soft tissue sarcoma	Gamma camera	None	(55)
	^{99m}Tc-DSPE-PEG$_{2000}$	Rat fibrosarcoma	Gamma camera	None	(56)
	^{99}Tc-labeled liposomal Dox	Head and neck; Squamous cell carcinoma	SPECT	Dox	(57, 58)
Copolymers					
	HPMA-Dox	Prostate	MRI	Dox	(59)
	HPMA-gemcitabine	Prostate	Gamma camera	Gemcitabine	(59)

Dendrimer					
	G8-Gd-D	Squamous cell carcinoma	MRI	None	(60)
Iron oxide nano-particles					
	Ferumoxyol (Feraheme)	Murine mammary; Pancreas	MRI	None	(61, 62)
	Angiospark680	Breast	NiR Imaging	None	(63)
Macro-molecular Complexes					
	Albumin-$(GdDTPA)_{30}$	Breast	DCE-MRI	None	(64)
	Gadofosveset trisodium (albumin bound)	Mouse mammary	MRI	None	(61)

Enhanced Permeability and Retention

NP have long been thought to localize to solid tumors via EPR. Tumors generate aberrant blood vessels which can harbor gap openings of between 400 and 600 nm (65). Coupled with poor lymphatic drainage, leaky tumor vasculature causes large particles to become trapped in tumor interstitial spaces (66). NP, which are usually 10 to 100 nm, have been shown preclinically to passively accumulate in tumors due to EPR, often regardless of targeting surface moieties (67, 68).

Perhaps the most commonly cited barrier to therapeutic NP efficacy is delivery to and penetration of tumor tissues, despite preclinical results (43, 69). Researchers have since suggested that EPR is hampered in humans by conditions of high interstitial fluid pressures (IFP), increased pericyte coverage, inconsistent vessel pore sizes, and thicker collagen and extracellular matrix (ECM) layers (70-73). The parameters which define EPR are highly variable in patients, and are based on dynamic conditions that change over time.

The task of improving NP accumulation in solid tumors can be viewed from two perspectives: (1) adjustment of the physical parameters of the NP, and (2) therapeutic modulation of the tumor and its microenvironment (74). Studies of the former are already actively utilizing imaging (75, 76). By adding diagnostic components to the NP platform, researchers can measure differences in systemic distribution of NP during the design, modification, or fine-tuning of NP. This can mean manipulating size and shape, surface chemistry, targeting moieties, etc. (77).

The latter describes the use of therapeutic interventions which make tumor tissues more available to NP infiltration. Many currently-accessible treatments have the capacity to influence EPR parameters (78). To improve NP delivery, multiple groups are utilizing therapies that affect tumor blood flow, vascular permeability, IFP, and ECM components (79, 80). The goal is to reduce or remodel the physical barriers to macromolecular profusion in human tumors, and provide therapeutic avenues to improve outcomes of NP which are already in or near clinical trials. Nanotheranostics studies utilize various imaging modalities to measure and monitor differences in NP distribution patterns which result from additional therapies/interventions. A summary of these studies is provided in Table 2. These studies identify tools and techniques for personalization of NP therapies for cancer.

Table 2. Preclinical studies of Imaging NPs for measuring therapeutically-altered NP delivery

Therapeutic Strategy	Treatment	Drug	NP Imaging Probe	Modality	Observed Effect	Ref
Targeting Tumor Vasculature						
	VEGFR inhibition	Axitinib	Albumin-$(GdDTPA)_{30}$	DCE-MRI	Reduced vascular permeability of NP	(64)
	Alk5 inhibition	LY-364947	Ferumoxytol (Feraheme)	MRI	Modest improvement of enhancement throughout tumor	(61)
		A-83-01	Liposomal Gd-DTPA	DCE-MRI	Increased AUC of Gd accumulation in tumor	(50)
Tumor Debulking						
	Cytotoxic Therapy	Cyclo-phosphamide	^{64}Cu-MM-302 (HER2-targeted liposomal Dox)	PET	Reduced IFP; increased liposomal delivery to tumors; improved T_x efficacy	(51)
		S-1 (Tegafur)	Fluorescent PEGylated liposomes	NiR Imaging	Increased liposomal delivery; increased homogeneity	(52)
			Fluorescent siRNA lipoplexes	NiR Imaging	Increased uptake of lipoplexes in tumors; improved therapeutic efficacy	(53)
Radiation						
	Single High-Dose RT	N/A	G8-Gd-D	MRI	Increased enhancement at multiple time points	(60)
			Liposomal Iodine	Dual-energy CT	Increased iodine concentrations in tumors; increased permeability	(54)
			HPMA-Dox (Gd)	MRI	Enhanced tumor localization; increased efficacy and toxicity	(59)
			HPMA-gemcitabine (^{131}I)	Gamma Camera	Enhanced tumor localization; increased efficacy, modest toxicity	(59)
			Angiospark680	NiR Imaging	Increased accumulation of probe in tumors; increased efficacy of subsequent Doxil T_x	(63)

Thermal Ablation						
	Microwave Ablation	N/A	^{99}Tc-Liposomes	Gamma Camera	Increased liposome accumulation in tumor	(55)
	Warm Water Catheter	N/A	^{99m}Tc-DSPE-PEG_{2000}	Gamma Camera	Increased liposome accumulation in tumor; increased Dox delivery with subsequent Doxil T_x	(56)
	Radio-frequency thermal ablation	N/A	^{99}Tc-Liposomal Dox	Gamma Camera; SPECT	Increased liposome delivery to tumor; increased levels of Dox in resected tumor tissues	(57)
Targeting ECM and BM						
	Collagen remodeling	Collagenase-2	^{99}Tc-Doxil	SPECT	Transient drop in IFP; increased intratumoral Doxil localization	(58)
		Losartin	Ferumoxytol	MRI	Increased tumor blood pool as measured with ferumoxytol; enhanced uptake of subsequent SMI drugs	(62)

Changes in NP Delivery Due after Therapeutically Targeting Tumor Vasculature

Large pores and gaps in tumor vessel walls allow for extravasation of macromolecules in circulation, including NP (81). These characteristics are heterogeneous in clinical populations, making them a somewhat difficult target for cancer therapies (82). Although often lacking widespread impact as monotherapies, drugs which target angiogenesis or vessel integrity have been shown to improve outcomes when combined with chemotherapy (83, 84). One example is bevacizumab (Avastin™; Genentech, San Francisco, CA), a vascular endothelial growth factor (VEGF)-targeted antibody which is FDA approved in combination with chemotherapy in multiple tumor types (85). Another example is ziv-aflibercept injection (Zaltrap®, Sanofi and Regeneron Pharmaceuticals, Inc., Tarrytown, NY), which is a recombinant fusion protein which contains domains which bind to portions of VEGF, and has been FDA approved for combination with chemotherapy in colon cancer (86). However, the ability to modulate tumor vasculature properties is an attractive concept when facing the problem of inconsistent NP distribution in tumors. Thus, agents which target a number of vascular properties have been suggested as a means of altering EPR to enhance NP delivery.

3.1. Imaging the Effects of Targeting Tumor Angiogenesis on NP Deposition in Solid Tumors

Anti-angiogenic therapies like bevacizumab are designed to disrupt tumor blood vessel formation and ultimately starve tumors of nutrients. These drugs have led to modest improvements in clinical outcomes when combined with conventional chemotherapy (83, 84).

3.1.1. Anti-VEGF therapies

While depletion of blood vessels is the intended outcome of anti-angiogenic therapy, there is some evidence that these drugs cause temporary remodeling or "normalization" of blood vessels, which may affect drug delivery for a short time (87, 88). With the expanding use of anti-angiogenic therapies in the clinic, a complete understanding of their effect on NP delivery will be important as N5P enter clinical trials, and treatment regimens.

A study performed by Wilmes *et al.* measured the effect of blocking VEGF signaling on perfusion of small and large contrast agents with DCE-MRI in BT474 breast tumor xenografts in mice (64). The group utilized a novel small molecule inhibitor of VEGF receptor tyrosine kinase, axitinib (AG-013736; Inlyta®; Pfizer, NY, NY) to disrupt tumor vessel properties and growth. Administration of the drug for three weeks showed dramatic antitumor action. DCE-MRI images to measure early drug effects were obtained with both macromolecular albumin-bound gadolinium-bound diethylenetriaminepentaacetic acid (GdDTPA) and low molecular weight GdDTPA contrast agents before and after axitinib therapy.

After only seven days of axitinib administration, the authors noted a marked decrease in tumor perfusion compared to control tumors. Reduced vessel permeability was evident from significant drops in tumor endothelial transfer coefficients (K^{ps}) calculated for both contrast agents. Histology staining for CD31 performed in resected tumor tissues showed a reduced number of microvessels after seven days of treatment, which complements the imaging data. The measurable decrease in albumin-bound GdDTPA perfusion into tumor tissues

following short-term axitinib therapy suggests that imaging with DCE-MRI can provide early and dynamic measures of changes in macromolecular distribution. This study indicates that macromolecular delivery to tumors can be dramatically altered by therapeutic intervention, and provides rationale for utilizing imaging to measure these effects early into treatment.

3.1.2. Targeting TGF-β

Multiple studies have demonstrated that NP accumulation in solid tumors can be enhanced by treatment with agents which cause tumor vessels to become leaky (89, 90). A popular target is the transforming growth factor (TGF)-β pathway, since blocking the kinase activity of the TGF-β1 receptor has been shown to increase tumor vessel leakage (91). Drugs that inhibit TGF-βR1, also known as activin-like kinase 5 (Alk5), are widely available and relatively well characterized, which simplifies their incorporation into nanotheranostic studies.

Daldrup-Link *et al.* chose to utilize MR imaging to measure the effect of Alk5-inhibitor [3-(pyridine-2-yl)-4-(4-quinonyl)]-1H-pyrazole (LY-364947 Calbiochem, San Diego, CA) on the delivery of NP-based contrast agents in transgenic mouse mammary tumor virus-driven expression of the polyoma middle T oncogene (MMTV-PyMT) adenocarcinoma, as well as an orthotopic glioblastoma model (61). MRI images were performed with gadofosveset trisodium (Ablavar®), a small molecule contrast agent which binds albumin to form macromolecular complexes in circulation, as well as ferumoxytol (Feraheme™), an iron oxide NP. Images were obtained at baseline, and following 6 days of

treatment with LY-364947, i.p. every other day to visualize the effect of Alk5 inhibition on NP delivery.

In tumors subjected to Alk5 inhibition, tumor enhancement increased threefold compared to controls in MR images with gadofosveset, primarily in the tumor periphery, and twofold in images with ferumoxytol, throughout tumor tissues. The authors suggest that Alk5 inhibition may be able to improve NP delivery and efficacy, and that this effect can be visualized with NP contrast agents for MR imaging. In this way, image-guided modulation of TGF-β signaling can be used to personalize NP therapies.

Another study, carried out by Minowa *et al.* in mice bearing colon 26 tumors, measured the effect of Alk5 inhibition with A-83-01 on NP delivery by performing DCE-MRI with liposomal Gd-DTPA. The authors compared baseline scans to scans acquired 24 hours after initiating treatment, which consisted of two injections of A-83-01. Compared to baseline scans, treatment resulted in a 3.8-fold increase in the AUC of Gd concentration (Figure 1). This implies that even short-term Alk5 inhibition can markedly improve liposome delivery to the tumor. Importantly, imaging with a liposomal contrast agent for MRI was able to identify improved liposomal delivery very early into Alk5 inhibition with A-83-01.

4. PET with Radiolabeled Pyrimidine Analogs for Early Assessment of Drug Efficacy in Tumors

Just as oncologists have relied on tissue biopsies to help define and stage tumors, PET images can be used to quantitatively assess the metabolic behavior

of tumors. However, while biopsies involve invasive procedures and produce a limited sample, PET images non-invasively provide information about the entire tumor and surrounding tissues. In this way, PET is ideal for longitudinal studies of tumor metabolism and for measuring changes in response to therapy (92, 93). While response to treatment is usually confirmed by morphological changes in tumor tissues (e.g. tumor size, tissue necrosis, etc.) (94), PET can measure biochemical shifts indicative of therapeutic response prior to any noticeable changes in tumor morphology.

PET Imaging of Cellular Proliferation

Although many studies have demonstrated the usefulness of ^{18}F-FDG PET in evaluating cancer treatment response, FDG imaging has limitations (95). As a radiolabeled form of glucose, ^{18}F-FDG is capable of measuring changes in glucose metabolism that result from treatment. Tumor cells often exhibit a highly glycolytic metabolism, whereby glucose is converted to lactate for ATP synthesis. This occurs in lieu of ATP generation through oxidative phosphorylation (96). Increased glucose consumption is one of the primary reasons that ^{18}F-FDG is expected to be taken up in greater amounts by tumor tissues (97). However, there is evidence that ^{18}F-FDG uptake is not ubiquitous in all tumors, and can be affected by a variety of different tumor- or microenvironment-specific mechanisms (98-100). In fact, ^{18}F-FDG uptake in tumors, while still an important tool for clinicians, may not provide the most direct measure of tumor response to therapy. Thus, other tracers developed for PET may provide a more straightforward measure of early

therapeutic response in tumors by measuring processes which are directly related to tumor survival and progression.

Pyrimidine Analogues

One of the fundamental traits of a tumor is the ability to maintain and increase proliferative behavior (101). Cells in proliferative tissues must duplicate their DNA to divide, a process requiring availability of purines and pyrimidines. Cellular consumption of thymidine is favored for measuring DNA synthesis and cell division. Compared to other nucleosides, thymidine is only incorporated in nuclear DNA, and not utilized in forming RNA (102). Exogenous uptake of natural thymidine in cells correlates with S phase of the cell cycle. To exploit the direct relationship between cellular thymidine salvage and cellular division for tumor imaging, multiple radiolabeled thymidine analogues have been developed for PET (103).

Of the thymidine analogues for oncological PET, 3'-[^{18}F]fluoro-3'-deoxythymidine (^{18}F-FLT) is the most widely accepted and utilized (104, 105). The replacement of the 3' hydroxyl group on a thymidine molecule with ^{18}F allows the tracer to be taken up into cells and phosphorylated, but not incorporated into growing DNA without inducing termination (106). ^{18}F-FLT is phosphorylated by thymidine kinase 1 (TK1), which traps it within cells following incorporation (15). ^{18}F-FLT has been suggested as a marker of proliferation in tumors by measuring TK1 activity during its metabolism via the thymidine salvage pathway (107). Tracer uptake correlates with immunohistochemical staining for proliferation marker Ki-67

in subsequently resected tissues (108). Clinically, ^{18}F-FLT PET is used to approximate tumor proliferation, offering insight into the aggressiveness of a tumor and its capacity to progress.

Although less commonly studied than ^{18}F-FLT, other thymidine analogues have been developed as PET tracers. These include, but are not limited to FMAU (1-(2'-deoxy-2'-fluoro-beta-D-arabinofuranosyl)thymine), FIAU (2'-fluoro-2'-deoxy-1-beta-D-arabinofuranosyl-5-iodo-uracil), and FAU (1-(2′-deoxy-2′-fluoro-β-d-arabinofuranosyl) uracil) (103). Of these, ^{18}F-FMAU has been of interest for imaging proliferation in tumors as an alternative to ^{18}F-FLT. The fluorine group on ^{18}F-FMAU is attached at the 2' position of thymidine, leaving the 3' hydroxyl group intact for ^{18}F-FMAU incorporation into DNA (109). An advantage of ^{18}F-FMAU over ^{18}F-FLT for PET is that ^{18}F-FMAU does not demonstrate the same high uptake in tissues like bone marrow, making identification of tumors in these tissues more feasible (110). One limitation of both FLT and FMAU is high uptake in the liver of humans, which is due to metabolism rather than proliferation (111, 112)(refs). This is likely due to the nature of FMAU phosphorylation which, unlike FLT, occurs predominantly by thymidine kinase 2 (TK2), not TK1 (102). Interestingly, TK2 phosphorylation of thymidine (and its analogues) is associated with the synthesis of mitochondrial DNA, not nuclear DNA (113). While both ^{18}F-FLT and ^{18}F-FMAU are taken up by tumor tissues during thymidine salvage, the phosphorylation of these by TK1 and TK2 respectively leads to differential retention. This, in turn, requires distinct interpretation of PET scans performed with either tracer.

FLT and predicting therapeutic response

While studies of the other thymidine analogues remain relatively limited, multiple researchers have suggested that the utility of ^{18}F-FLT lies in imaging early response to therapy. Tumor tissues, while normally rapidly dividing, often slow or stall proliferative processes when under stress caused by treatment (102). The effects of anticancer drugs, particularly of drugs which target DNA synthesis, have been measured early into treatment with ^{18}F-FLT (107).

In preclinical studies of ^{18}F-FLT PET in lymphoma, Graf *et al.* found that ^{18}F-FLT uptake significantly decreased in tumors treated with doxorubicin after only 48 hours (114). Similarly, Ullrich *et al.* found that ^{18}F-FLT uptake in erlotinib-sensitive non-small cell lung tumors significantly decreased after two days of therapy compared to drug-resistant controls (115). A clinical study in esophageal squamous cell cancer patients, performed by Chen *et al.*, demonstrated that ^{18}F-FLT scans performed before and 4 weeks into chemotherapy or radiotherapy could distinguish between responders and non-responders (116). It is important to note that in these studies ^{18}F-FLT was directly compared to ^{18}F-FDG, and in each case ^{18}F-FDG did not have the predictive power demonstrated by ^{18}F-FLT. The growing base of evidence supporting the use of ^{18}F-FLT in predicting response early into cancer treatment has strengthened the utility of PET in oncology (117). Further, the variety of other thymidine analogue tracers could lead to new methods for measuring the early effect of therapies for a variety of cancers.

CHAPTER 2. LIPOSOMAL ^{64}CU-PET IMAGING OF ANTI-VEGF DRUG EFFECTS ON LIPOSOMAL DELIVERY TO COLON CANCER XENOGRAFTS.

1. Introduction

Globally, colorectal cancer (CRC) is the third most common cancer in men (approximately 746,000 cases) and the second most common in women (approximately 614,000 cases) as of 2012 (118, 119). The push for precision medicine has led to a greater understanding of the molecular and genetic subtypes of CRC among the population (120-123), and promoted the search for prognostic and predictive biomarkers. However, while multiple molecular markers have shown promise as prognostic indicators (124, 125), attempts to utilize them in the clinic have led to conflicting results (126-129). Thus, tumor stage and supporting histological analysis remain the primary basis for therapeutic decision making in CRC (130, 131).

In addition to the search for prognostic markers for CRCs, research has also focused on uncovering better drug options. Standard cytotoxic agents for CRC include 5-fluorouricil (5FU), often combined with irinotecan and/or oxaliplatin (131-139). In patients with advanced disease almost all patients still develop resistance to treatment and succumb to tumor growth (140, 141). Targeted antibodies are regularly used in treating mCRC, including agents which target vascular endothelial growth factor (VEGF) and its receptor (VEGFR) (142). Targeting of VEGF pathways in CRC is designed to reduce tumor blood supply by disrupting tumor vessels, and has had some success in the clinic (143, 144). One such therapy is bevacizumab (bev; Avastin™; Genentech, San Francisco, CA), a VEGF-targeted monoclonal antibody, has been approved for CRC patients in combination

with various chemotherapy regimens. Unfortunately, most therapeutic options in CRC have faced the problem of resistance in the clinic, often due to the heterogeneous nature of colon tumors (144-148).

Recently, there has been a growing interest in the development of nanoparticle-based therapies, such as liposomes (LP), for cancer as multiple preclinical studies have shown notable success in cellular and animal models (149-155). Clinical trials utilizing LP for CRC treatment focus primarily on delivery of well-characterized drugs, including irinotecan and its metabolite, SN-38, or doxorubicin (130, 156, 157). LP deposition in solid tumors is heavily influenced by enhanced permeability and retention (EPR), making the state of tumor blood vessels a key factor in delivery. Theranostic approaches for imaging delivery of LP could provide vital insight into the probability of success when treating with LP platforms for drug delivery (158-160). In this study, we have utilized a ^{64}Cu-loadable liposome formulation to image the effects of short-term bev treatment on LP delivery to colon tumor xenografts in mice. We chose to target tumor vasculature, as the state of vessels in solid tumors is critical in defining EPR, and thus macromolecular delivery (161-163). Although the long-term effects of bev on tumor vasculature have been established, there is evidence that bev begins altering tumor vessels and affecting vascular permeability early into treatment (164). Thus, we aimed to measure any early changes in LP localization induced by short-term bev with PET, and monitor subsequent therapy with liposomal irinotecan (LP-I; MM-398; Onivyde®; Merrimack Pharmaceuticals Inc., Cambridge MA). In doing so, we generated a system to measure dynamic changes in LP deposition which

could affect the efficacy of LP-based therapies on an individual basis. Furthermore, we were able to non-invasively measure significant differences in LP delivery between bev-treated tumors and control tumors early into bev treatment. Finally, the results seen with PET correlated with subsequent monitoring of treatment efficacies, suggesting that this platform could have utility in predicting and monitoring therapeutic LP success.

2. Materials and Methods

Materials

HT-29 cells and McCoy's 5a Modified Medium were purchased from ATCC (Manassas, VA) and kept below 15 passages following receipt. 4-DEAP-ATSC chelator, empty MM-DX-929 liposomes, and LP-I were provided by Merrimack Pharmaceuticals, Inc. (Cambridge, MA). $^{64}CuCl_2$ was purchased from the Department of Radiology at Washington University (St. Louis, MO). Chelation efficiency was measured with iTLC-SG plates (Agilent Technologies, Santa Clara, CA). Loading efficiency was assessed with Sephadex G-50 DNA Grade Illustra Nick columns (GE Healthcare, Pittsburg, PA).

Gamma spectroscopy was performed on a Packard Cobra II gamma counter (Perkin-Elmer Inc., Waltham, MA). PET scans were acquired on an R4 microPET (Concorde Microsystems, Knoxville, TN). CT images were acquired using an Inveon microSPECT/CT (Siemens Preclinical Imaging Solutions, Malvern, PA). Images were registered and analyzed using PMOD Image Matching and Fusion Tool ver3.6 (PMOD group, Switzerland). Statistical analyses were performed using GraphPad Prism, ver7 (GraphPad Software Inc., La Jolla, CA).

Labeling MM-DX-929 with chelated ^{64}Cu

Upon receipt of $^{64}CuCl_2$, ^{64}Cu was chelated with 4-DEAP-ATSC (98±2% chelation efficiency), followed by loading into empty liposome (95±3% loading efficiency). Briefly, $^{64}CuCl_2$ was vortexed with 4-DEAP-ATSC solution (0.06 mg/ml chelator in 0.1M citrate buffer, pH 6) at room temperature for 10 seconds, then allowed to sit for one minute and vortexed again. Efficiency of ^{64}Cu chelation was determined by diluting a sample in citrate buffer for instant thin layer chromatography as described previously (165). Briefly, the radioactivity at the solvent front (free ^{64}Cu in solution) and at the sample origin (^{64}Cu-DEAP-ATSC complex) was measured by gamma spectroscopy of the iTLC plates. Greater than 90% chelation efficiency was required to proceed to loading.

^{64}Cu-MM-DX-929 was prepared by mixing ^{64}Cu-DEAP-ATSC with empty MM-DX-929 liposomes (15 mM phospholipid in 10 mM HEPES buffered saline, 150 mM sodium chloride, pH 6.5) and heated for 10 minutes at 65 °C, followed by immediate cooling in an ice water bath for one minute, as previously described (165). Loading efficiency of ^{64}Cu was assessed by performing size exclusion chromatography on an Illustra NICK column with a small sample of prepared ^{64}Cu-MM-DX-929 in HEPES buffered saline (HBS). Radioactivity of the eluent containing labeled ^{64}Cu-MM-DX-929 in HBS, and the column containing ^{64}Cu-DEAP-ATSC was measured with gamma scintigraphy. Greater than 90% labeling efficiency was achieved before proceeding with animal imaging.

Cell Culture

HT-29 human colorectal adenocarcinoma cells were cultured in McCoy's 5a Modified Medium supplemented with 5% fetal bovine serum and 1% penicillin/streptomycin, as described by ATCC. Cells were kept at 37°C with 5% CO_2 and were passaged with trypsin at approximately 80% confluence. Prior to inoculation in mice, cells were not passaged more than ten times in culture. Cell line identity was authenticated at time of all studies with the PowerPlex® 16 System from Promega (Madison, WI) in the Applied Genomics Technology Center at Wayne State University. Analyses were performed using ATCC and DSMZ reported karyotypes. Tumor fragments were subcutaneously implanted into SCID NCr female mice on day 0 by trochar.

Animal Studies

Tumor model: Cultured HT-29 human colorectal adenocarcinoma cells were used to establish a subcutaneous tumor model in female SCID NCr mice (Charles River Labs; MA) and thereafter maintained in serial passage.

MicroPET studies: Schematic representation of mouse study design is presented in Figure 1. Tumors were upstaged to 250mg (range: 200-300mg, day 12), and mice non-selectively randomized into their respective control (No Rx) and treatment groups (bev). All mice were imaged with microPET before and after bev treatment (on days 13 and 20) 24hr after intravenous (IV) administration of $^{64}CuCl_2$ MM-DX-929. Scans were compared for changes in LP accumulation during this time period. Mice were euthanized under anesthesia with whole blood and tissues collected after the second PET for biodistribution measurements and histological

analysis. For subsequent studies, after the 2nd scan, mice were further divided into 4 groups of n=6 (No Rx, Bev, LP-I, and Bev + LP-I) to assess tumor progression post bev treatment, with or without LP-I, compared to untreated controls. All mice were weighed and observed daily for the duration of the study. Tumors were measured by caliper 2-3x/weekly with the formula [volume (mg) = length (mm) x width^2 (mm^2)/2] used to calculate tumor mass.

Tracer preparation and injection: Empty LP MM-DX-929 (Merrimack Pharmaceuticals, Cambridge, MA) were labeled with $^{64}CuCl_2$ chelated with 4-DEAP-ATSC). Mice were administered 200-300 µCi/injection, IV within a 0.1 to 0.3 ml volume range; 22-24 hours prior to each microPET scan.

Drug preparation: Bevacizumab was prepped fresh for each injection from 25 mg/ml stock diluted with 0.9% sterile saline, pH 6.0 and injected intraperitoneally (IP) at 5 mg/kg in a volume of 0.2ml/20g mouse on days 14 and 17 (2q7d).

Liposomal Irinotecan (LP-I; MM-398; Onivyde®, Merrimack, Cambridge, MA) was prepped fresh for each injection from 5.05mg/ml stock diluted with 0.9% sterile saline, pH 6.0 and injected IV at 10 mg/kg in a volume of 0.2 ml/20g mouse on days 21, 24, and 28.

All animal studies were approved by and performed in strict accordance with the policies of the Institutional Animal Care and Use Committee (IACUC) at Wayne State University.

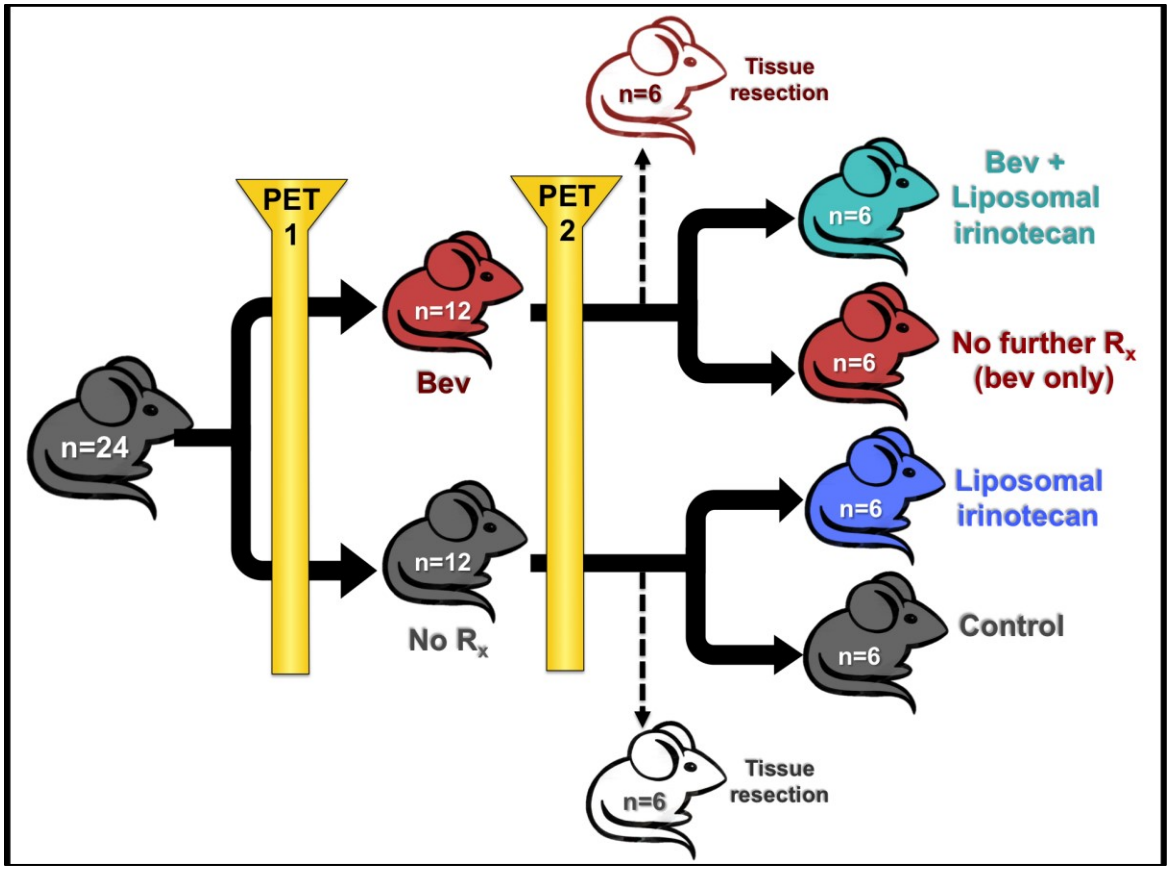

Figure 1. Liposome animal study design. Schematic representation of treatment groups and timeline for mice treated with bev, LP-I, bev followed by LP-I, and controls.

Animal Imaging with ^{64}Cu-MM-DX-929 PET

^{64}Cu-MM-DX-929 (104 nm) was used to approximate the systemic distribution of LP-I (110 nm), as it has been shown to predict the accumulation of LP-I in solid tumors (166). Following ^{64}Cu-liposome preparation, mice received approximately 200-300 μCi of ^{64}Cu-MM-DX-929 (20 μmol/kg lipid) intravenously via the tail vein. ^{64}Cu-MM-DX-929 was imaged with PET 24±2 hours post-injection, as liposomes remain in the blood pool for extended periods before depositing in tissues. Anesthesia was induced with 3% inhaled isoflurane, and maintained during scanning with 2% isoflurane. Mice were positioned prone on the scanner

bed with heating pad to maintain body temperature. Fiducial markers labeled with ^{64}Cu were fixed to the bed for subsequent alignment of PET and CT images. PET acquisition was performed for 10 minutes, followed by CT scanning 10 minutes to obtain anatomical images.

Attenuation correction was performed on the whole body microPET images based on previously recorded transmission scans. Images were reconstructed by applying an iterative ordered-subsets expectation maximization 2-dimensional algorithm (167). Together with scatter correction, these parameters yielded an isotropic spatial resolution of approximately 2mm in full width at half maximum (168). Prior to study, a phantom for ^{64}Cu was scanned to calculate conversion from counts/pixel/minute to kBq(μCi)/cm^3.

PET/CT image registration and analysis

PET and CT images were registered and aligned using the PMOD Image Matching and Fusion Tool. Regions of interest (ROIs) were defined manually on individual planes of the PET, using the aligned CT images for anatomical reference. 3-dimensional volumes of interest (VOIs) were generated from the stacked ROIs of the tissue of interest. Activity in the VOIs, as detected by PET in kBq(μCi)/cm^3, was converted to standardized uptake values based on injected dose and body weight. SUV_{max} values were calculated by averaging the max pixel value in the ROI of the three hottest consecutive planes in a tissue, and normalizing to injected dose and body weight.

^{64}Cu-MM-DX-929 PET imaging of short-term bev effects

A baseline ^{64}Cu-MM-DX-929 PET was performed on all mice at day 14 post-tumor implant, followed by half of the mice receiving two injections of bev over seven days. Bev was administered IP at 5 mg/kg in a single injection performed on days 14 and 17 (two total injections). All mice received a second ^{64}Cu-MM-DX-929 PET on day 20. Day 20 scans (post-treatment) were compared to scans from day 13 (baseline) and analyzed for changes in ^{64}Cu-MM-DX-929 delivery to tumor. Results were compared between bev-treated and control mice.

Whole body tissue distribution of ^{64}Cu-MM-DX-929

^{64}Cu-MM-DX-929 retention in bulk tissues was assessed by gamma spectroscopy of resected tissues. Briefly, following the second PET scan (day 7), mice were sacrificed and tissues harvested (n=8). These included tumor, liver, heart, lung, intestine, stomach, kidney, spleen, and blood. Tissues were washed in water, weighed, and activity was measured for one minute on a gamma counter. Activity in tissues was decay corrected to time of injection and normalized to tissue weight (kBq/cc). Tissue biodistribution was compared between bev-treated and untreated mice to ensure that bev treatment was not affecting retention of ^{64}Cu-MM-DX-929 in healthy tissues.

Immunohistochemistry and microvessel density analysis

Tumors resected after the second PET were fixed in formalin and paraffin embedded. Immunohistochemistry for CD34, and staining with hematoxylin (Sigma Aldrich, St. Louis, MO) was performed on 5 μm slices, and digital images of the entire cross section were captured. Sample identities were blinded, and

images were analyzed with Pannoramic Viewer ver1.15.4 (3DHISTECH Ltd., Budapest, Hungary). For each tissue, five distinct areas of 200 mm^2 were utilized in assessing microvessel density. Briefly, tumor blood vessels (as identified by CD34 staining) were counted in each section, and distance measurements across the widest diameter of each vessel were used to determine vessel size. The average number of vessels per cm^3 and the average vessel diameter were calculated.

^{64}Cu-labeled liposome interactions with macrophage populations in blood

^{64}Cu-MM-DX-929 as well as ^{64}Cu-MM-302, a structurally related liposome, were incubated in human whole blood for one hour with gentle rocking at 37˚C. Incubated blood samples, as well as samples collected from clinical trials of patients scanned with ^{64}Cu-MM-302, were subjected to density gradient centrifugation over a Ficoll-Hypaque gradient. Plasma, white blood cells, and red blood cells (RBCs) were separated via multiple centrifugation steps. White blood cell fractions were incubated in cell culture flasks with lymphocyte-cultured medium for 3 hours to induce macrophage adherence. Non-adhered lymphocytes were carefully aspirated, and attached monocytes were collected via Trypsin wash. Plasma, RBC, lymphocyte, and macrophage fractions were measured with gamma scintigraphy to determine ^{64}Cu-LP content. Values are represented as %total counts.

Whole blood from patients receiving ^{64}Cu-MM-302 was also subjected to size exclusion chromatography to determine LP stability at multiple time points, including 1 hour, 24 hours, and 48 hours after injection.

Statistical Analysis

Tumor growth curves with mean ± standard error was plotted and growth rates were tested with linear mixed model. Tumor latency to 1 gram total burden was tested with Kruskal-Wallis test, after normality assumption was evaluated with Shapiro-Wilk test. Statistical analyses were performed using R version 3.2 (The R Foundation for Statistical Computing). All other statistical analyses were performed using GraphPad Prism 7 (GraphPad Software Inc., La Jolla, CA). Data were presented as the mean ± standard error. Comparisons between the bevacizumab and control were performed using two-sample Student's t-test. A p-value of <0.05 was considered statistically significant.

3. Results

3.1. ^{64}Cu-MM-DX-929 PET can detect significant differences in LP delivery between colon tumors treated with bev and untreated controls

Liposome distribution in mice bearing subcutaneous HT-29 colon tumor xenografts was measured with ^{64}Cu-MM-DX-929 PET at baseline prior to any treatment. Due to the extended circulation times of liposomes in the body, images were acquired 24 ± 2 hours following tracer injection (approximately two half-lives of ^{64}Cu, $t_{1/2}$ = 12.7 hours) to allow extravasation from the blood pool (165). Tracer uptake was notable in liver (due to extensive vasculature) and spleen, and was still visible in the heart (residual blood pool). Tumors were easily detectable with ^{64}Cu-MM-DX-929 PET, with relatively ubiquitous tracer distribution at baseline.

By measuring changes in tumor SUV_{max} between baseline and post-treatment scans ($\%\Delta SUV_{max}$) we found the difference in $\%\Delta SUV_{max}$ of bev-treated tumors compared the controls to be statistically significant, p=0.0002 (Figure 2).

This trend was seen when comparing mice (data analyzed as an averaged value of both tumors per mouse), but was also true when comparing individual tumors (Figure 3). Scans from two control mice were determined to be un-evaluable due to technical issues with one or both PET images for those mice. Changes in ^{64}Cu-MM-DX-929 PET from baseline to post-treatment were noticeably different between tumors treated with bev and untreated controls. Tumors in control mice showed increased ^{64}Cu-MM-DX-929 retention after seven days compared to baseline images (Figure 4). Although these tumors often continued to grow between baseline and subsequent scans, increases in ^{64}Cu-MM-DX-929 tumor accumulation was independent of individual tumor size or growth rate (data not shown). In mice treated with bev, however, ^{64}Cu-MM-DX-929 delivery to tumor tissues appeared to remain stable between baseline and post-treatment scans (Figure 5). Again, these trends were independent of tumor size or growth rate (data not shown).

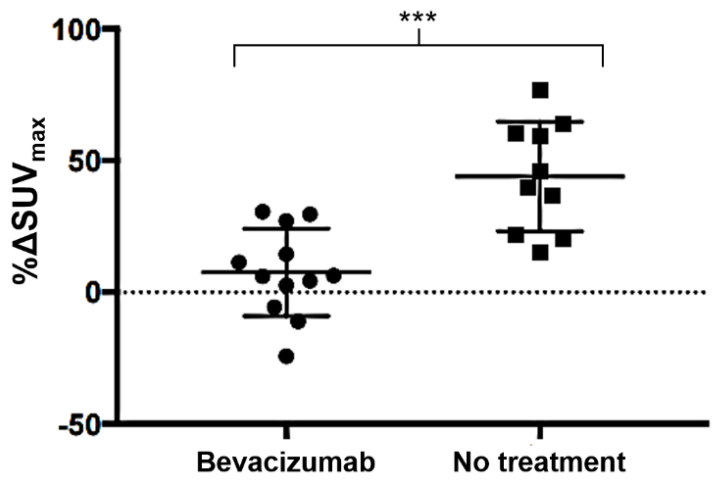

Figure 2. Changes in SUV_{max} of HT-29 colon tumors decreased after treatment with bev compared to untreated tumors. $\%\Delta SUV_{max}$ of liposome accumulation in tumor tissues of mice which received no treatment (n=10), compared to mice treated with two doses of bev (n=12) as measured by ^{64}Cu-MM-DX-929 PET. $\%\Delta SUV_{max}$ values represent the average $\%\Delta SUV_{max}$ of both tumors within an individual mouse. (****p=0.0002*)

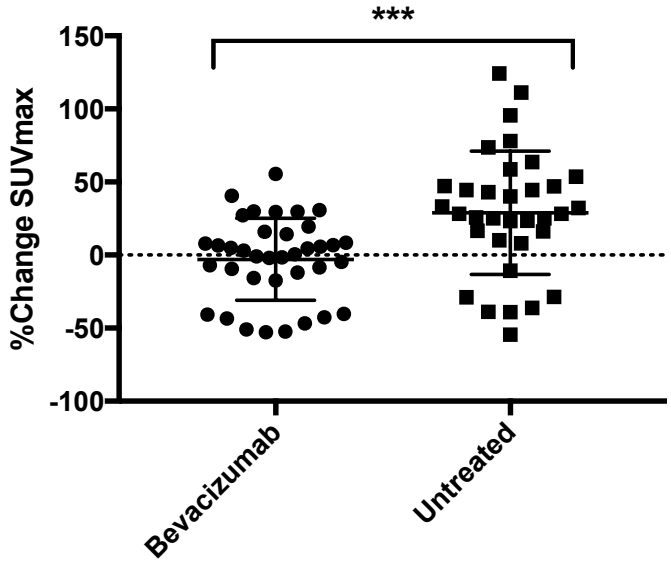

Figure 3. SUV_{max} of individual tumors decreased after treatment with bev compared to untreated tumors. Change in SUV_{max} values measured in individual HT-29 tumor xenografts after two injections of bev compared to untreated tumors. (p=0.0003)

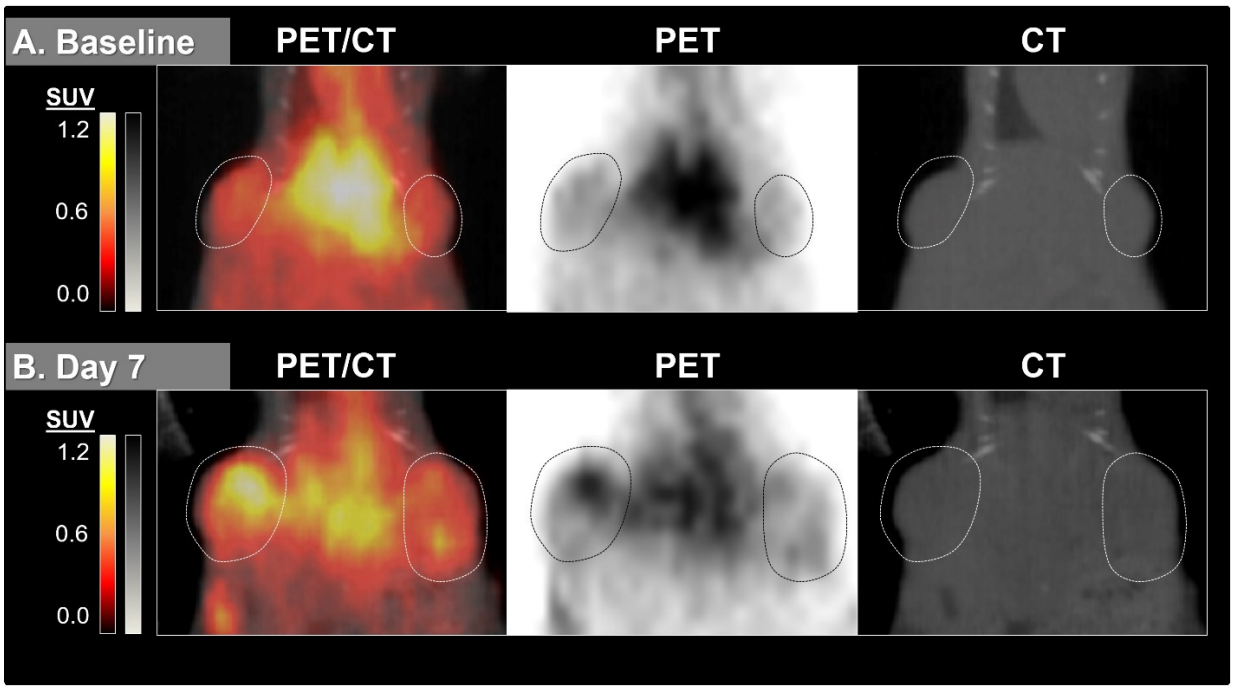

Figure 4. ^{64}Cu-MM-DX-929 delivery to HT-29 colon tumor xenografts increases after 7 days without therapeutic intervention. ^{64}Cu-MM-DX-929 scans of a mouse bearing two subcutaneous HT-29 colon xenografts (outlined) at baseline (A) and after seven days with no treatment (B). Images are coronal slices of the mouse midsection with fused PET/CT, PET alone, and CT alone. PET images were scaled from ½ background (kBq/cc) to liver average (kBq/cc) calculated based on average values from both scans.

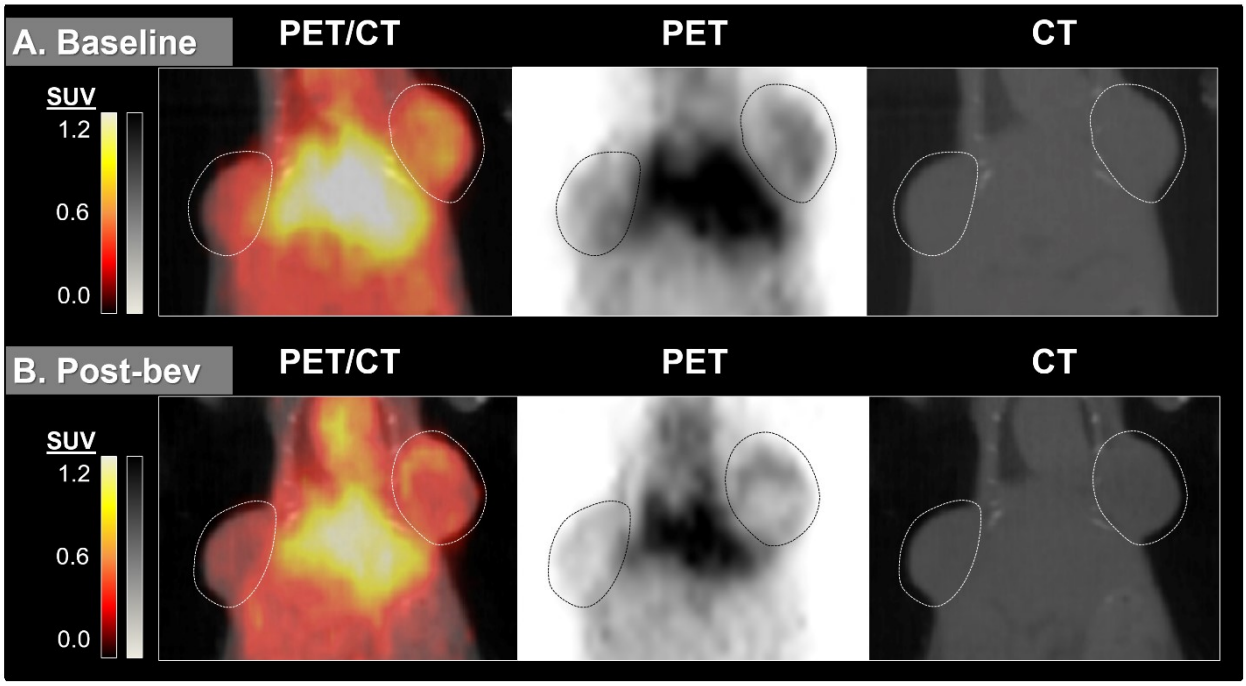

Figure 5. ^{64}Cu-MM-DX-929 delivery to HT-29 colon tumor xenografts does not increase when treated with two doses of bevacizumab. ^{64}Cu-MM-DX-929 scans of a mouse bearing two subcutaneous HT-29 colon xenografts (outlined) at baseline (A) and after seven days of bev treatment (B). Images are coronal slices of the mouse midsection with fused PET/CT, PET alone, and CT alone. PET images were scaled from ½ background (kBq/cc) to liver average (kBq/cc) calculated based on average values from both scans.

Interestingly, ^{64}Cu-MM-DX-929 PET scans visualized more frequent and dramatic shifts in the volumetric distribution of tracer across the mass of tumors treated with bev. This suggests that early into treatment, prior to measurable morphological differences, ^{64}Cu-MM-DX-929 PET identified altered tumor vascularity in bev-treated tumors, as well as early effects of bev on LP distribution. ^{64}Cu-MM-DX-929 PET images suggest that the early effects of bev may substantially alter or limit LP penetration into tumor tissues. Additionally, changes in tracer deposition in individual tumors were more highly variable in bev-treated tumors, while control tumors often exhibited similar increases in uptake over time (Figure 6). Taken together, ^{64}Cu-MM-DX-929 PET was able to detect increased LP accumulation/delivery in colon tumor xenografts tended to increase as tumors progressed without intervention, but this trend was reduced or abolished with only two doses of bev. Thus, with ^{64}Cu-MM-DX-929 PET we were able to measure the effects of bev therapy on LP delivery to solid tumors early into treatment.

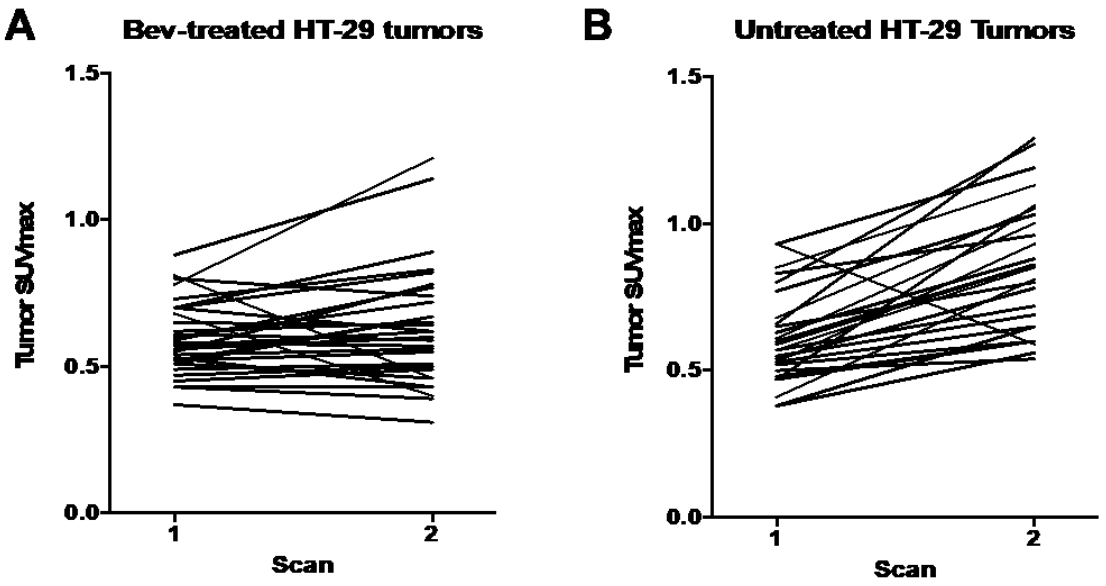

Figure 6. Changes in HT-29 tumor SUV_{max} values measured with ^{64}Cu-MM-DX-929 PET. Lines represent SUV_{max} values for individual tumors in mice treated with bev (A) or tumors in untreated mice (B).

3.2. Bevacizumab does not alter systemic distribution of ^{64}Cu-MM-DX-929 in non-tumor tissues

Any treatment with the potential to alter systemic distribution of a PET tracer could confound image analysis and uptake quantitation. To verify that bev did not significantly alter ^{64}Cu-MM-DX-929 global uptake in tissues, activity in normal tissues (resected immediately following the second PET of selected mice) was measure by gamma spectroscopy and compared between treated and untreated mice. No significant differences were detected between normal tissues of bev-treated mice and control mice (Figure 7). This demonstrates that systemic distribution was not altered in a way which would be confounding for image analysis in tissues of interest.

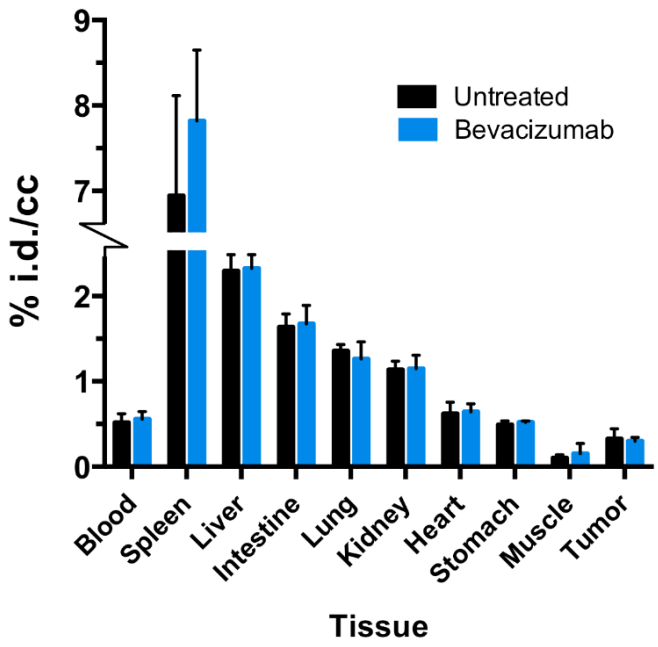

Figure 7. Bev treatment did not change overall biodistribution of ^{64}Cu-MM-DX-929. %injected radioactive dose per gram of resected tissues was measured directly after the second ^{64}Cu-MM-DX-929 PET scan.

3.3. Colon tumor growth was delayed by short-term bev alone, liposomal irinotecan alone, or short-term bev followed by liposomal irinotecan

Following the second ^{64}Cu-MM-DX-929 PET, bev-treated mice and untreated mice were further randomized into the following subsets: (1) untreated controls (n=6); (2) short-term bev (2q7d) only (n=6); (3) LP-I only (n=6); (4) short-term bev followed by LP-I (n=6) (Figure 1). One mouse assigned to receive LP-I only (group 3) was not included in data assessments due to lack of drug availability at the time of study. Mice were treated and tumor progression was monitored until tumor burden or weight loss warranted euthanasia. Tumor growth was considered individually, as well as by per-mouse analysis of total tumor burden.

As expected, HT-29 tumors in mice which received no treatment exhibited unrestrained growth (Figure 8A). Treatment with two doses of bev resulted in a measurable but modest delay in tumor progression compared to controls. Interestingly, tumors in mice treated with LP-I also exhibited delayed growth compared to controls, despite being administered later than bev, at advanced stage of disease. Succeeding short-term bev with LP-I demonstrated tumor inhibition compared to untreated controls, although there was no notable therapeutic advantage to this combination compared to bev or liposomal irinotecan alone with the specific doses and regimens tested.

As was seen in the PET scans with bev, individual tumor and mouse responses varied in each of the treatment groups. Spaghetti plots of tumor burden in individual mice show that while untreated tumors progressed similarly quickly, each treatment regimen yielded variable rates of response in individuals (Figure 8Ca-d). Tumor growth rates and drug-induced growth inhibition were independent

of tumor size at treatment initiation (data not shown). When measuring tumor latency to 1 gram total burden per mouse, each treatment group shows increased latency compared to untreated controls, though the differences in group medians were not statistically significant (Figure 8B).

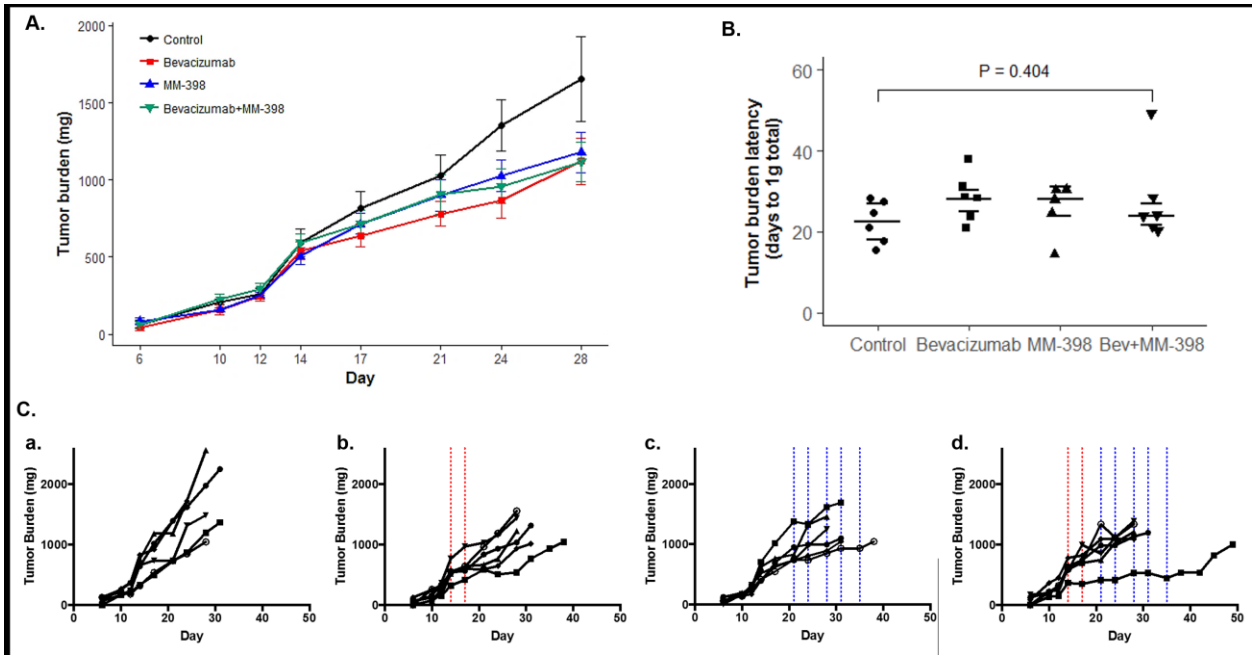

Figure 8. HT-29 tumor growth is affected by bev, LP-I, and bev followed by LP-I compared to untreated controls. Tumor growth inhibition assessed by caliper measurements represented for each treatment group compared to control, represented as a mixed linear model (****p<0.0001) (A). Tumor latency to approximately 1 gram total tumor burden was assessed for individual mice as a measure of growth delay due to treatment (B). Spaghetti plots of tumor growth in individual mice according to treatment with bev (C.b), LP-I (C.c), or bev followed by LP-I (C.d) compared to control tumors (C.a). Bev administration is indicated by red lines, LP-I administration is indicated by blue lines.

3.4. Bev treatment induced measurable changes in tumor blood vessels after two injections

Although treated mice received only two injections of bev, HT-29 tumors resected after the second ^{64}Cu-MM-DX-929/PET showed early evidence of bev response. Microvessel density (MVD) was assessed via immunohistochemical staining for CD34, followed by blinded analysis of tissues for vessel number and average diameter. CD34 staining revealed notable differences in vessel size between bev-treated and control tumors (Figure 9A). Short-term bev resulted in significantly smaller vessel diameters compared to untreated controls (Figure 9B). The total tissue area occupied by CD34+ vessels in treated tumors was 3.8% ± 1.5% compared to 5.7% ± 1.7% in control tumors ($p=0.04$, Figure 10). This indicates that ^{64}Cu-MM-DX-929 in the blood pool has a very small contribution to the tumor tracer activity. While the size of the vessels was noticeably altered following bev, the vessel density (vessels/cm^3) showed no measurable difference between bev-treated and untreated tumors (Figure 9C). These data would indicate that two injections of bev had begun eliciting an anti-vascular effect, and that the second ^{64}Cu-MM-DX-929 PET was performed during the early stages of bev response. Taken together with trends seen in PET, these data show that ^{64}Cu-MM-DX-929 PET was able to measure changes in LP delivery which were likely due to the early effects of bev. Importantly, while bev-induced changes in vessel diameter were measurable at the time of the second PET, no difference was seen in tumor growth rates between treated and control mice (Figure 8A). Thus, ^{64}Cu-MM-DX-929 PET was able to measure early fluctuations in LP delivery due to anti-vascular therapy, prior to any quantifiable changes to tumor morphology.

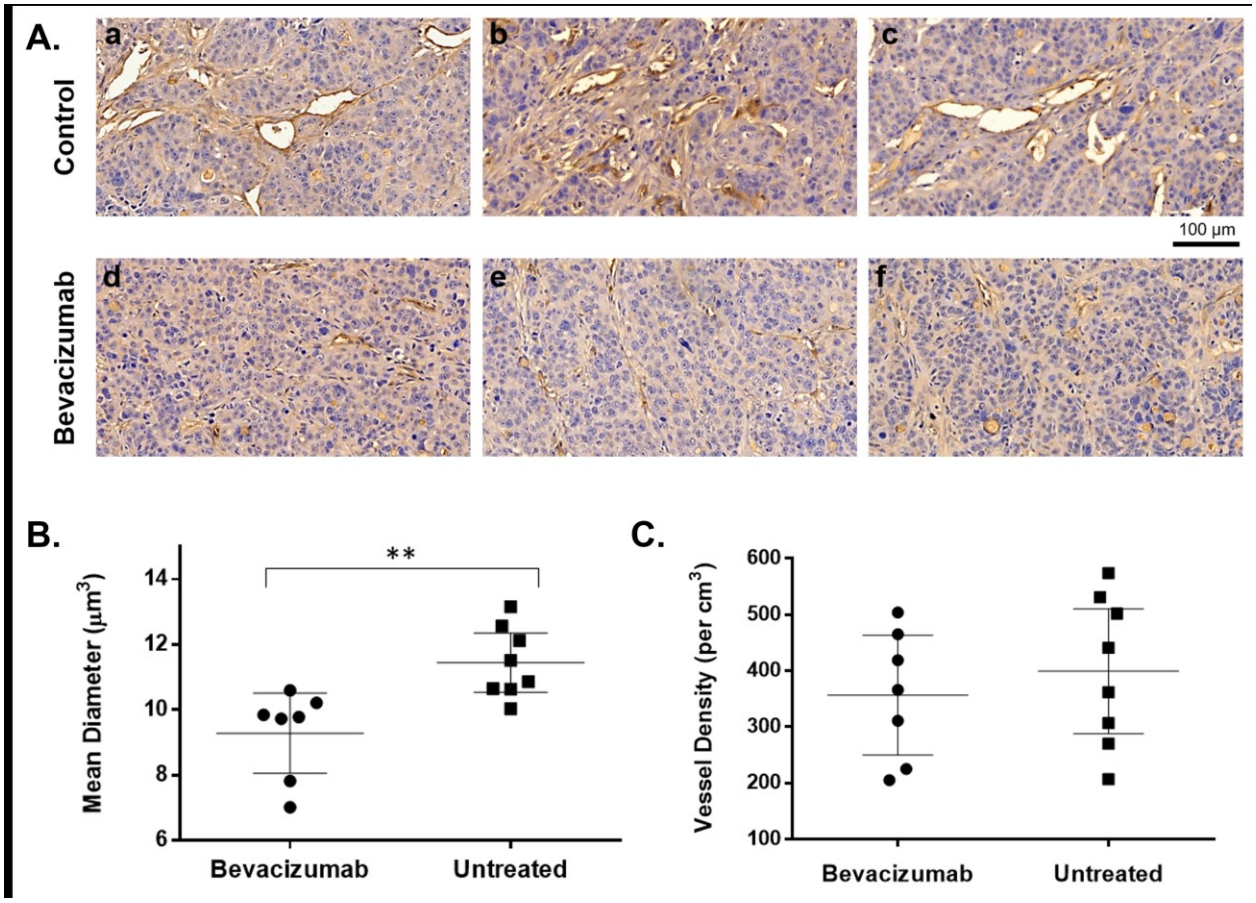

Figure 9. Bev induced significant changes in blood vessel diameter early into treatment. 20X images of HT-29 tumor tissues stained with CD34 to identify blood vessels (brown) and hematoxylin to denote cell nuclei (blue) show significant differences in vessel size between untreated controls (A. a-c) and tumors treated with bevacizumab (A. d-f). Microvessel density analysis of blood vessel diameter in bev-treated tumors compared to untreated controls (B). Vessel density (vessels per cm^3) was compared between treated and untreated tumors (C). Data are presented as mean ± SD. **p=0.0042

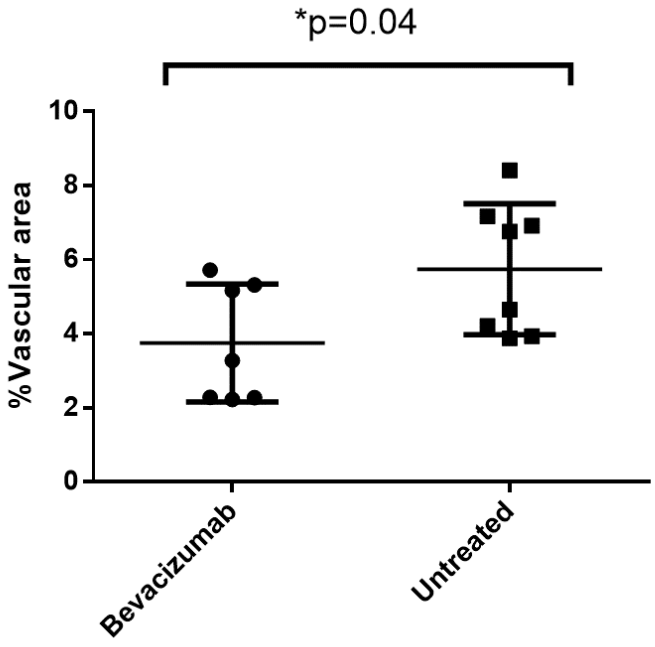

Figure 10. Percentage of total tissue area occupied by CD34 positive vessels in untreated and bev treated tumors. CD34 positive vessels were identified and diameters measured over a total of 1 cm^2 of tumor. Total vascular space per sample was determined by summation of the areas occupied by each vessel, as a percentage of total surveyed area. This can be represented as $A_{vasc} = (\Sigma[\pi*(d/2)^2]_{1\rightarrow n})/cm^2$.

3.5. ^{64}Cu-LP do not associate with macrophages and are stable in circulation for up to 48 hours.

In certain instances, macrophages have been found to take up NP such as liposomes (169). When utilizing LP for imaging, significant macrophage engulfment of tracer-LP can confound image interpretation. To determine the probability of macrophage interference with ^{64}Cu-MM-DX-929 for PET in patients, we measured macrophage uptake of ^{64}Cu-MM-DX-929 and a structurally related LP under clinical investigation, ^{64}Cu-MM-302, in human whole blood. Following incubation with either labeled liposome for 1 hour, blood cell populations were measured for radioactivity (Table 3). Radioactivity remained in the plasma, with little to no activity associated with monocyte populations. The same results were found when analyzing ^{64}Cu-MM-302 in blood samples from patients receiving ^{64}Cu-MM-302 PET (representative patient #300-1055 presented in Table 3). Blood samples taken at 1, 24, and 48 hours demonstrated that activity remained in the plasma for at least 48 hours (representative patient #300-1055; Figure 11A). HPLC analysis of LP stability was performed following ^{64}Cu-MM-302 injection in patients, which demonstrated that activity remains within LP for at least 48 hours (representative patient #300-1055; Figure 11B). Thus, ^{64}Cu-MM-302 was stable and remained in the plasma for at least 48 hours, suggesting that ^{64}Cu-LP PET at 24 hours (or later) should not confounded by free ^{64}Cu or macrophage engulfment of LP.

Table 3. %^{64}Cu-LP activity in human whole blood associated with blood cell populations.

	MM-DX-929 in whole blood (1 hr)	MM-302 in whole blood (1 hr)	MM-302 Patient: 300-1055
Plasma	97.9%	94.1%	98.5%
RBCs	2.0%	1.4%	1.1%
Lymphocytes	0.1%	3.8%	0.4%
Macrophages	0.0%	0.7%	0.0%

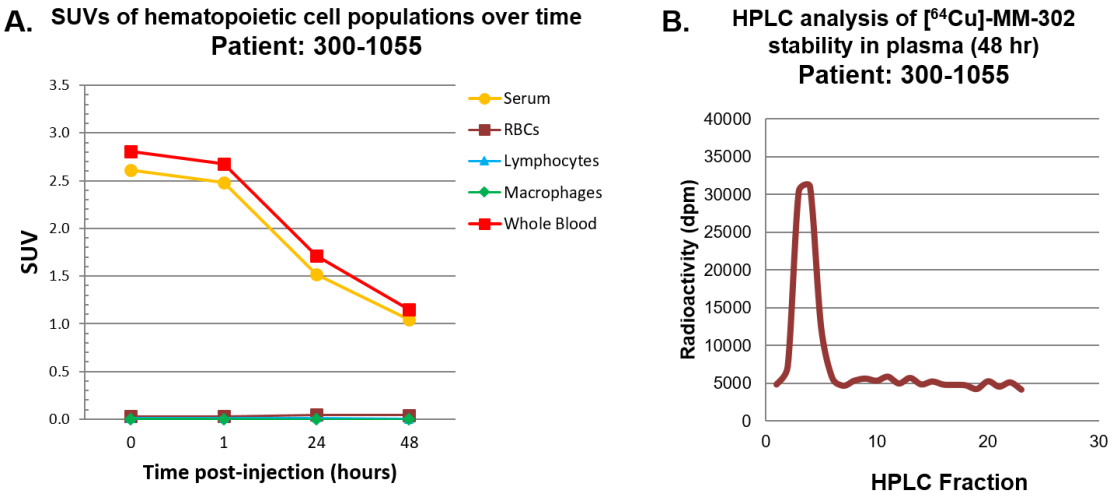

Figure 11. ^{64}Cu-LP are stable in circulation and remain in plasma for at least 48 hours. Radioactivity in blood cell populations was assessed in patients who received ^{64}Cu-MM-302 PET at time 0, 1, 24, and 48 hours. Data from a representative patient (#300-1055) is shown. Activity in blood fractions is plotted compared for each time point compared to whole blood (A), and HPLC analysis of ^{64}Cu association with LP is shown at 48 hours post-injection (B) (previously published in (170)).

4. Discussion

The urgent need for precision medicine for CRC is not limited to the development of more sophisticated therapies, but also techniques to predict and monitor therapeutic efficacy. Here we have demonstrated the utility of a dynamic system using ^{64}Cu-labeled liposomes for PET to non-invasively measure the early effects of bev therapy on LP delivery to colon tumor xenografts in mice. Furthermore, significant differences measured with ^{64}Cu-MM-DX-929 PET between bev-treated and control tumors provided early insight into therapeutic outcomes in mice subsequently treated with liposomal irinotecan.

Clinically, the potential advantages of LP are twofold: (1) sustained and/or local delivery of drugs or drug combinations to tumor tissues, and (2) reduced toxicity profiles as normal tissues are shielded from toxic drugs (45, 171-174). However, heterogeneous, inconsistent, or obstructed delivery of these nanoparticles to tumor tissues can hamper their effectiveness, and is hypothesized to be a contributor to the lack of clinical success seen with many LP. Passive targeting through EPR relies on specific properties of tumor blood vessels, which are constantly changing in response to the tumor environment and therapeutic intervention, particularly with antivascular agents. While antivascular agents are expected to disrupt tumor vessels, there is some evidence suggesting that early effects of bev treatment may transiently “normalize” tumor vessels, though these effects are not consistent (164, 175-177). Thus, a non-invasive means of measuring LP delivery to tumor tissues could provide individualized information on

the effect of drugs like bev on LP delivery and subsequent efficacy (17, 165, 170, 178).

In these studies, we found that we could use PET to quantify changes in LP accumulation in colon tumor xenografts very early into bev treatment. In mice that received no treatment in between PET scans, ^{64}Cu-MM-DX-929 accumulation in tumors increased, indicating that LP-I were still able to reach and penetrate HT-29 tumor tissues and elicit an effect. While previous studies of LP-I in HT-29 tumors demonstrated significant anti-tumor effects when administered earlier into tumor progression (179, 180), the modest effects seen here were likely attributed to treatment initiation at late-stage disease. Because of this, we anticipated no significant difference in survival among the treatment groups. After two injections over the course of one week, bev had already begun eliciting anti-vascular effects, which were quantifiable with ^{64}Cu-MM-DX-929 PET. While bev treatment conferred therapeutic advantage in HT-29 tumors, ^{64}Cu-MM-DX-929 PET showed that even short-term bev treatment began to impede liposome delivery and penetration. This observation is consistent with the lack of therapeutic benefit seen in treating mice with LP-I which had already received bev.

In the clinic, bev and other antivascular agents, such as ziv-aflibercept (Zaltrap®; Regenron Pharmaceuticals Inc., Tarrytown, NY), are approved to treat patients with CRC. As liposome-based therapies are introduced for this population, understanding the effects of antivascular agents on LP delivery could reduce the probability of employing incompatible drug combinations. Furthermore, when designing clinical trials of LP-drug platforms for colon cancer, imaging

techniques could be used to non-invasively monitor changes in LP delivery over time, or as a result of various therapies.

Along with the clinical implications of bev and LP-therapy in CRC patients, we have been able to employ a powerful model for dynamically assessing modulation of LP delivery. ^{64}Cu-MM-DX-929 PET was able to non-invasively quantify the effects of bev on LP delivery, which likely affected subsequent therapy with liposomal irinotecan injection. This would suggest that ^{64}Cu-MM-DX-929 PET may be sensitive enough to detect and monitor changes in LP delivery to solid tumors which may directly influence therapeutic LP efficacy. Aspects of the tumor environment which affect LP distribution are dynamic, and are certain to vary among patient populations. Thus, predicting and monitoring LP delivery with a non-invasive theranostic imaging is an invaluable tool in achieving precision medicine with LP for CRC patients.

Finally, the mission of individualized treatment plans for patients with cancer is one that requires a significant preclinical effort to identify diagnostic and therapeutic strategies. In this study, we have demonstrated a practical system for measuring therapeutic modulation of LP delivery that predicted and described subsequent therapeutic results. ^{64}Cu-MM-DX-929 PET may be used in preclinical studies of therapeutic LP to efficiently measure the effect of combination therapies, treatment timelines/conditions, etc. on LP delivery. Utilizing imaging protocols with tracer LP like ^{64}Cu-MM-DX-929 can quickly and non-invasively identify treatment conditions which improve or hinder LP delivery. In CRC, this could mean creating

more avenues towards precision medicine with liposomes to improve outcomes for patients.

CHAPTER 3. ^{18}F-FMAU PET TO EVALUATE RESPONSE TO CISPLATIN IN PRE-CLINICAL LUNG CANCER STUDIES

1. Introduction

With the success of ^{18}F-FLT PET in oncological imaging, a variety of radiolabeled thymidine analogues have been synthesized for assessment in imaging studies (103). Among these, ^{18}F-FMAU is of particular interest. While ^{18}F-FLT lacks the 3' hydroxyl group on natural thymidine causing termination of DNA strand elongation, ^{18}F-FMAU maintains a 3' hydroxyl group and can be incorporated into DNA (106). Early research into the utility of ^{18}F-FMAU for PET suggested that FMAU had lower uptake in bone marrow compared to ^{18}F-FLT (110). In multiple tumor types, metastases to the bone are common, and would be easier to identify in scans with a tracer that demonstrates lower background in the marrow. Thus, ^{18}F-FMAU was studied as a potential alternative to ^{18}F-FLT for PET of cellular proliferation in oncology (181, 182).

Natural thymidine is incorporated into dividing cells through the DNA salvage pathway (183). After cellular uptake, thymidine molecules (as well as functional analogues) undergo phosphorylation by thymidine kinases, which prevents transport out of the cell. Two forms of thymidine kinases are present in human cells, namely thymidine kinase 1 (TK1) and thymidine kinase 2 (TK2) (184). TK1 is primarily located in the cytoplasm, and its activity is strongly associated with the S phase of the cell cycle during nuclear DNA synthesis (185). Conversely, TK2 activity is relatively low and ubiquitous compared to TK1, and TK2 is closely associated with mitochondrial DNA synthesis (186). In vitro studies have demonstrated that FLT is predominantly phosphorylated by TK1, with strong

retention in actively dividing cell populations (187). Conversely, FMAU is predominantly phosphorylated by TK2, and is not as highly retained as FLT in proliferative tissues (102). Thus, while ^{18}F-FLT PET is considered a means of measuring tumor proliferation, ^{18}F-FMAU PET may offer a different perspective on cancer cell metabolism.

Mitochondrial metabolism, a critical determinant of cellular energy production, is often dramatically altered in tumor cells. Further, dynamic and transient shifts in mitochondrial biochemistry are being investigated as biomarkers for understanding tumor ATP synthesis, fatty acid oxidation, apoptosis signaling, synthesis of nucleotides, and more (188-190). Heterogeneity of mitochondrial biology in human tumors complicates the use of mitochondrial metabolism as a biomarker for cancer (191). However, measuring mitochondrial changes that result from treatment could provide insight into therapeutic effects on tumor metabolism (192, 193). It is conceivable that, while ^{18}F-FMAU is a less attractive choice for measuring proliferation with PET, ^{18}F-FMAU PET may be useful in measuring mitochondria-related effects in tumors.

Previous work in our lab, performed by Tehrani *et al.*, provided evidence that FMAU uptake in tumor cells may be associated with cell stress (102). Following exposure to nutritional stress, prostrate and breast cancer cell lines exhibited increased FMAU retention while FLT retention and TK1 activity decreased. FMAU retention was also increased in cells exposed to oxidative and reductive stresses, and correlated with mitochondrial mass measured in the cells. These data provide rationale for the study of ^{18}F-FMAU PET as a measure of

cellular stress, particularly energy metabolism stress which occurs early into treatment. We chose to measure the early effects of cisplatin treatment in human lung tumor models with ^{18}F-FMAU PET.

2. Materials and Methods

Materials

NCI-H460 cells, NCI-H292 cells, and Roswell Park Memorial Institute (RPMI)-1640 medium were purchased from ATCC (Manassas, VA) and kept below 15 passages following receipt. For in vitro studies with cisplatin, cis-Diammineplatinum(II) dichloride was purchased form Sigma Aldrich (St. Louis, MO). HPLC analysis of blood samples was performed using Hypersil C18 columns (Thermo Fisher Scientific, Waltham, MA). Gamma spectroscopy measurements were acquired with a Packard Cobra II gamma counter (Perkin-Elmer Inc., Waltham, MA). An R4 microPET (Concorde Microsystems, Knoxville, TN) was used for all animal PET scan acquisition. PMOD Image Matching and Fusion Tool ver3.6 (PMOD group, Switzerland) was utilized for image registration, matching, and analysis. Statistical analyses were performed using GraphPad Prism, ver7 (GraphPad Software Inc., La Jolla, CA).

Cell Culture

H460 large cell lung carcinoma cells and H292 mucoepidermoid pulmonary carcinoma cells cultured in RPMI-1640 medium supplemented with 5% fetal bovine serum and 1% penicillin/streptomycin, as described by ATCC. Cells were kept at 37°C with 5% CO_2 and were passaged with trypsin when cells reached approximately 80% confluence. Prior to inoculation in mice, cells were not

passaged more than ten times in culture. Cell line identity was authenticated at time of all studies with the PowerPlex® 16 System from Promega (Madison, WI) in the Applied Genomics Technology Center at Wayne State University. Analyses were performed using ATCC and DSMZ reported short tandom repeat loci for the cell lines.

Cell Line Sensitivity to Cisplatin

In order to establish the difference in cisplatin sensitivity between H460 and H292 cells, 5 day MTT assays were performed to determine IC_{50} values. Cisplatin (cis-Diammineplatinum(II) dichloride) was dissolved in sterile PBS and sonicated for 30 minutes at 37˚C until dissolved prior to generating series dilutions in culture medium. Cisplatin concentrations which resulted in a 50% loss of cell viability (IC_{50}) after 5 days was determined independently for each cell line. These concentrations of cisplatin were used for all in vitro tracer uptake assays.

^{18}F-FMAU Uptake in Cells Treated With Cisplatin

H460 and H292 cells were seeded in 6-well plates (900,000 and 1.8 million, respectively, due to doubling time). Cells were allowed to reach approximately 50% confluency (exponential growth phase) under normal culture conditions. Cells were exposed to IC_{50} concentrations of cisplatin (as determined by 5-day MTT) or vehicle (PBS) in complete culture medium for 24 hours. Following treatment, drug- or vehicle-containing medium was removed and cells were exposed to ^{18}F-FMAU in medium for 1 hour (approximately 0.05 uCi/well), at 37 ˚C and 5% CO_2. ^{18}F-FMAU medium was carefully collected and cells were washed three times with ice-cold PBS (between 2-4˚C) to impede any subsequent transmembrane transport or

tracer phosphorylation, and remove residual free tracer. Cells were lysed with 1M KOH and collected, and all fractions were measured with gamma scintigraphy. Cellular uptake of ^{18}F-FMAU was compared in both cell lines between cisplatin- and vehicle-treated cells.

Animal Studies

Tumor model: Cultured H460 and H292 cells grown in complete culture medium were used to establish subcutaneous tumor models in female SCID NCr mice (Charles River Labs; MA), via suspension in Matrigel prior to inoculation. Tumors were maintained in serial passage, via inoculation with H460 or H292 tumor fragments subcutaneously by trochar, over the course of experiments. All imaging studies were performed within 5 tumor passages in mice.

MicroPET studies: Schematic representation of mouse study design is presented in (Figure 12). Tumors were allowed to grow until they we approximately 250mg (range: 200-300mg) based on the growth rates of each tumor type. Animals were randomized into their respective control (No Rx) and treatment groups (cisplatin). All mice were imaged with microPET before and 24±2 hours after a single injection of cisplatin. Scans were compared for changes in tracer uptake in tissues of interest. Mice were euthanized under anesthesia with whole blood and tissues collected after the second PET for HPLC analysis and biodistribution measurements, respectively. All mice were weighed and observed daily for the duration of the study. Tumors were measured by caliper 2-3x/weekly with the formula [volume (mg) = length (mm) x width^2 (mm^2)/2] used to calculate tumor mass.

Tracer preparation and injection: ^{18}F-FMAU was synthesized as described previously (103). To achieve similar injected activity and volume, ^{18}F-FMAU was diluted in sterile saline when necessary. Mice were administered 200-300 uCi/injection intravenously (IV) within a 0.1 to 0.3 ml volume range.

Drug preparation: Cisplatin was freshly prepared for each injection from stock diluted with 0.9% sterile saline, pH 6.0 and injected IV at 11 mg/kg in a volume of approximately 0.2ml/20g mouse. Cisplatin injections were administered immediately following the first PET scan, after the mouse had fully recovered from anesthesia. Cisplatin treatment consisted solely of a single injection, and effects were assessed via PET after 24 ± 2 hours.

All animal studies were approved by and performed in strict accordance with the policies of the Institutional Animal Care and Use Committee (IACUC) at Wayne State University.

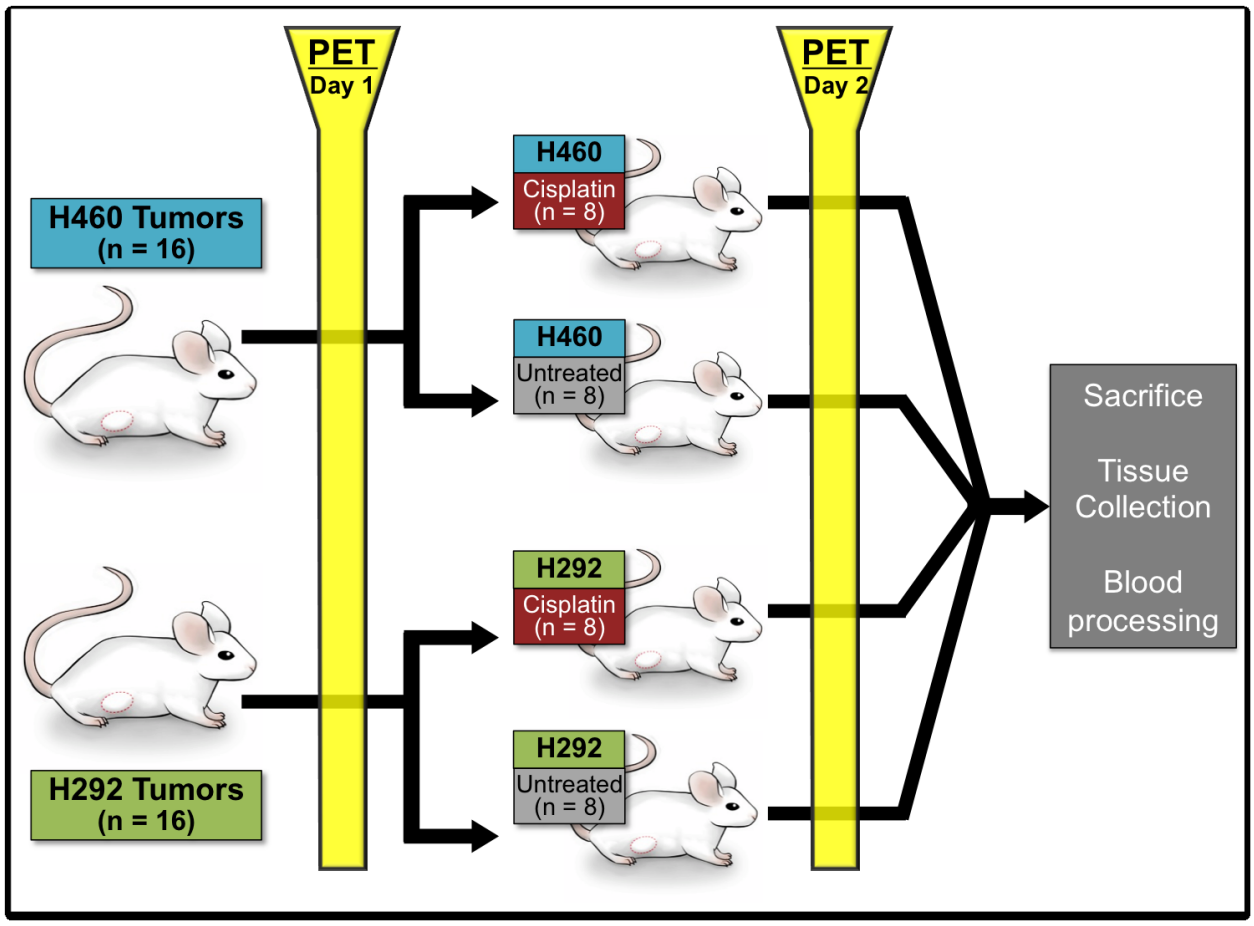

Figure 12. Schematic representation of FMAU mouse study design. Mice bearing H460 or H292 tumors were randomized to treatment groups, with half of the mice receiving IV cisplatin following the first PET. All mice were scanned again, approximately 24 hours after the first PET.

Animal Imaging with ^{18}F-FMAU PET

Following receipt of ^{18}F-FMAU mice received approximately 200-300 µCi of ^{18}F-FMAU intravenously via the tail vein. Whole body PET images were acquired one hour after IV administration of ^{18}F-FMAU. Dynamic images of representative animals from each treatment group were acquired immediately after tracer injection for 60 minutes, followed by a 10 minute whole body scan. Anesthesia for image acquisition was induced with 3% inhaled isoflurane prior to placement on the scanner, and maintained during scanning with 2% isoflurane. Mice were imaged in a prone position on the scanner bed with heating to maintain body temperature.

Attenuation correction based on routine transmission scans was performed on the whole body microPET images. Images were reconstructed by applying an iterative ordered-subsets expectation maximization 2-dimensional algorithm (167) and corrected for scatter. These parameters yield an isotropic spatial resolution of approximately 2mm in full width at half maximum (168). Prior to study, a phantom for ^{18}F was scanned to calculate conversion from counts/pixel/minute to kBq(µCi)/cm^3.

PET/CT Image Registration and Analysis

PET and CT images were registered and aligned using the PMOD Image Matching and Fusion Tool ver3.6 (PMOD group, Switzerland). Regions of interest (ROIs) were defined manually on individual planes of the PET. 3-dimensional volumes of interest (VOIs) were generated from the stacked ROIs of the tissue of

interest. Activity in the VOIs, as detected by PET in kBq(μCi)/cm^3, as well as injected dose and body weight were used to calculate standardized uptake values (SUV). SUV_{max} values were determined by averaging the max pixel value within each of the three hottest consecutive ROIs of a tissue, and normalizing to injected dose and body weight.

Whole Body Tissue Distribution of ^{18}F-FMAU

^{18}F-FMAU retention in resected tissues was assessed by gamma spectroscopy. Briefly, following the second PET scan, mice were sacrificed and tissues harvested. Resected tissues included tumor, liver, heart, lung, intestine, stomach, kidney, spleen, and whole blood. Serum from whole blood of representative animals of each treatment group was subjected to HPLC analysis. Tissues were washed, weighed, and activity was measured for one minute on a gamma counter. Activity in tissues was decay corrected to time of injection and normalized to tissue weight (kBq/cc). Activity per gram of tissue was calculated based on the injected dose of ^{18}F-FMAU. Tissue biodistribution was compared between mice treated with cisplatin and untreated controls to ensure that cisplatin treatment was not affecting systemic distribution or retention of ^{18}F-FMAU.

HPLC of Circulating ^{18}F-FMAU in Whole Blood

Following the second ^{18}F-FMAU PET, whole blood was drawn from animals post-sacrifice to determine if ^{18}F-FMAU had been metabolized during circulation time. Samples representing treated animals and untreated controls were selected for HPLC analysis of ^{18}F-FMAU, as previously described (102). Briefly, sera collected from whole blood was loaded onto a Hypersil C18 column with 6%

Acetonitrile, 10mM NaOAc, and allowed to run at a flow rate of 1 ml per minute. 0.5 ml fractions were collected and ^{18}F activity was measured via gamma scintigraphy. Curves generated from the HPLC of blood samples were compared to results from running a small aliquot of pure ^{18}F-FMAU as received prior to injection.

Statistical Analysis

Statistical analyses were performed using GraphPad Prism 7 (GraphPad Software Inc., La Jolla, CA). Data are presented as the mean ± standard deviation, unless otherwise stated. Comparisons of PET SUV data were performed using two-sample Student's t-test. A p-value of <0.05 was considered statistically significant.

3. Results

3.1. Changes in ^{18}F-FMAU uptake in lung tumor cells after cisplatin treatment differ based on cisplatin sensitivity

To assess the capacity of ^{18}F-FMAU to measure early response to cisplatin treatment, we sought to compare lung cancer cell lines with differing sensitivities to cisplatin. Multiple non-small cell cancer cell lines were subjected to MTT following treatment with cisplatin to determine relative sensitivity (data not shown). Of these, H460 cells and H292 cells were selected for further study, as these cells demonstrated a measurable difference in sensitivity to cisplatin. IC_{50} values were determined independently for H460 and H292 cells by exposing the cells to a series of cisplatin concentrations for 5 days, followed by MTT (Figure 13). H460 cells were identified as being more sensitive to cisplatin treatment (IC_{50} = 0.06 nM) than H292 cells (IC_{50} = 0.2 nM). The determined IC_{50} values were used throughout

all of the in vitro studies, representing the concentration of cisplatin which, after 5 days, would result in 50% cell death.

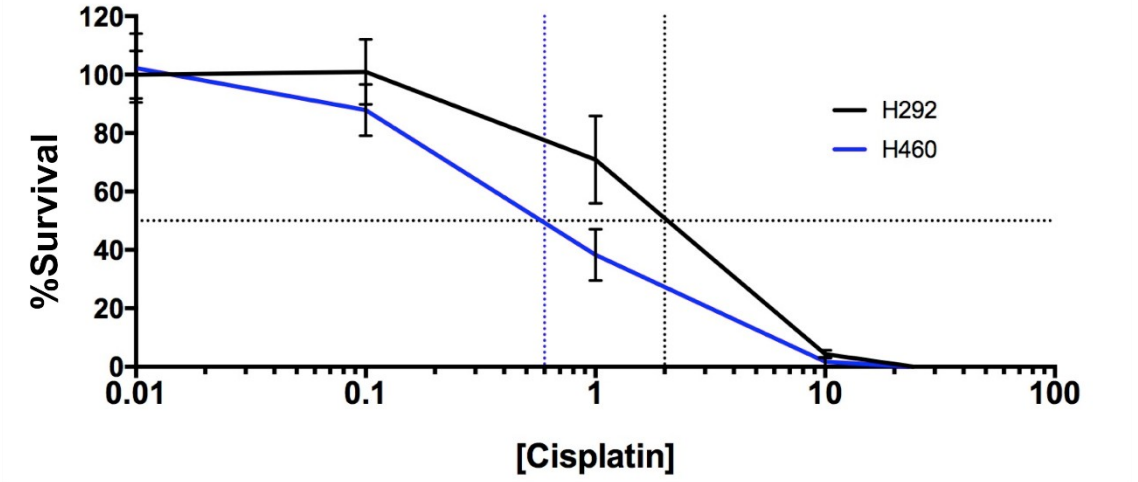

Figure 13. H460 cells are more sensitive to cisplatin-induced cell killing than H292 cells. Assessment of cell viability of H460 and H292 cells was assessed by MTT after 5 days of exposure to cisplatin concentrations in complete culture medium. IC_{50} values were determined as the concentration of cisplatin capable of causing a 50% loss of viability after 5 days. IC_{50} values were determined independently for each cell line, by which H460 cells were determined to be "cisplatin-sensitive" and H292 cells "cisplatin-resistant".

Cellular uptake assays of ^{18}F-FMAU were performed with H460 and H292 cells following exposure to cisplatin or vehicle (PBS) in complete culture medium. Cells were treated with determined IC_{50} concentrations of cisplatin for 24 hours, and subsequently exposed to cisplatin-free, complete culture medium containing ^{18}F-FMAU for 1 hour. Following multiple washes, ^{18}F-FMAU retention in cells was assessed via gamma scintigraphy. Interestingly, little change was noted in ^{18}F-FMAU retention in sensitive H460 cells following exposure to cisplatin (Figure 14A), while resistant H292 cells demonstrated significantly increased retention with treatment (Figure 14B). As expected, IC_{50} concentrations determined with 5 day MTT induced negligible reductions on cell number and viability after 24 hours, with H460 and H292 cells maintaining 100 ± 2% and 96 ± 2% viability respectively, as assessed by Trypan Blue measurements (data not shown). This indicates that differences seen in ^{18}F-FMAU uptake in cells between treated and untreated cells were not the result of significant differences in viability.

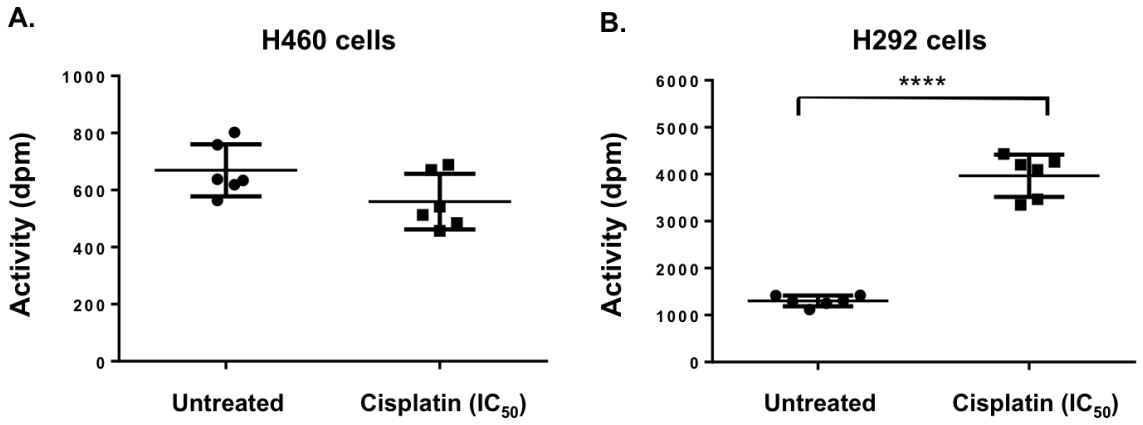

Figure 14. After 24 hours of cisplatin treatment ^{18}F-FMAU uptake increased in H292 cells but not H460 cells. Plated cells were exposed to ^{18}F-FMAU for one hour following 24 hours of cisplatin treatment (at determined IC_{50} concentrations) to measure the effect of treatment on tracer retention compared to vehicle controls. Following washes, cell-associated ^{18}F-FMAU in treated cells was quantified and normalized to uptake in untreated controls. (****$p<0.0001$).

3.2. Significant decreases in ^{18}F-FMAU uptake were observed in H460 xenografts but not H292 xenografts after 24 hours of cisplatin treatment in mice

Tumor retention of ^{18}F-FMAU following 24 hours of cisplatin treatment was assessed in vivo with microPET of female SCID NCr mice bearing H460 or H292 xenografts. Mice were scanned at baseline, prior to any treatment, 1 hour after injection of ^{18}F-FMAU. Immediately following the scan, half of the mice in each tumor group received a single injection of cisplatin at 11 mg/kg. All mice were scanned again with ^{18}F-FMAU PET 24 ± 2 hours after the baseline scan. Notable uptake was seen in tumor tissues, as well as in the bladders of some mice, indicative of clearance. Low uptake was seen in muscle tissue, which was selected for background measurements of ^{18}F-FMAU uptake. SUV_{max} values were compared between baseline scans and post-treatment scans to generate $\%\Delta SUV_{max}$ values for each individual tumor.

PET images revealed robust changes in ^{18}F-FMAU SUV_{max} in treated H460 (cisplatin-sensitive) tumors, with a mean change of -40.0% (range of -21.1% to 52.5%). This was statistically significant (****$p<0.0001$) compared to untreated H460 tumors, which showed negligible change in SUV_{max} 24 hours after baseline, with a mean of 3.73% (range of -7.4% to 12.4%) (Figure 15). Cisplatin-resistant H292 tumors, on the other hand, showed no significant change in SUV_{max} between PET scans, in both treated (mean change of -5.39%, range of -26.1% to 27.7%) and untreated tumors (mean change of -1.03%, range of -30.6% to 33.0%). SUV_{max} data were validated by assessing changes in SUV_{mean} of isocontours representing the hottest 50% of the tumor max pixel, which demonstrated the same trends seen with SUV_{max}. Cisplatin treatment did not induce critical toxicities in

any treated mice, although constipation was noted in some treated mice during necropsy after sacrifice on the second scan day.

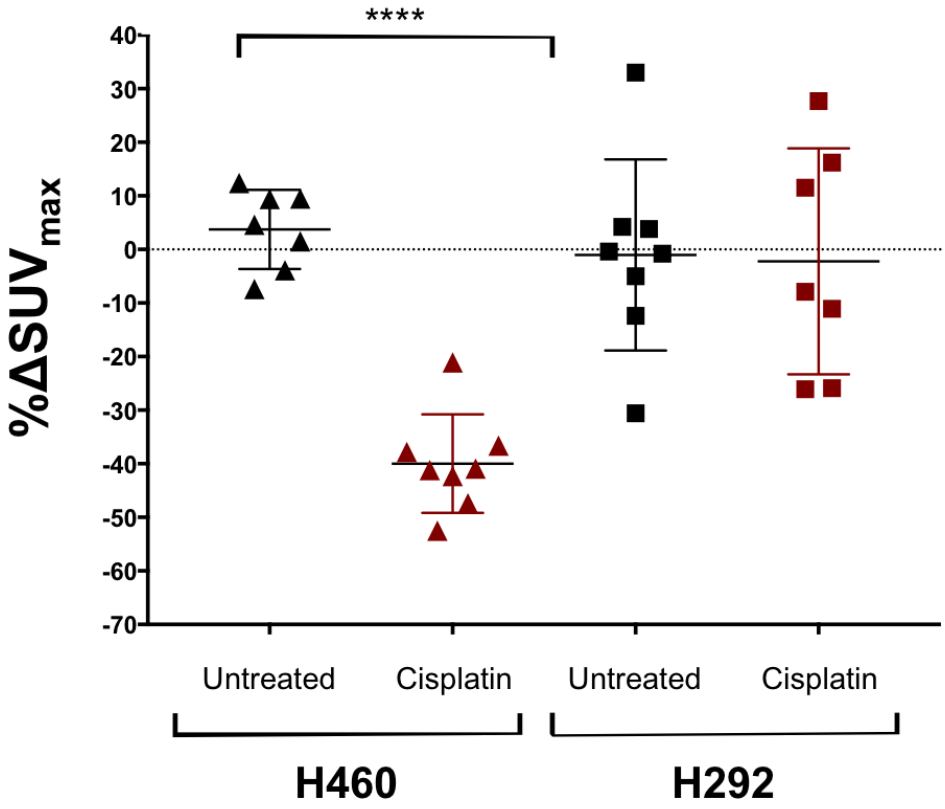

Figure 15. Cisplatin-treated H460 tumors in mice showed significant reductions in ^{18}F-FMAU uptake compared to H292 tumors imaged with PET. ^{18}F-FMAU PET scans were acquired before and after 24 hour treatment with a single injection of cisplatin in mice bearing H460 or H292 tumor xenografts. Uptake in tumor tissues was quantified as SUV_{max} values, and changes in uptake following the treatment period were calculated as $\%\Delta SUV_{max}$. (****$p<0.0001$).

^{18}F-FMAU PET images of H460 tumors visualized lower tracer uptake 24 hours after a single dose of cisplatin compared to untreated controls (Figure 16). In nearly all treated H460 tumors, this effect was evident across the entire volume of the tumor, both in the center of the mass and in the tumor periphery. In untreated H460 tumors, changes in tracer uptake were negligible to modest (mean change of -3.73%, range of -7.4% to 12.4%). Often, untreated tumors showed slight increases in ^{18}F-FMAU uptake, but this was considered within the confines of ^{18}F-FMAU PET reproducibility, as previously described (194). Unlike H460 tumors, PET of ^{18}F-FMAU uptake in cisplatin-resistant H292 tumors showed no consistent trend that could discriminate between treated and untreated tumors ($p=0.9850$) (Figure 17).

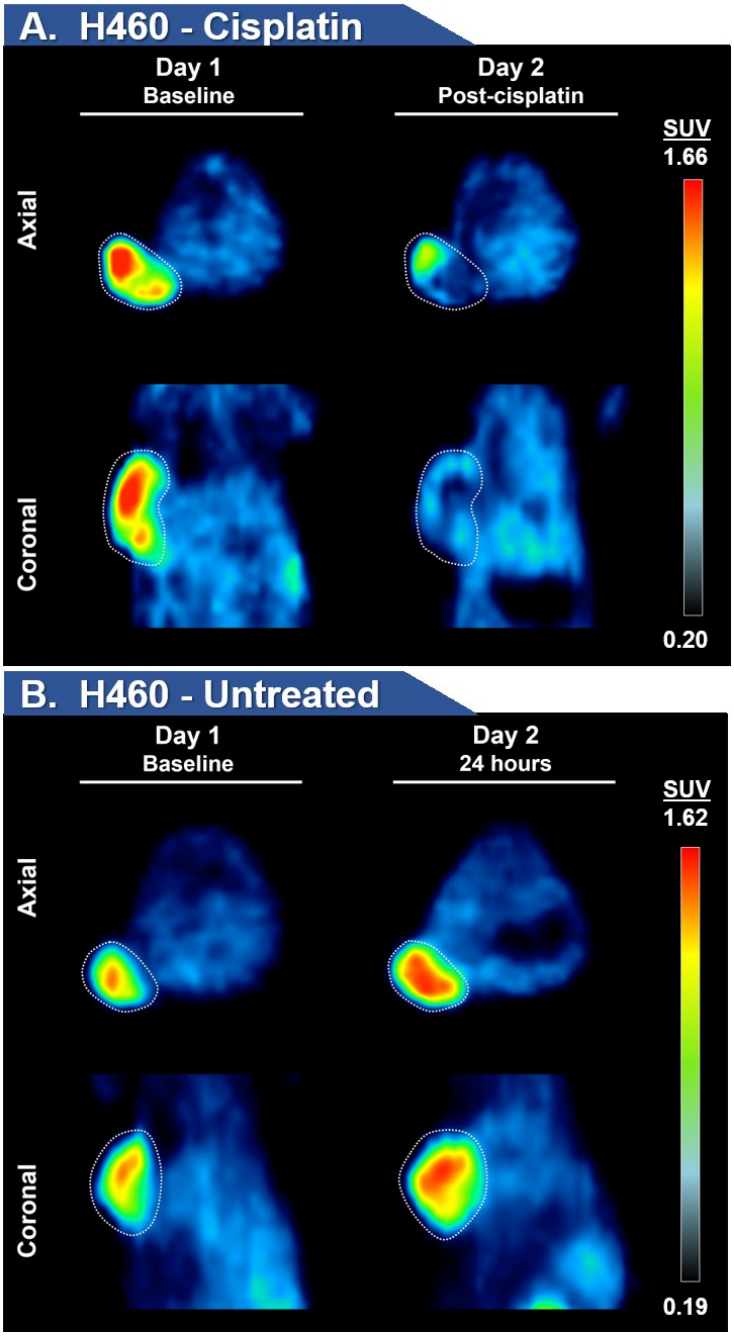

Figure 16. ^{18}F-FMAU PET scans of mice bearing H460 tumors before and after cisplatin treatment. Representative ^{18}F-FMAU scans of mice bearing H460 (cisplatin-sensitive) xenografts at baseline (left) and after 24 hours (right). Treatment with a single injection of cisplatin induced robust reductions in ^{18}F-FMAU uptake in tumors (indicated in white) (A), compared to changes in uptake seen in untreated mice (B). PET image color scale was calculated as follows: ½ background average → tumor max pixel.

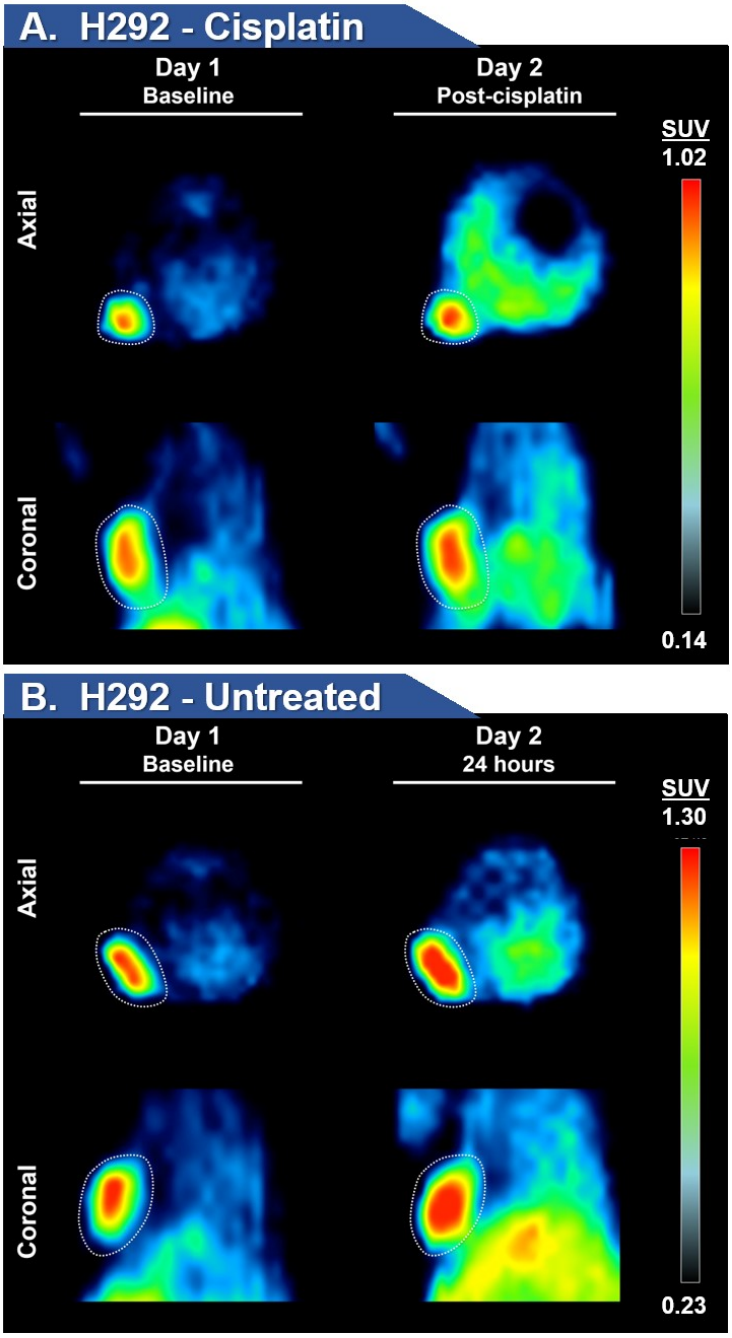

Figure 17. ^{18}F-FMAU PET scans of mice bearing H460 tumors before and after cisplatin treatment. Representative ^{18}F-FMAU scans of mice bearing H292 (cisplatin-resistant) xenografts at baseline (left) and after 24 hours (right). Treatment with a single injection of cisplatin induced negligible changes in ^{18}F-FMAU uptake in tumors (indicated in white) (A), compared to changes in uptake seen in untreated mice (B). PET image color scale was calculated as follows: ½ background average → tumor max pixel.

3.3. Systemic distribution and clearance of ^{18}F-FMAU was not affected by cisplatin treatment

Representative mice from each treatment group was measured with 60-minute dynamic scans after tracer injection to monitor ^{18}F-FMAU distribution and clearance. Time activity curves describing activity over time were generated to determine if any differences in clearance were observed in tumor, liver, and muscle between treated and untreated mice (Figure 18A and B).

To ensure that cisplatin did not alter systemic ^{18}F-FMAU distribution in a way which would affect tumor uptake, radioactivity was measured in bulk resected tissues. Following the second PET scan, mice were euthanized and resected tissues of interest were measured with gamma scintigraphy, with activity measured as %i.d./cc. Treated mice maintained slightly higher levels of activity in whole blood compared to untreated mice. In animals bearing H460 tumors, this was measured as mean normalized %i.d./gram of 2.04% ± 0.84% in blood samples of treated mice compared to 1.19% ± 0.54% in control mice. In mice bearing H292 tumors, normalized %i.d./gram of blood samples was measured as 1.31% ± 0.40% in treated mice compared to 0.84% ± 0.43% in untreated mice. However, these differences were not significant for mice bearing H292 or H460 tumors ($p=0.52$ and 0.53, respectively) (Figure 18C and D). In all groups, non-tumor tissues exhibited no significant difference between mice treated with cisplatin compared to untreated mice. This suggests that systemic tissue retention of ^{18}F-FMAU was not significantly altered by cisplatin treatment in a way which could confound tumor analysis. Resected H292 tumors showed no difference in activity between cisplatin-treated and untreated tumors. Similarly to the results seen by PET, ^{18}F-

FMAU retention in H460 tumors treated with cisplatin was significantly lower than untreated H460 tumors (*p=0.017).

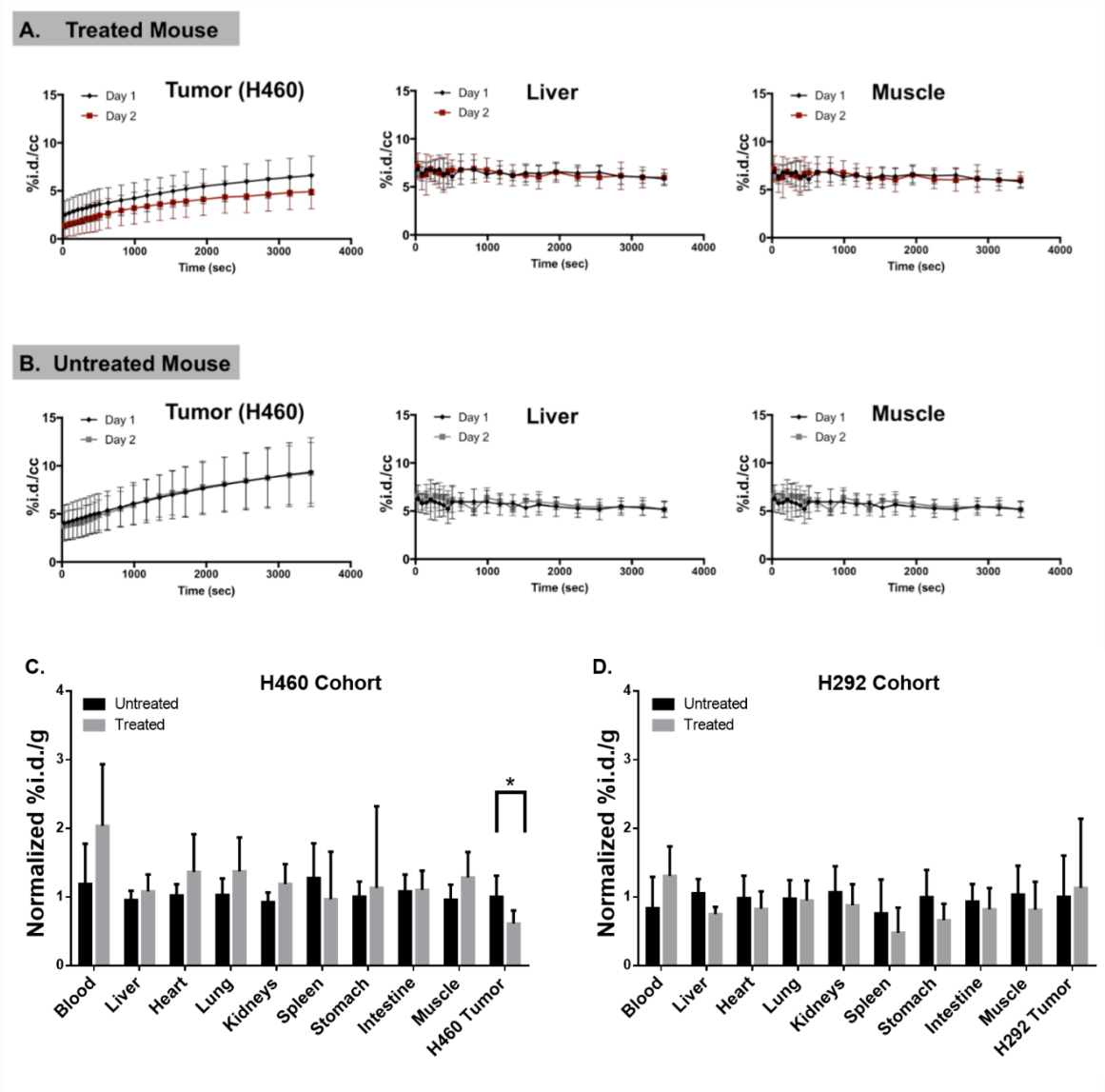

Figure 18. Cisplatin treatment did not alter clearance or biodistribution of ^{18}F-FMAU in mice. Representative curves of tracer uptake over time, as measured by 60-minute dynamic scan, in cisplatin-treated mice bearing H460 tumors demonstrate that ^{18}F-FMAU clearance is not altered in liver or muscle tissues (A) compared to tissues in untreated mice (B). Uptake was reduced in H460 tumors, consistent with whole body PET data of ^{18}F-FMAU uptake following cisplatin. Measured activity in bulk resected tissues from treated mice bearing H460 or H292 tumors was normalized to untreated controls. Relative activity suggests that cisplatin treatment does not significantly alter systemic biodistribution of ^{18}F-FMAU. As seen in PET, H460 tumors showed a significant reduction in ^{18}F-FMAU retention after cisplatin treatment compared to controls (*p=0.17). While ^{18}F-FMAU in the blood pool increased after cisplatin treatment, these effects were not determined to be statistically significant in mice bearing either H460 or H292 tumors (p=0.52 and 0.53, respectively)

3.4. ^{18}F-FMAU metabolism was not altered by cisplatin treatment

Following euthanasia, serum of whole blood samples from representative animals in each treatment group was analyzed with HPLC. Fractions were measured with gamma scintigraphy to detect ^{18}F-FMAU and any relevant metabolites, as represented by peaks in corresponding fractions. Samples were compared to HPLC curves of pure ^{18}F-FMAU samples retained prior to animal injections (Figure 19A). The majority of activity detected in the serum corresponded to unmetabolized ^{18}F-FMAU, with small amounts of metabolite noted as separate peak(s). Comparison of serum from mice treated with cisplatin (Figure 19C) to serum from untreated mice (Figure 19B) suggests that a single injection of cisplatin does not cause any measurable change in ^{18}F-FMAU metabolism. Thus, changes in ^{18}F activity in tumors is unlikely to be caused by uptake of functionally different metabolites which retain ^{18}F conjugation.

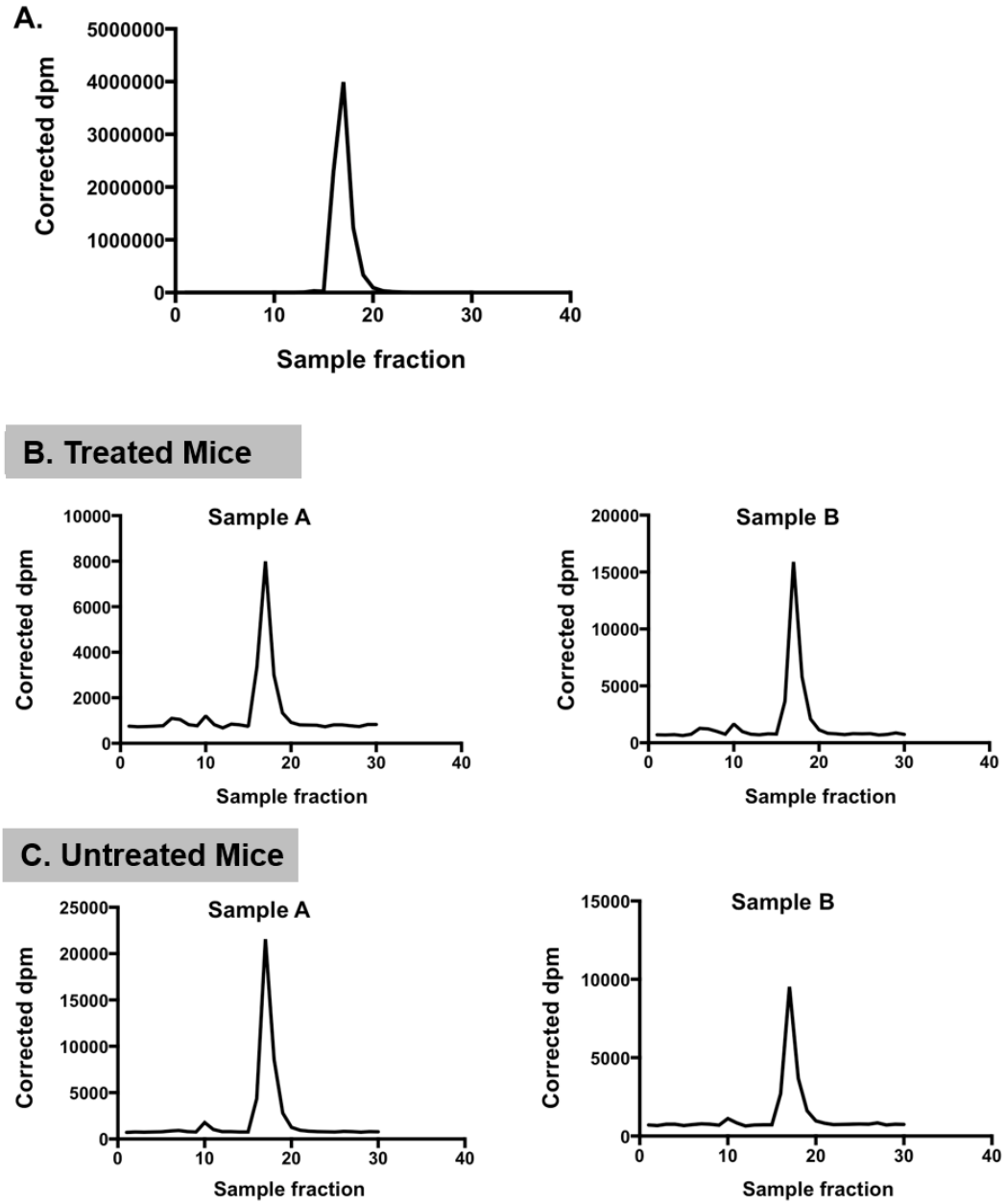

Figure 19. ^{18}F-FMAU metabolites represent a negligible fraction of ^{18}F-FMAU detected in the blood and are not significantly altered by cisplatin treatment. HPLC analysis of serum from cisplatin-treated and control mice was performed after sacrifice following the second PET scan. Peaks of activity in resulting fractions were detected with gamma-scintigraphy, and were compared to curves generated from HPLC of a sample of synthesized ^{18}F-FMAU (A). Although trace amounts of metabolites are seen in serum, the majority of activity corresponds with ^{18}F-FMAU in treated (B) and untreated mice (C).

4. Discussion

As a functional analogue of thymidine like ^{18}F-FLT, ^{18}F-FMAU was originally tested as a marker for proliferation in tumor imaging (181, 182, 195). However, FMAU phosphorylation has been shown to be primarily phosphorylated by TK2. Unlike TK1, TK2 activity is not cell-cycle dependent, and is closely associated with mitochondrial DNA synthesis. While this understanding confounds the association between ^{18}F-FMAU retention and cellular proliferation, it provides new opportunities for the use of ^{18}F-FMAU PET.

In this work, we present evidence that ^{18}F-FMAU PET may be useful in identifying early response to chemotherapy in non-small cell lung tumors. Previous work in our lab had demonstrated that mild cellular stress, such as nutritional deprivation, could induce a transient increase in FMAU uptake and retention in multiple cancer cell lines (102). These cells demonstrated increased TK2 activity and FMAU retention, while TK1 activity and FLT retention dropped. This suggested that, while proliferation (and associated FLT phosphorylation) slowed during cellular stress, a “flare” effect may be observed in FMAU retention which could indicate a stress response. Unlike nutritional or oxidative pressures, cisplatin treatment induces a very strong genotoxic effect. Interestingly, in vitro uptake assays of ^{18}F-FMAU showed a flare in uptake following cisplatin treatment in cisplatin-resistant H292 cells (Fig. 2B). This effect was not seen in cisplatin-sensitive H460 cells. Although unexpected, increased FMAU retention in H292 cells could be indicative of a cellular stress response—one which is perhaps more robust in overcoming the effects of cisplatin.

This “flare” effect was not seen in mouse studies of ^{18}F-FMAU PET which utilized the same tumor cell lines (Fig.3). However, an extremely significant drop in ^{18}F-FMAU retention was measured in H460 tumors treated with cisplatin compared to controls, while no difference was seen with cisplatin treatment in H292 tumors. The reduced uptake in the H460 tumors, which were more likely to respond to cisplatin treatment the H292 tumors, occurred within 24 hours of a single injection of cisplatin. This was well before any measurable changes in tumor size were evident, indicating that ^{18}F-FMAU PET was sensitive enough to measure very early changes in H460 metabolism induced by cisplatin.

It is important to note that, while a flare was seen in H292 cells in vitro, this effect was measured with a relatively high dose of cisplatin (IC_{50} value as determined by MTT). In vivo, the therapeutic dose is limited by systemic bioavailability and toxicity. Thus, the cisplatin dose to which the H292 tumors were exposed in mice may not have been powerful enough to alter tumor cell metabolism and ^{18}F-FMAU retention. Realistically, chemotherapeutic doses in the clinic often fall short of the amount of drug required to kill tumors.

To better understand these data, we will perform protein analyses of both cell lines to measure TK2 presence in the presence or absence of cisplatin. This should ensure that TK2 protein levels are not affected by cisplatin in a way which could confound the imaging data. Further, we may pursue measurements of mitochondrial mass in each cell line before and after cisplatin treatment, to ascertain the role of mitochondrial proliferation in FMAU uptake in these cells. This could provide insight into the differences seen in FMAU uptake following cisplatin

treatment of these cells, as well as the inconsistencies observed between cell studies and animal PET studies.

While we did not measure a flare with ^{18}F-FMAU uptake in either tumor in response to cisplatin, ^{18}F-FMAU PET was able to differentiate between cisplatin-sensitive and cisplatin-resistant tumors. Moreover, the sensitive tumors were distinguishable 24 hours into treatment, after a single dose. We believe that this is compelling evidence for the use of ^{18}F-FMAU PET in predicting non-small cell lung cancer response early into cisplatin treatment. To better understand the potential of this tracer for oncological imaging, further study of ^{18}F-FMAU PET in tumors is necessary.

CHAPTER 4. SUMMARY

Cancer patients face a myriad of challenges in combating tumors, which are often as unique as the person harboring them. Oncological PET offers a variety of opportunities for researchers and clinicians to use non-invasive imaging in the personalization of cancer treatment. Although many forms of imaging can provide information on tumor location, size, and general morphology, PET can measure metabolic and biochemical parameters of tumors. Due to the impressive sensitivity of PET, thoughtfully designed tracers can be used to quantify specific processes in tissues. In the case of PET for tumors, information about metabolic activity or cellular behavior can define or drastically alter therapeutic strategies selected to treat a cancer.

Information about tumor biochemistry is assessed non-invasively with PET imaging. Unlike more traditional means of tumor profiling, such as tissue biopsy, PET does not require invasive procedures and provides information about the entire tumor or multiple tumor within an individual. This makes longitudinal monitoring of tumor behavior much easier on the patient, and can be used to measure changes in tumor activity over time or as a result of therapy. Subtle changes in tumor behavior can be detected with PET well before changes in overall morphology are measurable, making PET an ideal means of detecting early response to treatment. The heterogeneic nature of tumors leads to a wide variety of responses to conventional or experimental therapies. Early detection of response in patient populations could identify patients who are likely to respond to a therapy and, more importantly, those who are unlikely to respond. Patients with

tumors predicted to be resistant can move on to other strategies before there is obvious growth or spread of the tumor and thus avoid further ineffective treatment regimen.

PET has become an important method for measuring and monitoring nanoparticle delivery to solid tumors, particularly in preclinical studies. Successful delivery of nanoparticles to solid tumor tissue is necessary for the successful implementation of nanoparticle-based cancer treatments. Unfortunately, nanoparticle delivery is highly variable in patient tumors, which has led to an effort in identifying therapeutic strategies for manipulating nanoparticle delivery as needed. We have shown that PET with radiolabeled nanoparticles is an elegant means to not only measure nanoparticle delivery to tumors, but to monitor changes induced by combination therapy. We found that bevacizumab-induced changes in vascularity of colon tumor xenografts was able to significantly alter nanoparticle delivery after only one week of treatment. Further, these effects were detectable by PET with a ^{64}Cu-labeled liposome. By utilizing tracer nanoparticles that mimic drug-loaded nanoparticles, researchers can utilize PET to define and monitor therapeutic strategies to augment nanoparticle delivery to solid tumors.

The biochemistry of the tracers used for PET define the type of information that is acquired with a PET scan. In the clinic, the most commonly used tracers are small molecules which specifically integrate into biological processes of interest. Similarly, ^{18}F-FMAU is a thymidine analogue studied for tumor imaging with PET. In our studies of both cells and mouse models of lung cancer, we found that changes ^{18}F-FMAU uptake may be indicative of tumor response to treatment

with cisplatin. ^{18}F-FMAU uptake in cisplatin-responsive tumors dropped dramatically during treatment, while resistant tumors showed little change in tracer uptake. Importantly, these changes were seen within 24 hours of treatment initiation, and only one injection of cisplatin. ^{18}F-FMAU PET was able to clearly differentiate between resistant and sensitive tumors very early into treatment. This supports the promise of PET for imaging early response to treatment in lung tumors undergoing chemotherapy.

In conclusion, the advantages of oncological PET imaging extend far beyond the limits of defining tumor morphology. PET can be utilized to detect treatment-induced changes in tumor behavior with tracers that range from small-small molecule to nanoparticles. In the era of targeted therapies and precision medicine, PET is a powerful tool to measure, monitor, and predict tumor response to treatment. In this way, PET can help physicians select better therapeutic strategies that are tailored to the specific needs of each individual patient.

REFERENCES

1. Peng BH, Levin CS. Recent development in PET instrumentation. Curr Pharm Biotechnol. 2010;11(6):555-71. PubMed PMID: 20497121; PubMed Central PMCID: PMCPMC3697478.

2. Cherry SR. Fundamentals of positron emission tomography and applications in preclinical drug development. J Clin Pharmacol. 2001;41(5):482-91. PubMed PMID: 11361044.

3. Pichler BJ, Wehrl HF, Judenhofer MS. Latest advances in molecular imaging instrumentation. J Nucl Med. 2008;49 Suppl 2:5S-23S. doi: 10.2967/jnumed.108.045880. PubMed PMID: 18523063.

4. Levin CS, Hoffman EJ. Calculation of positron range and its effect on the fundamental limit of positron emission tomography system spatial resolution. Phys Med Biol. 1999;44(3):781-99. PubMed PMID: 10211810.

5. Riemann B, Schafers KP, Schober O, Schafers M. Small animal PET in preclinical studies: opportunities and challenges. Q J Nucl Med Mol Imaging. 2008;52(3):215-21. PubMed PMID: 18551093.

6. Weber S, Bauer A. Small animal PET: aspects of performance assessment. Eur J Nucl Med Mol Imaging. 2004;31(11):1545-55. doi: 10.1007/s00259-004-1683-x. PubMed PMID: 15517252.

7. Kim JS, Lee JS, Im KC, Kim SJ, Kim SY, Lee DS, et al. Performance measurement of the microPET focus 120 scanner. J Nucl Med. 2007;48(9):1527-35. doi: 10.2967/jnumed.107.040550. PubMed PMID: 17704248.

8. Schafers KP, Reader AJ, Kriens M, Knoess C, Schober O, Schafers M. Performance evaluation of the 32-module quadHIDAC small-animal PET scanner. J Nucl Med. 2005;46(6):996-1004. PubMed PMID: 15937311.

9. Wang Y, Seidel J, Tsui BM, Vaquero JJ, Pomper MG. Performance evaluation of the GE healthcare eXplore VISTA dual-ring small-animal PET scanner. J Nucl Med. 2006;47(11):1891-900. PubMed PMID: 17079824.

10. Hwang BH, Kim MH, Chang K. Molecular imaging of high-risk atherosclerotic plaques: is it clinically translatable? Korean Circ J. 2011;41(9):497-502. doi: 10.4070/kcj.2011.41.9.497. PubMed PMID: 22022323; PubMed Central PMCID: PMCPMC3193039.

11. Clark PM, Ebiana VA, Gosa L, Cloughesy TF, Nathanson DA. Harnessing Preclinical Molecular Imaging to Inform Advances in Personalized Cancer Medicine. J Nucl Med. 2017;58(5):689-96. doi: 10.2967/jnumed.116.181693. PubMed PMID: 28385796.

12. Diksic M, Jolly D. New high-yield synthesis of 18F-labelled 2-deoxy-2-fluoro-D-glucose. Int J Appl Radiat Isot. 1983;34(6):893-6. PubMed PMID: 6874115.

13. Brown RS, Leung JY, Fisher SJ, Frey KA, Ethier SP, Wahl RL. Intratumoral distribution of tritiated-FDG in breast carcinoma: correlation between Glut-1 expression and FDG uptake. J Nucl Med. 1996;37(6):1042-7. PubMed PMID: 8683298.

14. Buerkle A, Weber WA. Imaging of tumor glucose utilization with positron emission tomography. Cancer Metastasis Rev. 2008;27(4):545-54. doi: 10.1007/s10555-008-9151-x. PubMed PMID: 18523732.

15. Shields AF, Grierson JR, Dohmen BM, Machulla HJ, Stayanoff JC, Lawhorn-Crews JM, et al. Imaging proliferation in vivo with [F-18]FLT and positron emission tomography. Nat Med. 1998;4(11):1334-6. doi: 10.1038/3337. PubMed PMID: 9809561.

16. Grierson JR, Shields AF. Radiosynthesis of 3'-deoxy-3'-[(18)F]fluorothymidine: [(18)F]FLT for imaging of cellular proliferation in vivo. Nucl Med Biol. 2000;27(2):143-56. PubMed PMID: 10773543.

17. Roy Chowdhury M, Schumann C, Bhakta-Guha D, Guha G. Cancer nanotheranostics: Strategies, promises and impediments. Biomed Pharmacother. 2016;84:291-304. doi: 10.1016/j.biopha.2016.09.035. PubMed PMID: 27665475.

18. Chakravarty R, Goel S, Dash A, Cai W. Radiolabeled inorganic nanoparticles for positron emission tomography imaging of cancer: an overview. Q J Nucl Med Mol Imaging. 2017;61(2):181-204. doi: 10.23736/S1824-4785.17.02969-7. PubMed PMID: 28124549; PubMed Central PMCID: PMCPMC5477426.

19. Phelps ME. Positron emission tomography provides molecular imaging of biological processes. Proc Natl Acad Sci U S A. 2000;97(16):9226-33. PubMed PMID: 10922074; PubMed Central PMCID: PMCPMC16850.

20. Fledelius J, Khalil AA, Hjorthaug K, Frokiaer J. Using positron emission tomography (PET) response criteria in solid tumours (PERCIST) 1.0 for

evaluation of 2'-deoxy-2'-[18F] fluoro-D-glucose-PET/CT scans to predict survival early during treatment of locally advanced non-small cell lung cancer (NSCLC). J Med Imaging Radiat Oncol. 2016;60(2):231-8. doi: 10.1111/1754-9485.12427. PubMed PMID: 26678718.

21. Hendlisz A, Deleporte A, Delaunoit T, Marechal R, Peeters M, Holbrechts S, et al. The Prognostic Significance of Metabolic Response Heterogeneity in Metastatic Colorectal Cancer. PLoS One. 2015;10(9):e0138341. doi: 10.1371/journal.pone.0138341. PubMed PMID: 26421426; PubMed Central PMCID: PMCPMC4589397.

22. Shang J, Ling X, Zhang L, Tang Y, Xiao Z, Cheng Y, et al. Comparison of RECIST, EORTC criteria and PERCIST for evaluation of early response to chemotherapy in patients with non-small-cell lung cancer. Eur J Nucl Med Mol Imaging. 2016;43(11):1945-53. doi: 10.1007/s00259-016-3420-7. PubMed PMID: 27236466.

23. Hwang SH, Cho A, Yun M, Choi YD, Rha SY, Kang WJ. Prognostic Value of Pretreatment Metabolic Tumor Volume and Total Lesion Glycolysis Using 18F-FDG PET/CT in Patients With Metastatic Renal Cell Carcinoma Treated With Anti-Vascular Endothelial Growth Factor-Targeted Agents. Clin Nucl Med. 2017;42(5):e235-e41. doi: 10.1097/RLU.0000000000001612. PubMed PMID: 28288043.

24. Hwang SH, Lee JW, Cho HJ, Kim KS, Choi GH, Yun M. Prognostic Value of Metabolic Tumor Volume and Total Lesion Glycolysis on Preoperative 18F-FDG PET/CT in Patients With Very Early and Early Hepatocellular Carcinoma.

Clin Nucl Med. 2017;42(1):34-9. doi: 10.1097/RLU.0000000000001449. PubMed PMID: 27775949.

25. Horn KP, Yap JT, Agarwal N, Morton KA, Kadrmas DJ, Beardmore B, et al. FDG and FLT-PET for Early measurement of response to 37.5 mg daily sunitinib therapy in metastatic renal cell carcinoma. Cancer Imaging. 2015;15:15. doi: 10.1186/s40644-015-0049-x. PubMed PMID: 26335224; PubMed Central PMCID: PMCPMC4558962.

26. Challapalli A, Barwick T, Pearson RA, Merchant S, Mauri F, Howell EC, et al. 3'-Deoxy-3'-(1)(8)F-fluorothymidine positron emission tomography as an early predictor of disease progression in patients with advanced and metastatic pancreatic cancer. Eur J Nucl Med Mol Imaging. 2015;42(6):831-40. doi: 10.1007/s00259-015-3000-2. PubMed PMID: 25673055.

27. Siva S, Callahan J, Pryor D, Martin J, Lawrentschuk N, Hofman MS. Utility of 68 Ga prostate specific membrane antigen - positron emission tomography in diagnosis and response assessment of recurrent renal cell carcinoma. J Med Imaging Radiat Oncol. 2017;61(3):372-8. doi: 10.1111/1754-9485.12590. PubMed PMID: 28116853.

28. Davis JC, Daw NC, Navid F, Billups CA, Wu J, Bahrami A, et al. FDG Uptake During Early Adjuvant Chemotherapy Predicts Histologic Response in Pediatric and Young Adult Patients with Osteosarcoma. J Nucl Med. 2017. doi: 10.2967/jnumed.117.190595. PubMed PMID: 28611244.

29. Fang B, Mehran RJ, Heymach JV, Swisher SG. Predictive biomarkers in precision medicine and drug development against lung cancer. Chin J Cancer.

2015;34(7):295-309. doi: 10.1186/s40880-015-0028-4. PubMed PMID: 26134262; PubMed Central PMCID: PMCPMC4593363.

30. Ciccarese C, Massari F, Iacovelli R, Fiorentino M, Montironi R, Di Nunno V, et al. Prostate cancer heterogeneity: Discovering novel molecular targets for therapy. Cancer Treat Rev. 2017;54:68-73. doi: 10.1016/j.ctrv.2017.02.001. PubMed PMID: 28231559.

31. Caparello C, Meijer LL, Garajova I, Falcone A, Le Large TY, Funel N, et al. FOLFIRINOX and translational studies: Towards personalized therapy in pancreatic cancer. World J Gastroenterol. 2016;22(31):6987-7005. doi: 10.3748/wjg.v22.i31.6987. PubMed PMID: 27610011; PubMed Central PMCID: PMCPMC4988311.

32. Wahl RL, Zasadny K, Helvie M, Hutchins GD, Weber B, Cody R. Metabolic monitoring of breast cancer chemohormonotherapy using positron emission tomography: initial evaluation. J Clin Oncol. 1993;11(11):2101-11. doi: 10.1200/JCO.1993.11.11.2101. PubMed PMID: 8229124.

33. Buvat I, Necib H, Garcia C, Wagner A, Vanderlinden B, Emonts P, et al. Lesion-based detection of early chemosensitivity using serial static FDG PET/CT in metastatic colorectal cancer. Eur J Nucl Med Mol Imaging. 2012;39(10):1628-34. doi: 10.1007/s00259-012-2172-2. PubMed PMID: 22710958; PubMed Central PMCID: PMCPMC3458195.

34. Segreto S, Fonti R, Ottaviano M, Pellegrino S, Pace L, Damiano V, et al. Evaluation of metabolic response with 18F-FDG PET-CT in patients with advanced or recurrent thymic epithelial tumors. Cancer Imaging. 2017;17(1):10.

doi: 10.1186/s40644-017-0112-x. PubMed PMID: 28264726; PubMed Central PMCID: PMCPMC5339950.

35. Cremonesi M, Gilardi L, Ferrari ME, Piperno G, Travaini LL, Timmerman R, et al. Role of interim 18F-FDG-PET/CT for the early prediction of clinical outcomes of Non-Small Cell Lung Cancer (NSCLC) during radiotherapy or chemo-radiotherapy. A systematic review. Eur J Nucl Med Mol Imaging. 2017. doi: 10.1007/s00259-017-3762-9. PubMed PMID: 28681192.

36. Wong ANM, McArthur GA, Hofman MS, Hicks RJ. The Advantages and Challenges of Using FDG PET/CT for Response Assessment in Melanoma in the Era of Targeted Agents and Immunotherapy. Eur J Nucl Med Mol Imaging. 2017;44(Suppl 1):67-77. doi: 10.1007/s00259-017-3691-7. PubMed PMID: 28389693.

37. Chang JC, Kundranda M. Novel Diagnostic and Predictive Biomarkers in Pancreatic Adenocarcinoma. Int J Mol Sci. 2017;18(3). doi: 10.3390/ijms18030667. PubMed PMID: 28335509; PubMed Central PMCID: PMCPMC5372679.

38. Ulaner GA, Hyman DM, Ross DS, Corben A, Chandarlapaty S, Goldfarb S, et al. Detection of HER2-Positive Metastases in Patients with HER2-Negative Primary Breast Cancer Using 89Zr-Trastuzumab PET/CT. J Nucl Med. 2016;57(10):1523-8. doi: 10.2967/jnumed.115.172031. PubMed PMID: 27151988; PubMed Central PMCID: PMCPMC5050126.

39. Afshar-Oromieh A, Holland-Letz T, Giesel FL, Kratochwil C, Mier W, Haufe S, et al. Diagnostic performance of 68Ga-PSMA-11 (HBED-CC) PET/CT

in patients with recurrent prostate cancer: evaluation in 1007 patients. Eur J Nucl Med Mol Imaging. 2017;44(8):1258-68. doi: 10.1007/s00259-017-3711-7. PubMed PMID: 28497198; PubMed Central PMCID: PMCPMC5486817.

40. Efferson CL, Winkelmann CT, Ware C, Sullivan T, Giampaoli S, Tammam J, et al. Downregulation of Notch pathway by a gamma-secretase inhibitor attenuates AKT/mammalian target of rapamycin signaling and glucose uptake in an ERBB2 transgenic breast cancer model. Cancer Res. 2010;70(6):2476-84. doi: 10.1158/0008-5472.CAN-09-3114. PubMed PMID: 20197467.

41. Kaliszczak M, Trousil S, Aberg O, Perumal M, Nguyen QD, Aboagye EO. A novel small molecule hydroxamate preferentially inhibits HDAC6 activity and tumour growth. Br J Cancer. 2013;108(2):342-50. doi: 10.1038/bjc.2012.576. PubMed PMID: 23322205; PubMed Central PMCID: PMCPMC3566806.

42. Sagnella SM, McCarroll JA, Kavallaris M. Drug delivery: beyond active tumour targeting. Nanomedicine. 2014;10(6):1131-7. doi: 10.1016/j.nano.2014.04.012. PubMed PMID: 24823644.

43. Jain RK, Stylianopoulos T. Delivering nanomedicine to solid tumors. Nat Rev Clin Oncol. 2010;7(11):653-64. doi: 10.1038/nrclinonc.2010.139. PubMed PMID: 20838415; PubMed Central PMCID: PMCPMC3065247.

44. Richardson VJ, Ryman BE, Jewkes RF, Jeyasingh K, Tattersall MN, Newlands ES, et al. Tissue distribution and tumour localization of 99m-technetium-labelled liposomes in cancer patients. Br J Cancer. 1979;40(1):35-43. PubMed PMID: 475960; PubMed Central PMCID: PMCPMC2009957.

45. Prabhakar U, Maeda H, Jain RK, Sevick-Muraca EM, Zamboni W, Farokhzad OC, et al. Challenges and key considerations of the enhanced permeability and retention effect for nanomedicine drug delivery in oncology. Cancer Res. 2013;73(8):2412-7. doi: 10.1158/0008-5472.CAN-12-4561. PubMed PMID: 23423979; PubMed Central PMCID: PMCPMC3916009.

46. Mura S, Couvreur P. Nanotheranostics for personalized medicine. Adv Drug Deliv Rev. 2012;64(13):1394-416. doi: 10.1016/j.addr.2012.06.006. PubMed PMID: 22728642.

47. Lammers T, Aime S, Hennink WE, Storm G, Kiessling F. Theranostic nanomedicine. Acc Chem Res. 2011;44(10):1029-38. doi: 10.1021/ar200019c. PubMed PMID: 21545096.

48. Zhou H, Qian W, Uckun FM, Wang L, Wang YA, Chen H, et al. IGF1 Receptor Targeted Theranostic Nanoparticles for Targeted and Image-Guided Therapy of Pancreatic Cancer. ACS Nano. 2015;9(8):7976-91. doi: 10.1021/acsnano.5b01288. PubMed PMID: 26242412; PubMed Central PMCID: PMCPMC4908958.

49. Melancon MP, Zhou M, Li C. Cancer theranostics with near-infrared light-activatable multimodal nanoparticles. Acc Chem Res. 2011;44(10):947-56. doi: 10.1021/ar200022e. PubMed PMID: 21848277; PubMed Central PMCID: PMCPMC3196765.

50. Minowa T, Kawano K, Kuribayashi H, Shiraishi K, Sugino T, Hattori Y, et al. Increase in tumour permeability following TGF-beta type I receptor-inhibitor treatment observed by dynamic contrast-enhanced MRI. Br J Cancer.

2009;101(11):1884-90. doi: 10.1038/sj.bjc.6605367. PubMed PMID: 19888220; PubMed Central PMCID: PMCPMC2788254.

51. Geretti E, Leonard SC, Dumont N, Lee H, Zheng J, De Souza R, et al. Cyclophosphamide-Mediated Tumor Priming for Enhanced Delivery and Antitumor Activity of HER2-Targeted Liposomal Doxorubicin (MM-302). Mol Cancer Ther. 2015;14(9):2060-71. doi: 10.1158/1535-7163.MCT-15-0314. PubMed PMID: 26162690.

52. Doi Y, Abu Lila AS, Matsumoto H, Okada T, Shimizu T, Ishida T. Improvement of intratumor microdistribution of PEGylated liposome via tumor priming by metronomic S-1 dosing. Int J Nanomedicine. 2016;11:5573-82. doi: 10.2147/IJN.S119069. PubMed PMID: 27822036; PubMed Central PMCID: PMCPMC5087787.

53. Nakamura K, Abu Lila AS, Matsunaga M, Doi Y, Ishida T, Kiwada H. A double-modulation strategy in cancer treatment with a chemotherapeutic agent and siRNA. Mol Ther. 2011;19(11):2040-7. doi: 10.1038/mt.2011.174. PubMed PMID: 21878904; PubMed Central PMCID: PMCPMC3222530.

54. Moding EJ, Clark DP, Qi Y, Li Y, Ma Y, Ghaghada K, et al. Dual-energy micro-computed tomography imaging of radiation-induced vascular changes in primary mouse sarcomas. Int J Radiat Oncol Biol Phys. 2013;85(5):1353-9. doi: 10.1016/j.ijrobp.2012.09.027. PubMed PMID: 23122984; PubMed Central PMCID: PMCPMC3625949.

55. Matteucci ML, Anyarambhatla G, Rosner G, Azuma C, Fisher PE, Dewhirst MW, et al. Hyperthermia increases accumulation of technetium-99m-

labeled liposomes in feline sarcomas. Clin Cancer Res. 2000;6(9):3748-55. PubMed PMID: 10999769.

56. Kleiter MM, Yu D, Mohammadian LA, Niehaus N, Spasojevic I, Sanders L, et al. A tracer dose of technetium-99m-labeled liposomes can estimate the effect of hyperthermia on intratumoral doxil extravasation. Clin Cancer Res. 2006;12(22):6800-7. doi: 10.1158/1078-0432.CCR-06-0839. PubMed PMID: 17121901.

57. Head HW, Dodd GD, 3rd, Bao A, Soundararajan A, Garcia-Rojas X, Prihoda TJ, et al. Combination radiofrequency ablation and intravenous radiolabeled liposomal Doxorubicin: imaging and quantification of increased drug delivery to tumors. Radiology. 2010;255(2):405-14. doi: 10.1148/radiol.10090714. PubMed PMID: 20413753; PubMed Central PMCID: PMCPMC2858812.

58. Zheng X, Goins BA, Cameron IL, Santoyo C, Bao A, Frohlich VC, et al. Ultrasound-guided intratumoral administration of collagenase-2 improved liposome drug accumulation in solid tumor xenografts. Cancer Chemother Pharmacol. 2011;67(1):173-82. doi: 10.1007/s00280-010-1305-1. PubMed PMID: 20306263.

59. Lammers T, Subr V, Peschke P, Kuhnlein R, Hennink WE, Ulbrich K, et al. Image-guided and passively tumour-targeted polymeric nanomedicines for radiochemotherapy. Br J Cancer. 2008;99(6):900-10. doi: 10.1038/sj.bjc.6604561. PubMed PMID: 19238631; PubMed Central PMCID: PMCPMC2538765.

60. Kobayashi H, Reijnders K, English S, Yordanov AT, Milenic DE, Sowers AL, et al. Application of a macromolecular contrast agent for detection of alterations of tumor vessel permeability induced by radiation. Clin Cancer Res. 2004;10(22):7712-20. doi: 10.1158/1078-0432.CCR-04-1175. PubMed PMID: 15570005.

61. Daldrup-Link HE, Mohanty S, Ansari C, Lenkov O, Shaw A, Ito K, et al. Alk5 inhibition increases delivery of macromolecular and protein-bound contrast agents to tumors. JCI Insight. 2016;1(6). doi: 10.1172/jci.insight.85608. PubMed PMID: 27182558; PubMed Central PMCID: PMCPMC4864003.

62. Kumar V, Boucher Y, Liu H, Ferreira D, Hooker J, Catana C, et al. Noninvasive Assessment of Losartan-Induced Increase in Functional Microvasculature and Drug Delivery in Pancreatic Ductal Adenocarcinoma. Transl Oncol. 2016;9(5):431-7. doi: 10.1016/j.tranon.2016.07.004. PubMed PMID: 27751347; PubMed Central PMCID: PMCPMC5067928.

63. Appelbe OK, Zhang Q, Pelizzari CA, Weichselbaum RR, Kron SJ. Image-Guided Radiotherapy Targets Macromolecules through Altering the Tumor Microenvironment. Mol Pharm. 2016;13(10):3457-67. doi: 10.1021/acs.molpharmaceut.6b00465. PubMed PMID: 27560921; PubMed Central PMCID: PMCPMC5103304.

64. Wilmes LJ, Pallavicini MG, Fleming LM, Gibbs J, Wang D, Li KL, et al. AG-013736, a novel inhibitor of VEGF receptor tyrosine kinases, inhibits breast cancer growth and decreases vascular permeability as detected by dynamic

contrast-enhanced magnetic resonance imaging. Magn Reson Imaging. 2007;25(3):319-27. doi: 10.1016/j.mri.2006.09.041. PubMed PMID: 17371720.

65. Chapman S, Dobrovolskaia M, Farahani K, Goodwin A, Joshi A, Lee H, et al. Nanoparticles for cancer imaging: The good, the bad, and the promise. Nano Today. 2013;8(5):454-60. doi: 10.1016/j.nantod.2013.06.001. PubMed PMID: 25419228; PubMed Central PMCID: PMCPMC4240321.

66. Matsumura Y, Maeda H. A new concept for macromolecular therapeutics in cancer chemotherapy: mechanism of tumoritropic accumulation of proteins and the antitumor agent smancs. Cancer Res. 1986;46(12 Pt 1):6387-92. PubMed PMID: 2946403.

67. Torchilin V. Tumor delivery of macromolecular drugs based on the EPR effect. Adv Drug Deliv Rev. 2011;63(3):131-5. doi: 10.1016/j.addr.2010.03.011. PubMed PMID: 20304019.

68. Pirollo KF, Chang EH. Does a targeting ligand influence nanoparticle tumor localization or uptake? Trends Biotechnol. 2008;26(10):552-8. doi: 10.1016/j.tibtech.2008.06.007. PubMed PMID: 18722682.

69. Danhier F. To exploit the tumor microenvironment: Since the EPR effect fails in the clinic, what is the future of nanomedicine? J Control Release. 2016;244(Pt A):108-21. doi: 10.1016/j.jconrel.2016.11.015. PubMed PMID: 27871992.

70. Miao L, Huang L. Exploring the tumor microenvironment with nanoparticles. Cancer Treat Res. 2015;166:193-226. doi: 10.1007/978-3-319-

16555-4_9. PubMed PMID: 25895870; PubMed Central PMCID: PMCPMC5010228.

71. Casazza A, Di Conza G, Wenes M, Finisguerra V, Deschoemaeker S, Mazzone M. Tumor stroma: a complexity dictated by the hypoxic tumor microenvironment. Oncogene. 2014;33(14):1743-54. doi: 10.1038/onc.2013.121. PubMed PMID: 23604130.

72. Glentis A, Gurchenkov V, Matic Vignjevic D. Assembly, heterogeneity, and breaching of the basement membranes. Cell Adh Migr. 2014;8(3):236-45. PubMed PMID: 24727304; PubMed Central PMCID: PMCPMC4198347.

73. Maeda H. Toward a full understanding of the EPR effect in primary and metastatic tumors as well as issues related to its heterogeneity. Adv Drug Deliv Rev. 2015;91:3-6. doi: 10.1016/j.addr.2015.01.002. PubMed PMID: 25579058.

74. Durymanov MO, Rosenkranz AA, Sobolev AS. Current Approaches for Improving Intratumoral Accumulation and Distribution of Nanomedicines. Theranostics. 2015;5(9):1007-20. doi: 10.7150/thno.11742. PubMed PMID: 26155316; PubMed Central PMCID: PMCPMC4493538.

75. Kjellman P, in 't Zandt R, Fredriksson S, Strand SE. Optimizing retention of multimodal imaging nanostructures in sentinel lymph nodes by nanoscale size tailoring. Nanomedicine. 2014;10(5):1089-95. doi: 10.1016/j.nano.2014.01.007. PubMed PMID: 24502988.

76. Song J, Yang X, Yang Z, Lin L, Liu Y, Zhou Z, et al. Rational Design of Branched Nanoporous Gold Nanoshells with Enhanced Physico-Optical

Properties for Optical Imaging and Cancer Therapy. ACS Nano. 2017. doi: 10.1021/acsnano.7b02048. PubMed PMID: 28605594.

77. Ramishetti S, Huang L. Intelligent design of multifunctional lipid-coated nanoparticle platforms for cancer therapy. Ther Deliv. 2012;3(12):1429-45. doi: 10.4155/tde.12.127. PubMed PMID: 23323560; PubMed Central PMCID: PMCPMC3584330.

78. Ojha T, Pathak V, Shi Y, Hennink WE, Moonen CTW, Storm G, et al. Pharmacological and physical vessel modulation strategies to improve EPR-mediated drug targeting to tumors. Adv Drug Deliv Rev. 2017. doi: 10.1016/j.addr.2017.07.007. PubMed PMID: 28697952.

79. Khawar IA, Kim JH, Kuh HJ. Improving drug delivery to solid tumors: priming the tumor microenvironment. J Control Release. 2015;201:78-89. doi: 10.1016/j.jconrel.2014.12.018. PubMed PMID: 25526702.

80. Ishida T, Kiwada H. Alteration of tumor microenvironment for improved delivery and intratumor distribution of nanocarriers. Biol Pharm Bull. 2013;36(5):692-7. PubMed PMID: 23649327.

81. Chung AS, Lee J, Ferrara N. Targeting the tumour vasculature: insights from physiological angiogenesis. Nat Rev Cancer. 2010;10(7):505-14. doi: 10.1038/nrc2868. PubMed PMID: 20574450.

82. Jain RK, Duda DG, Clark JW, Loeffler JS. Lessons from phase III clinical trials on anti-VEGF therapy for cancer. Nat Clin Pract Oncol. 2006;3(1):24-40. doi: 10.1038/ncponc0403. PubMed PMID: 16407877.

83. Miller K, Wang M, Gralow J, Dickler M, Cobleigh M, Perez EA, et al. Paclitaxel plus bevacizumab versus paclitaxel alone for metastatic breast cancer. N Engl J Med. 2007;357(26):2666-76. doi: 10.1056/NEJMoa072113. PubMed PMID: 18160686.

84. Reck M, von Pawel J, Zatloukal P, Ramlau R, Gorbounova V, Hirsh V, et al. Phase III trial of cisplatin plus gemcitabine with either placebo or bevacizumab as first-line therapy for nonsquamous non-small-cell lung cancer: AVAil. J Clin Oncol. 2009;27(8):1227-34. doi: 10.1200/JCO.2007.14.5466. PubMed PMID: 19188680.

85. Sandler A, Gray R, Perry MC, Brahmer J, Schiller JH, Dowlati A, et al. Paclitaxel-carboplatin alone or with bevacizumab for non-small-cell lung cancer. N Engl J Med. 2006;355(24):2542-50. doi: 10.1056/NEJMoa061884. PubMed PMID: 17167137.

86. Macarulla T, Sauri T, Tabernero J. Evaluation of aflibercept in the treatment of metastatic colorectal cancer. Expert Opin Biol Ther. 2014;14(10):1493-505. doi: 10.1517/14712598.2014.947956. PubMed PMID: 25152076.

87. Jain RK. Normalizing tumor vasculature with anti-angiogenic therapy: a new paradigm for combination therapy. Nat Med. 2001;7(9):987-9. doi: 10.1038/nm0901-987. PubMed PMID: 11533692.

88. Dickson PV, Hamner JB, Sims TL, Fraga CH, Ng CY, Rajasekeran S, et al. Bevacizumab-induced transient remodeling of the vasculature in neuroblastoma xenografts results in improved delivery and efficacy of

systemically administered chemotherapy. Clin Cancer Res. 2007;13(13):3942-50. doi: 10.1158/1078-0432.CCR-07-0278. PubMed PMID: 17606728.

89. Dreher MR, Liu W, Michelich CR, Dewhirst MW, Yuan F, Chilkoti A. Tumor vascular permeability, accumulation, and penetration of macromolecular drug carriers. J Natl Cancer Inst. 2006;98(5):335-44. doi: 10.1093/jnci/djj070. PubMed PMID: 16507830.

90. Lejeune FJ. Clinical use of TNF revisited: improving penetration of anti-cancer agents by increasing vascular permeability. J Clin Invest. 2002;110(4):433-5. doi: 10.1172/JCI16493. PubMed PMID: 12189235; PubMed Central PMCID: PMCPMC150423.

91. Sounni NE, Dehne K, van Kempen L, Egeblad M, Affara NI, Cuevas I, et al. Stromal regulation of vessel stability by MMP14 and TGFbeta. Dis Model Mech. 2010;3(5-6):317-32. doi: 10.1242/dmm.003863. PubMed PMID: 20223936; PubMed Central PMCID: PMCPMC2860851.

92. Smith TA. FDG uptake, tumour characteristics and response to therapy: a review. Nucl Med Commun. 1998;19(2):97-105. PubMed PMID: 9548192.

93. Young H, Baum R, Cremerius U, Herholz K, Hoekstra O, Lammertsma AA, et al. Measurement of clinical and subclinical tumour response using [18F]-fluorodeoxyglucose and positron emission tomography: review and 1999 EORTC recommendations. European Organization for Research and Treatment of Cancer (EORTC) PET Study Group. Eur J Cancer. 1999;35(13):1773-82. PubMed PMID: 10673991.

94. Husband JE. Monitoring tumour response. Eur Radiol. 1996;6(6):775-85. PubMed PMID: 8972311.

95. Kumar V, Nath K, Berman CG, Kim J, Tanvetyanon T, Chiappori AA, et al. Variance of SUVs for FDG-PET/CT is greater in clinical practice than under ideal study settings. Clin Nucl Med. 2013;38(3):175-82. doi: 10.1097/RLU.0b013e318279ffdf. PubMed PMID: 23354032; PubMed Central PMCID: PMCPMC3578161.

96. Potter M, Newport E, Morten KJ. The Warburg effect: 80 years on. Biochem Soc Trans. 2016;44(5):1499-505. doi: 10.1042/BST20160094. PubMed PMID: 27911732; PubMed Central PMCID: PMCPMC5095922.

97. Upadhyay M, Samal J, Kandpal M, Singh OV, Vivekanandan P. The Warburg effect: insights from the past decade. Pharmacol Ther. 2013;137(3):318-30. doi: 10.1016/j.pharmthera.2012.11.003. PubMed PMID: 23159371.

98. Shen B, Huang T, Sun Y, Jin Z, Li XF. Revisit 18F-fluorodeoxyglucose oncology positron emission tomography: "systems molecular imaging" of glucose metabolism. Oncotarget. 2017;8(26):43536-42. doi: 10.18632/oncotarget.16647. PubMed PMID: 28402949.

99. Clavo AC, Brown RS, Wahl RL. Fluorodeoxyglucose uptake in human cancer cell lines is increased by hypoxia. J Nucl Med. 1995;36(9):1625-32. PubMed PMID: 7658223.

100. Pauwels EK, Ribeiro MJ, Stoot JH, McCready VR, Bourguignon M, Maziere B. FDG accumulation and tumor biology. Nucl Med Biol. 1998;25(4):317-22. PubMed PMID: 9639291.

101. Hanahan D, Weinberg RA. Hallmarks of cancer: the next generation. Cell. 2011;144(5):646-74. doi: 10.1016/j.cell.2011.02.013. PubMed PMID: 21376230.

102. Tehrani OS, Douglas KA, Lawhorn-Crews JM, Shields AF. Tracking cellular stress with labeled FMAU reflects changes in mitochondrial TK2. Eur J Nucl Med Mol Imaging. 2008;35(8):1480-8. doi: 10.1007/s00259-008-0738-9. PubMed PMID: 18265975; PubMed Central PMCID: PMCPMC3826914.

103. Mangner TJ, Klecker RW, Anderson L, Shields AF. Synthesis of 2'-deoxy-2'-[18F]fluoro-beta-D-arabinofuranosyl nucleosides, [18F]FAU, [18F]FMAU, [18F]FBAU and [18F]FIAU, as potential PET agents for imaging cellular proliferation. Synthesis of [18F]labelled FAU, FMAU, FBAU, FIAU. Nucl Med Biol. 2003;30(3):215-24. PubMed PMID: 12745012.

104. Mankoff DA, Shields AF, Krohn KA. PET imaging of cellular proliferation. Radiol Clin North Am. 2005;43(1):153-67. PubMed PMID: 15693654.

105. Bading JR, Shields AF. Imaging of cell proliferation: status and prospects. J Nucl Med. 2008;49 Suppl 2:64S-80S. doi: 10.2967/jnumed.107.046391. PubMed PMID: 18523066.

106. Toyohara J, Waki A, Takamatsu S, Yonekura Y, Magata Y, Fujibayashi Y. Basis of FLT as a cell proliferation marker: comparative uptake studies with [3H]thymidine and [3H]arabinothymidine, and cell-analysis in 22 asynchronously

growing tumor cell lines. Nucl Med Biol. 2002;29(3):281-7. PubMed PMID: 11929696.

107. Reske SN, Deisenhofer S. Is 3'-deoxy-3'-(18)F-fluorothymidine a better marker for tumour response than (18)F-fluorodeoxyglucose? Eur J Nucl Med Mol Imaging. 2006;33 Suppl 1:38-43. doi: 10.1007/s00259-006-0134-2. PubMed PMID: 16721567.

108. Chalkidou A, Landau DB, Odell EW, Cornelius VR, O'Doherty MJ, Marsden PK. Correlation between Ki-67 immunohistochemistry and 18F-fluorothymidine uptake in patients with cancer: A systematic review and meta-analysis. Eur J Cancer. 2012;48(18):3499-513. doi: 10.1016/j.ejca.2012.05.001. PubMed PMID: 22658807.

109. Bading JR, Shahinian AH, Vail A, Bathija P, Koszalka GW, Koda RT, et al. Pharmacokinetics of the thymidine analog 2'-fluoro-5-methyl-1-beta-D-arabinofuranosyluracil (FMAU) in tumor-bearing rats. Nucl Med Biol. 2004;31(4):407-18. doi: 10.1016/j.nucmedbio.2004.01.001. PubMed PMID: 15093810.

110. Sun H, Sloan A, Mangner TJ, Vaishampayan U, Muzik O, Collins JM, et al. Imaging DNA synthesis with [18F]FMAU and positron emission tomography in patients with cancer. Eur J Nucl Med Mol Imaging. 2005;32(1):15-22. doi: 10.1007/s00259-004-1713-8. PubMed PMID: 15586282.

111. Shields AF, Briston DA, Chandupatla S, Douglas KA, Lawhorn-Crews J, Collins JM, et al. A simplified analysis of [18F]3'-deoxy-3'-fluorothymidine

metabolism and retention. Eur J Nucl Med Mol Imaging. 2005;32(11):1269-75. doi: 10.1007/s00259-005-1813-0. PubMed PMID: 15991018.

112. Muzi M, Vesselle H, Grierson JR, Mankoff DA, Schmidt RA, Peterson L, et al. Kinetic analysis of 3'-deoxy-3'-fluorothymidine PET studies: validation studies in patients with lung cancer. J Nucl Med. 2005;46(2):274-82. PubMed PMID: 15695787.

113. Wang J, Eriksson S. Phosphorylation of the anti-hepatitis B nucleoside analog 1-(2'-deoxy-2'-fluoro-1-beta-D-arabinofuranosyl)-5-iodouracil (FIAU) by human cytosolic and mitochondrial thymidine kinase and implications for cytotoxicity. Antimicrob Agents Chemother. 1996;40(6):1555-7. PubMed PMID: 8726039; PubMed Central PMCID: PMCPMC163369.

114. Graf N, Herrmann K, Numberger B, Zwisler D, Aichler M, Feuchtinger A, et al. [18F]FLT is superior to [18F]FDG for predicting early response to antiproliferative treatment in high-grade lymphoma in a dose-dependent manner. Eur J Nucl Med Mol Imaging. 2013;40(1):34-43. doi: 10.1007/s00259-012-2255-0. PubMed PMID: 23053327.

115. Ullrich RT, Zander T, Neumaier B, Koker M, Shimamura T, Waerzeggers Y, et al. Early detection of erlotinib treatment response in NSCLC by 3'-deoxy-3'-[F]-fluoro-L-thymidine ([F]FLT) positron emission tomography (PET). PLoS One. 2008;3(12):e3908. doi: 10.1371/journal.pone.0003908. PubMed PMID: 19079597; PubMed Central PMCID: PMCPMC2592703.

116. Chen H, Li Y, Wu H, Sun L, Lin Q, Zhao L, et al. 3'-deoxy-3'-[(1)(8)F]-fluorothymidine PET/CT in early determination of prognosis in patients with

esophageal squamous cell cancer: comparison with [(1)(8)F]-FDG PET/CT. Strahlenther Onkol. 2015;191(2):141-52. doi: 10.1007/s00066-014-0744-8. PubMed PMID: 25163419.

117. Bollineni VR, Kramer GM, Jansma EP, Liu Y, Oyen WJ. A systematic review on [(18)F]FLT-PET uptake as a measure of treatment response in cancer patients. Eur J Cancer. 2016;55:81-97. doi: 10.1016/j.ejca.2015.11.018. PubMed PMID: 26820682.

118. Ferlay J, Soerjomataram I, Dikshit R, Eser S, Mathers C, Rebelo M, et al. Cancer incidence and mortality worldwide: sources, methods and major patterns in GLOBOCAN 2012. Int J Cancer. 2015;136(5):E359-86. doi: 10.1002/ijc.29210. PubMed PMID: 25220842.

119. Ferlay J SI, Ervik M, Dikshit R, Eser S, Mathers C, Rebelo M, Parkin DM, Forman D, Bray, F. GLOBOCAN 2012 v1.0, Cancer Incidence and Mortality Worldwide: IARC CancerBase No. 11 [Internet]: Lyon, France: International Agency for Research on Cancer; 2013. Available from: http://globocan.iarc.fr, accessed on 05/08/2017.

120. Jass JR. Classification of colorectal cancer based on correlation of clinical, morphological and molecular features. Histopathology. 2007;50(1):113-30. doi: 10.1111/j.1365-2559.2006.02549.x. PubMed PMID: 17204026.

121. Marisa L, de Reynies A, Duval A, Selves J, Gaub MP, Vescovo L, et al. Gene expression classification of colon cancer into molecular subtypes: characterization, validation, and prognostic value. PLoS Med.

2013;10(5):e1001453. doi: 10.1371/journal.pmed.1001453. PubMed PMID: 23700391; PubMed Central PMCID: PMCPMC3660251.

122. Sinicrope FA, Okamoto K, Kasi PM, Kawakami H. Molecular Biomarkers in the Personalized Treatment of Colorectal Cancer. Clin Gastroenterol Hepatol. 2016;14(5):651-8. doi: 10.1016/j.cgh.2016.02.008. PubMed PMID: 26872400; PubMed Central PMCID: PMCPMC4836987.

123. De Rosa M, Rega D, Costabile V, Duraturo F, Niglio A, Izzo P, et al. The biological complexity of colorectal cancer: insights into biomarkers for early detection and personalized care. Therap Adv Gastroenterol. 2016;9(6):861-86. doi: 10.1177/1756283X16659790. PubMed PMID: 27803741; PubMed Central PMCID: PMCPMC5076770.

124. De Roock W, De Vriendt V, Normanno N, Ciardiello F, Tejpar S. KRAS, BRAF, PIK3CA, and PTEN mutations: implications for targeted therapies in metastatic colorectal cancer. Lancet Oncol. 2011;12(6):594-603. doi: 10.1016/S1470-2045(10)70209-6. PubMed PMID: 21163703.

125. Douillard JY, Rong A, Sidhu R. RAS mutations in colorectal cancer. N Engl J Med. 2013;369(22):2159-60. doi: 10.1056/NEJMc1312697. PubMed PMID: 24283232.

126. Hutchins G, Southward K, Handley K, Magill L, Beaumont C, Stahlschmidt J, et al. Value of mismatch repair, KRAS, and BRAF mutations in predicting recurrence and benefits from chemotherapy in colorectal cancer. J Clin Oncol. 2011;29(10):1261-70. doi: 10.1200/JCO.2010.30.1366. PubMed PMID: 21383284.

127. Mouradov D, Domingo E, Gibbs P, Jorissen RN, Li S, Soo PY, et al. Survival in stage II/III colorectal cancer is independently predicted by chromosomal and microsatellite instability, but not by specific driver mutations. Am J Gastroenterol. 2013;108(11):1785-93. doi: 10.1038/ajg.2013.292. PubMed PMID: 24042191.

128. Roth AD, Tejpar S, Delorenzi M, Yan P, Fiocca R, Klingbiel D, et al. Prognostic role of KRAS and BRAF in stage II and III resected colon cancer: results of the translational study on the PETACC-3, EORTC 40993, SAKK 60-00 trial. J Clin Oncol. 2010;28(3):466-74. doi: 10.1200/JCO.2009.23.3452. PubMed PMID: 20008640.

129. Cushman-Vokoun AM, Stover DG, Zhao Z, Koehler EA, Berlin JD, Vnencak-Jones CL. Clinical utility of KRAS and BRAF mutations in a cohort of patients with colorectal neoplasms submitted for microsatellite instability testing. Clin Colorectal Cancer. 2013;12(3):168-78. doi: 10.1016/j.clcc.2013.04.005. PubMed PMID: 23773459; PubMed Central PMCID: PMCPMC4090139.

130. Kotelevets L, Chastre E, Desmaele D, Couvreur P. Nanotechnologies for the treatment of colon cancer: From old drugs to new hope. Int J Pharm. 2016;514(1):24-40. doi: 10.1016/j.ijpharm.2016.06.005. PubMed PMID: 27863668.

131. Lee JK, Chan AT. Molecular Prognostic and Predictive Markers in Colorectal Cancer: Current Status. Curr Colorectal Cancer Rep. 2011;7(2):136-44. doi: 10.1007/s11888-011-0091-4. PubMed PMID: 21572547; PubMed Central PMCID: PMCPMC3093112.

132. Jemal A, Bray F, Center MM, Ferlay J, Ward E, Forman D. Global cancer statistics. CA Cancer J Clin. 2011;61(2):69-90. doi: 10.3322/caac.20107. PubMed PMID: 21296855.

133. Poon MA, O'Connell MJ, Moertel CG, Wieand HS, Cullinan SA, Everson LK, et al. Biochemical modulation of fluorouracil: evidence of significant improvement of survival and quality of life in patients with advanced colorectal carcinoma. J Clin Oncol. 1989;7(10):1407-18. doi: 10.1200/JCO.1989.7.10.1407. PubMed PMID: 2476530.

134. Brandi G, De Lorenzo S, Nannini M, Curti S, Ottone M, Dall'Olio FG, et al. Adjuvant chemotherapy for resected colorectal cancer metastases: Literature review and meta-analysis. World J Gastroenterol. 2016;22(2):519-33. doi: 10.3748/wjg.v22.i2.519. PubMed PMID: 26811604; PubMed Central PMCID: PMCPMC4716056.

135. Andre T, Louvet C, Maindrault-Goebel F, Couteau C, Mabro M, Lotz JP, et al. CPT-11 (irinotecan) addition to bimonthly, high-dose leucovorin and bolus and continuous-infusion 5-fluorouracil (FOLFIRI) for pretreated metastatic colorectal cancer. GERCOR. Eur J Cancer. 1999;35(9):1343-7. PubMed PMID: 10658525.

136. Ychou M, Rivoire M, Thezenas S, Quenet F, Delpero JR, Rebischung C, et al. A randomized phase II trial of three intensified chemotherapy regimens in first-line treatment of colorectal cancer patients with initially unresectable or not optimally resectable liver metastases. The METHEP trial. Ann Surg Oncol. 2013;20(13):4289-97. doi: 10.1245/s10434-013-3217-x. PubMed PMID: 23955585.

137. Souglakos J, Androulakis N, Syrigos K, Polyzos A, Ziras N, Athanasiadis A, et al. FOLFOXIRI (folinic acid, 5-fluorouracil, oxaliplatin and irinotecan) vs FOLFIRI (folinic acid, 5-fluorouracil and irinotecan) as first-line treatment in metastatic colorectal cancer (MCC): a multicentre randomised phase III trial from the Hellenic Oncology Research Group (HORG). Br J Cancer. 2006;94(6):798-805. doi: 10.1038/sj.bjc.6603011. PubMed PMID: 16508637; PubMed Central PMCID: PMCPMC2361370.

138. Twelves C. Can capecitabine replace 5-FU/leucovorin in combination with oxaliplatin for the treatment of advanced colorectal cancer? Oncology (Williston Park). 2002;16(12 Suppl No 14):23-6. PubMed PMID: 12520636.

139. Akiyama Y, Fujita K, Ishida H, Sunakawa Y, Yamashita K, Kawara K, et al. Association of ABCC2 genotype with efficacy of first-line FOLFIRI in Japanese patients with advanced colorectal cancer. Drug Metab Pharmacokinet. 2012;27(3):325-35. PubMed PMID: 22201120.

140. Giacchetti S, Perpoint B, Zidani R, Le Bail N, Faggiuolo R, Focan C, et al. Phase III multicenter randomized trial of oxaliplatin added to chronomodulated fluorouracil-leucovorin as first-line treatment of metastatic colorectal cancer. J Clin Oncol. 2000;18(1):136-47. doi: 10.1200/JCO.2000.18.1.136. PubMed PMID: 10623704.

141. Longley DB, Harkin DP, Johnston PG. 5-fluorouracil: mechanisms of action and clinical strategies. Nat Rev Cancer. 2003;3(5):330-8. doi: 10.1038/nrc1074. PubMed PMID: 12724731.

142. Seow HF, Yip WK, Fifis T. Advances in targeted and immunobased therapies for colorectal cancer in the genomic era. Onco Targets Ther. 2016;9:1899-920. doi: 10.2147/OTT.S95101. PubMed PMID: 27099521; PubMed Central PMCID: PMCPMC4821380.

143. Prenen H, Vecchione L, Van Cutsem E. Role of targeted agents in metastatic colorectal cancer. Target Oncol. 2013;8(2):83-96. doi: 10.1007/s11523-013-0281-x. PubMed PMID: 23645285.

144. Nandikolla AG, Rajdev L. Targeting angiogenesis in gastrointestinal tumors: current challenges. Transl Gastroenterol Hepatol. 2016;1:67. doi: 10.21037/tgh.2016.08.04. PubMed PMID: 28138633; PubMed Central PMCID: PMCPMC5244743.

145. Axelrod DE, Vedula S, Obaniyi J. Effective chemotherapy of heterogeneous and drug-resistant early colon cancers by intermittent dose schedules: a computer simulation study. Cancer Chemother Pharmacol. 2017;79(5):889-98. doi: 10.1007/s00280-017-3272-2. PubMed PMID: 28343282.

146. Sargent DJ, Marsoni S, Monges G, Thibodeau SN, Labianca R, Hamilton SR, et al. Defective mismatch repair as a predictive marker for lack of efficacy of fluorouracil-based adjuvant therapy in colon cancer. J Clin Oncol. 2010;28(20):3219-26. doi: 10.1200/JCO.2009.27.1825. PubMed PMID: 20498393; PubMed Central PMCID: PMCPMC2903323.

147. Leguisamo NM, Gloria HC, Kalil AN, Martins TV, Azambuja DB, Meira LB, et al. Base excision repair imbalance in colorectal cancer has prognostic value

and modulates response to chemotherapy. Oncotarget. 2017;8:54199-214. doi: 10.18632/oncotarget.14909. PubMed PMID: 28159922.

148. Bijnsdorp IV, Peters GJ, Temmink OH, Fukushima M, Kruyt FA. Differential activation of cell death and autophagy results in an increased cytotoxic potential for trifluorothymidine compared to 5-fluorouracil in colon cancer cells. Int J Cancer. 2010;126(10):2457-68. doi: 10.1002/ijc.24943. PubMed PMID: 19816940.

149. Maksimenko A, Alami M, Zouhiri F, Brion JD, Pruvost A, Mougin J, et al. Therapeutic modalities of squalenoyl nanocomposites in colon cancer: an ongoing search for improved efficacy. ACS Nano. 2014;8(3):2018-32. doi: 10.1021/nn500517a. PubMed PMID: 24555414; PubMed Central PMCID: PMCPMC4060170.

150. Anitha A, Sreeranganathan M, Chennazhi KP, Lakshmanan VK, Jayakumar R. In vitro combinatorial anticancer effects of 5-fluorouracil and curcumin loaded N,O-carboxymethyl chitosan nanoparticles toward colon cancer and in vivo pharmacokinetic studies. Eur J Pharm Biopharm. 2014;88(1):238-51. doi: 10.1016/j.ejpb.2014.04.017. PubMed PMID: 24815764.

151. Wang K, Liu L, Zhang T, Zhu YL, Qiu F, Wu XG, et al. Oxaliplatin-incorporated micelles eliminate both cancer stem-like and bulk cell populations in colorectal cancer. Int J Nanomedicine. 2011;6:3207-18. doi: 10.2147/IJN.S26268. PubMed PMID: 22238509; PubMed Central PMCID: PMCPMC3254265.

152. Judge AD, Robbins M, Tavakoli I, Levi J, Hu L, Fronda A, et al. Confirming the RNAi-mediated mechanism of action of siRNA-based cancer therapeutics in mice. J Clin Invest. 2009;119(3):661-73. doi: 10.1172/JCI37515. PubMed PMID: 19229107; PubMed Central PMCID: PMCPMC2648695.

153. Jain A, Jain SK. In vitro and cell uptake studies for targeting of ligand anchored nanoparticles for colon tumors. Eur J Pharm Sci. 2008;35(5):404-16. doi: 10.1016/j.ejps.2008.08.008. PubMed PMID: 18824095.

154. Jain KK. Advances in the field of nanooncology. BMC Med. 2010;8:83. doi: 10.1186/1741-7015-8-83. PubMed PMID: 21144040; PubMed Central PMCID: PMCPMC3018446.

155. Urbanska AM, Karagiannis ED, Guajardo G, Langer RS, Anderson DG. Therapeutic effect of orally administered microencapsulated oxaliplatin for colorectal cancer. Biomaterials. 2012;33(18):4752-61. doi: 10.1016/j.biomaterials.2012.03.023. PubMed PMID: 22472433; PubMed Central PMCID: PMCPMC3586541.

156. Chibaudel B, Maindrault-Goebel F, Bachet JB, Louvet C, Khalil A, Dupuis O, et al. PEPCOL: a GERCOR randomized phase II study of nanoliposomal irinotecan PEP02 (MM-398) or irinotecan with leucovorin/5-fluorouracil as second-line therapy in metastatic colorectal cancer. Cancer Med. 2016;5(4):676-83. doi: 10.1002/cam4.635. PubMed PMID: 26806397; PubMed Central PMCID: PMCPMC4831286.

157. Batist G, Gelmon KA, Chi KN, Miller WH, Jr., Chia SK, Mayer LD, et al. Safety, pharmacokinetics, and efficacy of CPX-1 liposome injection in patients

with advanced solid tumors. Clin Cancer Res. 2009;15(2):692-700. doi: 10.1158/1078-0432.CCR-08-0515. PubMed PMID: 19147776.

158. Vizirianakis IS. Nanomedicine and personalized medicine toward the application of pharmacotyping in clinical practice to improve drug-delivery outcomes. Nanomedicine. 2011;7(1):11-7. doi: 10.1016/j.nano.2010.11.002. PubMed PMID: 21094279.

159. Frank D, Tyagi C, Tomar L, Choonara YE, du Toit LC, Kumar P, et al. Overview of the role of nanotechnological innovations in the detection and treatment of solid tumors. Int J Nanomedicine. 2014;9:589-613. doi: 10.2147/IJN.S50941. PubMed PMID: 24489467; PubMed Central PMCID: PMCPMC3904834.

160. Miller MA, Gadde S, Pfirschke C, Engblom C, Sprachman MM, Kohler RH, et al. Predicting therapeutic nanomedicine efficacy using a companion magnetic resonance imaging nanoparticle. Sci Transl Med. 2015;7(314):314ra183. doi: 10.1126/scitranslmed.aac6522. PubMed PMID: 26582898; PubMed Central PMCID: PMCPMC5462466.

161. Yamamoto S, Kato A, Sakurai Y, Hada T, Harashima H. Modality of tumor endothelial VEGFR2 silencing-mediated improvement in intratumoral distribution of lipid nanoparticles. J Control Release. 2017;251:1-10. doi: 10.1016/j.jconrel.2017.02.010. PubMed PMID: 28192155.

162. Ernsting MJ, Murakami M, Roy A, Li SD. Factors controlling the pharmacokinetics, biodistribution and intratumoral penetration of nanoparticles. J

Control Release. 2013;172(3):782-94. doi: 10.1016/j.jconrel.2013.09.013. PubMed PMID: 24075927; PubMed Central PMCID: PMCPMC3891171.

163. Daldrup-Link HE, Okuhata Y, Wolfe A, Srivastav S, Oie S, Ferrara N, et al. Decrease in tumor apparent permeability-surface area product to a MRI macromolecular contrast medium following angiogenesis inhibition with correlations to cytotoxic drug accumulation. Microcirculation. 2004;11(5):387-96. doi: 10.1080/10739680490457665. PubMed PMID: 15280064.

164. Lassau N, Coiffier B, Kind M, Vilgrain V, Lacroix J, Cuinet M, et al. Selection of an early biomarker for vascular normalization using dynamic contrast-enhanced ultrasonography to predict outcomes of metastatic patients treated with bevacizumab. Ann Oncol. 2016;27(10):1922-8. doi: 10.1093/annonc/mdw280. PubMed PMID: 27502701; PubMed Central PMCID: PMCPMC5035788.

165. Lee H, Zheng J, Gaddy D, Orcutt KD, Leonard S, Geretti E, et al. A gradient-loadable (64)Cu-chelator for quantifying tumor deposition kinetics of nanoliposomal therapeutics by positron emission tomography. Nanomedicine. 2015;11(1):155-65. doi: 10.1016/j.nano.2014.08.011. PubMed PMID: 25200610.

166. Lee HG, D.; Ventura, M.; Bernards, N.; de Souza, R.; Kirpotin, D.; Wickham, T.; Fitzgerald, J.; Zheng, J.; Hendriks, B. S. Companion Diagnostic 64Cu-Liposome Positron Emission Tomography Enables Characterization of Drug Delivery to Tumors and Predicts Response to Cancer Nanomedicines. Manuscript submitted for publication. 2017.

167. Hudson HM, Larkin RS. Accelerated image reconstruction using ordered subsets of projection data. IEEE Trans Med Imaging. 1994;13(4):601-9. doi: 10.1109/42.363108. PubMed PMID: 18218538.

168. Peng F, Lu X, Janisse J, Muzik O, Shields AF. PET of human prostate cancer xenografts in mice with increased uptake of 64CuCl2. J Nucl Med. 2006;47(10):1649-52. PubMed PMID: 17015901.

169. Raz A, Bucana C, Fogler WE, Poste G, Fidler IJ. Biochemical, morphological, and ultrastructural studies on the uptake of liposomes by murine macrophages. Cancer Res. 1981;41(2):487-94. PubMed PMID: 7448797.

170. Lee H, Shields AF, Siegel BA, Miller KD, Krop I, Ma CX, et al. 64Cu-MM-302 Positron Emission Tomography Quantifies Variability of Enhanced Permeability and Retention of Nanoparticles in Relation to Treatment Response in Patients with Metastatic Breast Cancer. Clin Cancer Res. 2017;23(15):4190-202. doi: 10.1158/1078-0432.CCR-16-3193. PubMed PMID: 28298546.

171. Fonseca NA, Gregorio AC, Valerio-Fernandes A, Simoes S, Moreira JN. Bridging cancer biology and the patients' needs with nanotechnology-based approaches. Cancer Treat Rev. 2014;40(5):626-35. doi: 10.1016/j.ctrv.2014.02.002. PubMed PMID: 24613464.

172. Ranganathan R, Madanmohan S, Kesavan A, Baskar G, Krishnamoorthy YR, Santosham R, et al. Nanomedicine: towards development of patient-friendly drug-delivery systems for oncological applications. Int J Nanomedicine. 2012;7:1043-60. doi: 10.2147/IJN.S25182. PubMed PMID: 22403487; PubMed Central PMCID: PMCPMC3292417.

173. Shapira A, Livney YD, Broxterman HJ, Assaraf YG. Nanomedicine for targeted cancer therapy: towards the overcoming of drug resistance. Drug Resist Updat. 2011;14(3):150-63. doi: 10.1016/j.drup.2011.01.003. PubMed PMID: 21330184.

174. Reynolds JG, Geretti E, Hendriks BS, Lee H, Leonard SC, Klinz SG, et al. HER2-targeted liposomal doxorubicin displays enhanced anti-tumorigenic effects without associated cardiotoxicity. Toxicol Appl Pharmacol. 2012;262(1):1-10. doi: 10.1016/j.taap.2012.04.008. PubMed PMID: 22676972.

175. Mollard S, Ciccolini J, Imbs DC, El Cheikh R, Barbolosi D, Benzekry S. Model driven optimization of antiangiogenics + cytotoxics combination: application to breast cancer mice treated with bevacizumab + paclitaxel doublet leads to reduced tumor growth and fewer metastasis. Oncotarget. 2017;8(14):23087-98. doi: 10.18632/oncotarget.15484. PubMed PMID: 28416742.

176. Hutchinson LG, Mueller HJ, Gaffney EA, Maini PK, Wagg J, Phipps A, et al. Modeling Longitudinal Preclinical Tumor Size Data to Identify Transient Dynamics in Tumor Response to Antiangiogenic Drugs. CPT Pharmacometrics Syst Pharmacol. 2016;5(11):636-45. doi: 10.1002/psp4.12142. PubMed PMID: 27863175; PubMed Central PMCID: PMCPMC5192995.

177. Wong PP, Bodrug N, Hodivala-Dilke KM. Exploring Novel Methods for Modulating Tumor Blood Vessels in Cancer Treatment. Curr Biol. 2016;26(21):R1161-R6. doi: 10.1016/j.cub.2016.09.043. PubMed PMID: 27825457.

178. Babu A, Templeton AK, Munshi A, Ramesh R. Nanodrug delivery systems: a promising technology for detection, diagnosis, and treatment of cancer. AAPS PharmSciTech. 2014;15(3):709-21. doi: 10.1208/s12249-014-0089-8. PubMed PMID: 24550101; PubMed Central PMCID: PMCPMC4037475.

179. Kalra AV, Kim J, Klinz SG, Paz N, Cain J, Drummond DC, et al. Preclinical activity of nanoliposomal irinotecan is governed by tumor deposition and intratumor prodrug conversion. Cancer Res. 2014;74(23):7003-13. doi: 10.1158/0008-5472.CAN-14-0572. PubMed PMID: 25273092.

180. Drummond DC, Noble CO, Guo Z, Hong K, Park JW, Kirpotin DB. Development of a highly active nanoliposomal irinotecan using a novel intraliposomal stabilization strategy. Cancer Res. 2006;66(6):3271-7. doi: 10.1158/0008-5472.CAN-05-4007. PubMed PMID: 16540680.

181. Conti PS, Alauddin MM, Fissekis JR, Schmall B, Watanabe KA. Synthesis of 2'-fluoro-5-[11C]-methyl-1-beta-D-arabinofuranosyluracil ([11C]-FMAU): a potential nucleoside analog for in vivo study of cellular proliferation with PET. Nucl Med Biol. 1995;22(6):783-9. PubMed PMID: 8535339.

182. Conti PS, Bading JR, Mouton PP, Links JM, Alauddin MM, Fissekis JD, et al. In vivo measurement of cell proliferation in canine brain tumor using C-11-labeled FMAU and PET. Nucl Med Biol. 2008;35(1):131-41. doi: 10.1016/j.nucmedbio.2007.09.003. PubMed PMID: 18158952.

183. Miran T, Vogg ATJ, El Moussaoui L, Kaiser HJ, Drude N, von Felbert V, et al. Dual addressing of thymidine synthesis pathways for effective targeting of proliferating melanoma. Cancer Med. 2017;6(7):1639-51. doi:

10.1002/cam4.1113. PubMed PMID: 28608446; PubMed Central PMCID: PMCPMC5504322.

184. Munch-Petersen B, Cloos L, Tyrsted G, Eriksson S. Diverging substrate specificity of pure human thymidine kinases 1 and 2 against antiviral dideoxynucleosides. J Biol Chem. 1991;266(14):9032-8. PubMed PMID: 2026611.

185. Munch-Petersen B, Tyrsted G. Induction of thymidine kinases in phytohaemagglutinin-stimulated human lymphocytes. Biochim Biophys Acta. 1977;478(3):364-75. PubMed PMID: 911839.

186. Lee LS, Cheng Y. Human deoxythymidine kinase II: substrate specificity and kinetic behavior of the cytoplasmic and mitochondrial isozymes derived from blast cells of acute myelocytic leukemia. Biochemistry. 1976;15(17):3686-90. PubMed PMID: 1066165.

187. Grierson JR, Schwartz JL, Muzi M, Jordan R, Krohn KA. Metabolism of 3'-deoxy-3'-[F-18]fluorothymidine in proliferating A549 cells: validations for positron emission tomography. Nucl Med Biol. 2004;31(7):829-37. doi: 10.1016/j.nucmedbio.2004.06.004. PubMed PMID: 15464384.

188. DeBerardinis RJ, Chandel NS. Fundamentals of cancer metabolism. Sci Adv. 2016;2(5):e1600200. doi: 10.1126/sciadv.1600200. PubMed PMID: 27386546; PubMed Central PMCID: PMCPMC4928883.

189. Obre E, Rossignol R. Emerging concepts in bioenergetics and cancer research: metabolic flexibility, coupling, symbiosis, switch, oxidative tumors, metabolic remodeling, signaling and bioenergetic therapy. Int J Biochem Cell

Biol. 2015;59:167-81. doi: 10.1016/j.biocel.2014.12.008. PubMed PMID: 25542180.

190. Bellance N, Lestienne P, Rossignol R. Mitochondria: from bioenergetics to the metabolic regulation of carcinogenesis. Front Biosci (Landmark Ed). 2009;14:4015-34. PubMed PMID: 19273331.

191. Sancho P, Barneda D, Heeschen C. Hallmarks of cancer stem cell metabolism. Br J Cancer. 2016;114(12):1305-12. doi: 10.1038/bjc.2016.152. PubMed PMID: 27219018; PubMed Central PMCID: PMCPMC4984474.

192. Guerra F, Arbini AA, Moro L. Mitochondria and cancer chemoresistance. Biochim Biophys Acta. 2017;1858(8):686-99. doi: 10.1016/j.bbabio.2017.01.012. PubMed PMID: 28161329.

193. Chang JY, Yi HS, Kim HW, Shong M. Dysregulation of mitophagy in carcinogenesis and tumor progression. Biochim Biophys Acta. 2017;1858(8):633-40. doi: 10.1016/j.bbabio.2016.12.008. PubMed PMID: 28017650.

194. Vaishampayan UN, Tehrani OS, Lawhorn-Crews JM, Heilbrun LK, Dobson K, Smith D, et al. A Pilot Trial Evaluating Zoledronic Acid Induced Changes in [18F]FMAU-Positron Emission Tomography Imaging of Bone Metastases in Prostate Cancer. Mol Imaging Biol. 2017. doi: 10.1007/s11307-017-1057-y. PubMed PMID: 28289967.

195. Jadvar H. Imaging Cellular Proliferation in Prostate Cancer with Positron Emission Tomography. Asia Ocean J Nucl Med Biol. 2015;3(2):72-6. PubMed PMID: 27408885; PubMed Central PMCID: PMCPMC4937643.

ABSTRACT

PET IMAGING OF EARLY THERAPEUTIC RESPONSE IN SOLID TUMORS

by

STEPHANIE J. BLOCKER

December 2017

Advisor: Dr. Anthony F. Shields

Major: Cancer Biology

Degree: Doctor of Philosophy

An important pillar of precision medicine for oncology is the ability to identify patients who respond to treatment early into their therapy. Positron emission tomography (PET) allows physicians and researchers to measure changes in tumor behavior prior to noticeable differences in morphology.

Objective: Determine the utility of multiple tracers for PET in assessing early changes in tumor activity that result from treatment.

Methods: Two tracers for PET were studied. ^{64}Cu-labeled liposomes were used to assess changes in liposome delivery two solid colon tumors early into treatment with bevacizumab (Bev). ^{18}F-FMAU thymidine analog (1-(2'-deoxy-2'-fluoro-beta-D-arabinofuranosyl)thymine), was utilized to detect early response to cisplatin treatment in non-small cell lung tumor models. Scans were analyzed before and after short-term therapy to determine changes in tracer retention which suggest therapeutic response.

Results: In each study PET was able to detect changes in tumor behavior which occurred early into treatment. After two injections of Bev over one week,

liposome delivery was significantly reduced as measured by PET. In lung tumors, 24 hours of cisplatin treatment induced significant drops in ^{18}F-FMAU retention in cisplatin sensitive tumors compared to resistant tumors.

Conclusion: PET imaging with a variety of tracers can provide information about tumor response to a broad spectrum of treatments. Thus, PET is a powerful tool for personalized therapy of cancer.

AUTOBIOGRAPHICAL STATEMENT

Stephanie Blocker

EDUCATION

Wayne State University
Ph.D. in Cancer Biology December, 2017

Albion College
B.A. in Biology
May, 2011

SELECTED GRANTS

Graduate Fellowship, DeRoy Testamentary Foundation 2015-2016
NRSA T32 Training Grant Fellowship 2013-2014

SELECTED PUBLICATIONS

Blocker SJ, Douglas KA, Polin LA, Lee H, Hendriks BS, Lalo E, Chen W, Shields AF. Liposomal ^{64}Cu-PET Imaging of Anti-VEGF Drug Effects on Liposomal Delivery to Colon Cancer Xenografts. *Theranostics.* In Press, 2017

Lee H, Shields AF, Siegel BA, Miller KD, Krop I, Ma CX, LoRusso PM, Munster PN, Campbell K, Gaddy DF, Leonard SC, Geretti E, **Blocker SJ**, Kirpotin DB, Moyo V, Wickham TJ, Hendriks BS. ^{64}Cu-MM-302 Positron Emission Tomography Quantifies Variability of Enhanced Permeability and Retention of Nanoparticles in Relation to Treatment Response in Patients with Metastatic Breast Cancer. *Clinical Cancer Research*: an official journal of the American Association for Cancer Research. 2017. doi: 10.1158/1078-0432.CCR16-3193. PubMed PMID: 28298546.